

# **Towards high resolution resting-state fMRI in the mouse brain**

Mapping of mouse resting state networks using ultra-high field MRI

**Bárbara Polena Pacheco Araújo Costa**

Thesis to obtain the Master of Science Degree in  
**Biomedical Engineering**

Supervisor: Dr. Noam Shemesh  
Co-Supervisor: Prof. Patrícia Margarida Piedade Figueiredo

## **Examination Committee**

Chairperson: Prof. João Orlando Marques Gameiro Folgado  
Supervisor: Dr. Noam Shemesh  
Member of the Committee: Dr. Alexandre da Rocha Freire de Andrade

**November 2019**

# **Preface**

The work presented in this thesis was performed at the Neuroplasticity and Neural Activity Lab of the Champalimaud Research (Lisbon, Portugal) in Champalimaud Centre for the Unknown during the period February-October 2019, under the supervision of Dr. Noam Shemesh. The thesis was co-supervised at Instituto Superior Técnico by Prof. Patrícia Figueiredo.

# **Declaration**

I declare that this document is an original work of my own authorship and that it fulfills all the requirements of the Code of Conduct and Good Practices of the Universidade de Lisboa.

# Acknowledgments

Firstly, I would like to thank my supervisor, Noam Shemesh, for all his help and guidance, and especially for providing all the amazing opportunities I had along these months. I would also like to thank my lab colleagues, particularly, Julia for her kindness and patience, Francisca for always being so helpful and friendly (even through uncharted Canadian territory), Rita for being so caring since the very beginning, Teresa and Clem for being the best neighbors, Fred for his motherly presence, and Cris for her constant aid and inspiration. A huge thank you for all for the amazing people in the lab, for the supportive environment, as well as for being an endless source of fun lunches and chocolate breaks - I feel truly lucky to have spent this semester in this incredible lab!

Of course, this project would not have been possible without the never-ending support of my parents, who kept checking if I was eating healthy (which I was. Most of the time), my brother, and my grandmas and aunt. Their curiosity, interest and affection were present on a daily basis, for which I am deeply grateful.

A heartfelt thank you to all my friends in IST and beyond, who made the last years such a memorable and enriching experience, namely Di and Clara, Eva, Raquel, my Shrek mates, and my precious Fellergut family.

Last but definitely not least, a very special thanks to my dear boyfriend Miguel, for his continuous support even when I was grumpy, stressed and/or tired, and for giving good advice, encouragement words, and the best hugs.



# Abstract

Resting-state functional magnetic resonance imaging (rsfMRI) allows the study of functional connectivity in the brain. Through the mapping of functional networks, it is possible to extract information about the intrinsic organization and function of the brain, as well as to study pathologies and arousal states. Considering that controlled preclinical experiments allow combining rsfMRI with other techniques, and that transgenic mouse models are particularly good models for neurological diseases, murine imaging is becoming an attractive option. Still, there are inherent technical difficulties in imaging mice, and detection of robust and consistent networks has been challenging. Moreover, mouse rsfMRI is usually performed at relatively low spatial resolution, limiting the investigation of small structures. In this study, to overcome these shortcomings, rsfMRI datasets were acquired with both standard (0.3 mm x 0.3 mm) and high resolution (0.16 mm x 0.16 mm), different preprocessing pipelines were tested, and a seed-based analysis was conducted with seeds on cortical and subcortical areas. No significant differences were found between pipelines, but it was possible to reproduce functional networks mostly consistent with previous literature, particularly on motor (M1), somatosensory (S1 and S2) and visual (VC) cortices, hippocampus (Hip) and caudate putamen (CPu), for both low- and high-resolution datasets. Considering the high variability of possible data acquisition parameters, anesthetic regimes, preprocessing and analysis pipelines, these consistent network mappings are encouraging results for rsfMRI in mice as translational tools for the study of large-scale neural dynamics, as well as fundamental mechanisms of small structures in the brain.

**Keywords:** Resting state functional MRI, Functional connectivity, Mouse model, Resting state networks, Seed-based analysis.



# Resumo

Imagens de ressonância magnética funcional em estado de repouso (rsfMRI) permitem estudar a conectividade funcional cerebral. O mapeamento de redes funcionais possibilita a extração de informação sobre organização e função intrínsecas do cérebro, assim como o estudo de patologias e estados psicológicos. Considerando que estudos pré-clínicos permitem combinar rsfMRI com outras técnicas, e que modelos de ratinho são particularmente bons para doenças neurológicas, estudos em roedores são cada vez mais uma opção atraente. Contudo, existem dificuldades técnicas inerentes a rsfMRI em ratinhos, e a detecção de redes robustas e consistentes tem sido desafiante. Além disso, rsfMRI em roedores é normalmente realizada com resolução espacial relativamente baixa, limitando a investigação de estruturas pequenas. Neste estudo, para superar estas limitações, imagens de rsfMRI foram adquiridas com baixa (0.3 mm x 0.3 mm) e alta (0.16 mm x 0.16 mm) resolução, diferentes métodos de pré-processamento foram testados e uma análise baseada em *seeds* foi realizada em áreas corticais e subcorticais. Não foram encontradas diferenças significativas entre os pré-processamentos, mas foram reproduzidas redes funcionais coerentes com a literatura, nomeadamente nos córtices motor (M1), somatossensorial (S1 e S2) e visual (VC), no hipocampo (Hip) e corpo estriado dorsal (CPu), para imagens de baixa e alta resolução. Considerando a grande variabilidade de possíveis parâmetros de aquisição de imagens, regimes anestésicos, e de métodos de pré-processamento e análise, este mapeamento consistente é encorajador para rsfMRI em ratinhos como ferramenta translacional para o estudo de dinâmicas neuronais em grande escala, assim como mecanismos fundamentais de pequenas estruturas cerebrais.

**Palavras-chave:** Imagens de ressonância magnética funcional em estado de repouso, Conectividade funcional, Modelo de ratinho, Redes neuronais de repouso, Análise baseada em *seeds*.



# Table of Contents

|   |             |
|---|-------------|
| <b>Preface</b> .....  | <b>ii</b>   |
| <b>Declaration</b> .....  | <b>ii</b>   |
| <b>Acknowledgments</b> .....  | <b>iii</b>  |
| <b>Abstract</b> .....   | <b>v</b>    |
| <b>Resumo</b> .....   | <b>vii</b>  |
| <b>Table of Contents</b> .....  | <b>ix</b>   |
| <b>List of Figures</b> .....  | <b>xi</b>   |
| <b>List of Tables</b> .....   | <b>xiii</b> |
| <b>List of Acronyms</b> .....   | <b>xv</b>   |
| <b>1. Introduction</b> .....  | <b>1</b>    |
| 1.1. Motivation .....   | 1           |
| 1.2. Magnetic Resonance Imaging.....  | 2           |
| 1.2.1. Magnetic Resonance Physics .....   | 2           |
| 1.2.1.A. Spins in an External Static Magnetic Field .....                               | 2           |
| 1.2.1.B. Excitation and Relaxation of a Spin System .....                               | 4           |
| 1.2.2. Magnetic Resonance Imaging.....  | 7           |
| 1.2.2.A. Slice Selection.....   | 7           |
| 1.2.2.B. Phase and Frequency Encoding.....  | 8           |
| 1.2.2.C. Image Contrast and Primary MRI Pulse Sequences .....                           | 10          |
| 1.3. Functional Magnetic Resonance Imaging .....  | 11          |
| 1.3.1. The Blood Oxygenation Level Dependent Contrast.....                              | 11          |
| 1.3.1.A. Neuronal Activation and its Hemodynamic Effects (Neurovascular Coupling) ..... | 12          |
| 1.3.1.B. The BOLD Signal .....  | 14          |
| 1.3.2. BOLD Signal: Imaging Considerations.....   | 15          |
| 1.3.2.A. Gradient-Echo and Spin-Echo Sequences .....                                    | 15          |
| 1.3.2.B. Temporal Resolution.....   | 16          |
| 1.3.2.C. Spatial Resolution .....   | 17          |
| 1.3.3. Blocked and Event Related Experimental Designs.....                              | 18          |
| 1.3.4. Resting State Functional Magnetic Resonance Imaging .....                        | 18          |
| 1.3.5. Analysis of Resting State fMRI Data .....  | 19          |
| 1.3.5.A. Preprocessing .....  | 20          |
| 1.3.5.B. Postprocessing.....  | 21          |
| 1.4. Anesthesia in Rodent fMRI Experiments.....   | 22          |

|   |           |
|---|-----------|
| 1.5. State of the Art of Resting State fMRI in Mice ..... | 23        |
| 1.6. Thesis Objectives .....                              | 26        |
| 1.7. Thesis Outline .....                                 | 26        |
| <b>2. Materials and Methods .....</b>                     | <b>27</b> |
| 2.1. Optimization of Acquisition Parameters .....         | 27        |
| 2.1.1. Animal Preparation .....                           | 27        |
| 2.1.2. MRI Protocol .....                                 | 29        |
| 2.1.3. Urethane characterization .....                    | 31        |
| 2.2. Resting State fMRI Experiments .....                 | 32        |
| 2.2.1. Animal Preparation .....                           | 32        |
| 2.2.2. MRI Protocol .....                                 | 32        |
| 2.3. Data Analysis .....                                  | 34        |
| 2.3.1. Preprocessing Pipeline .....                       | 34        |
| 2.3.2. Postprocessing .....                               | 36        |
| <b>3. Results .....</b>                                   | <b>39</b> |
| 3.1. Optimization of Acquisition Parameters .....         | 39        |
| 3.1.1. Preliminary Resting State fMRI Acquisitions .....  | 39        |
| 3.1.2. Urethane Characterization .....                    | 41        |
| 3.2. Resting state fMRI experiments .....                 | 42        |
| 3.2.1. Quality Control .....                              | 42        |
| 3.2.2. Resting State Analysis .....                       | 48        |
| 3.2.2.A. Low Resolution .....                             | 48        |
| 3.2.2.B. High Resolution .....                            | 52        |
| <b>4. Discussion .....</b>                                | <b>57</b> |
| 4.1. Optimization of Acquisition Parameters .....         | 58        |
| 4.1.1. Preliminary Resting State fMRI Acquisitions .....  | 58        |
| 4.1.2. Urethane Characterization .....                    | 59        |
| 4.2. Resting State fMRI Experiments .....                 | 60        |
| 4.2.1. Low Resolution .....                               | 60        |
| 4.2.2. High Resolution .....                              | 63        |
| <b>5. Conclusions and Future Work .....</b>               | <b>65</b> |
| <b>6. References .....</b>                                | <b>67</b> |
| <b>Annex A .....</b>                                      | <b>73</b> |

# List of Figures

|  |    |
|--|----|
| <b>Figure 1.1:</b> Spin distributions in the presence of a magnetic field $B_0$ .....  | 3  |
| <b>Figure 1.2:</b> Net magnetization concept.....  | 4  |
| <b>Figure 1.3:</b> Laboratory and rotating frames .....  | 5  |
| <b>Figure 1.4:</b> Excitation of a spin system through a $90^\circ$ RF pulse .....   | 5  |
| <b>Figure 1.5:</b> Longitudinal and transverse relaxation .....  | 6  |
| <b>Figure 1.6:</b> Schematic representation of a pulse sequence .....  | 8  |
| <b>Figure 1.7:</b> K-space cartesian filling .....   | 10 |
| <b>Figure 1.8:</b> Different tissue contrasts.....   | 10 |
| <b>Figure 1.9:</b> Primary MRI pulse sequences .....   | 11 |
| <b>Figure 1.10:</b> Cortical vasculature on a microscopic level .....  | 13 |
| <b>Figure 1.11:</b> The Hemodynamic Response Function (HRF) .....  | 14 |
| <b>Figure 1.12:</b> GE-EPI sequence .....  | 16 |
| <b>Figure 1.13:</b> Typical RSNs in the human brain.....   | 19 |
| <b>Figure 1.14:</b> Final connectivity maps obtained with a 0.6mg/kg/h medetomidine dosage, at two time points, in six seeds.....  | 25 |
| <b>Figure 2.1:</b> Schematic representation of the main steps performed in the optimization stage, and in the final resting state acquisition phase .....  | 27 |
| <b>Figure 2.2:</b> Three orthogonal planes, as applied conventionally to the mouse body .....  | 29 |
| <b>Figure 2.3:</b> Paradigm used for visual stimulation .....  | 30 |
| <b>Figure 2.4:</b> Schematic representation of a normal medetomidine imaging session, with the main steps and their relative, approximate duration .....   | 31 |
| <b>Figure 2.5:</b> Mouse brain regions, with average coverage of structural and functional scans. ....   | 33 |
| <b>Figure 2.6:</b> Example of the 6 motion parameters returned by the motion correction algorithm .....  | 34 |
| <b>Figure 2.7:</b> Outlier detection with a translation threshold of 0.3 mm and intensity threshold of 3 standard deviations from the mean .....   | 35 |
| <b>Figure 2.8:</b> Ventricular masks used for CSF signal regression .....  | 36 |
| <b>Figure 3.1:</b> Raw structural images from one representative mouse.....  | 39 |
| <b>Figure 3.2:</b> Raw functional images from one representative mouse .....   | 40 |
| <b>Figure 3.3:</b> Connectivity map with a seed on M1, using the baseline preprocessing pipeline .....   | 40 |
| <b>Figure 3.4:</b> Three representative spatial maps obtained from an ICA .....  | 41 |
| <b>Figure 3.5:</b> Representative power spectrum of one of the IC time courses .....   | 41 |
| <b>Figure 3.6:</b> Raw structural images from one representative mouse.....  | 42 |
| <b>Figure 3.7:</b> Raw functional images from one representative mouse (low-resolution run) .....  | 43 |
| <b>Figure 3.8:</b> Raw functional images from one representative mouse (high-resolution run) .....   | 43 |
| <b>Figure 3.9:</b> Brain map of significant ( $p < 0.01$ , minimum cluster size = 15) BOLD activation to binocular visual stimulation with 2 Hz flashing frequency and 10 ms of pulse width..... | 44 |

|  |    |
|--|----|
| <b>Figure 3.10:</b> Location of the ROIs (in red) used in the analysis .....   | 44 |
| <b>Figure 3.11:</b> Timeseries and correlation values, for the first mouse, and first pair of “left-right” ROIs.....   | 45 |
| <b>Figure 3.12:</b> Timeseries and correlation values, for the first mouse, and second pair of “left-right” ROIs.  | 45 |
| <b>Figure 3.13:</b> Timeseries and correlation values, for the second mouse, and first pair of “left-right” ROIs.  | 46 |
| <b>Figure 3.14:</b> Timeseries and correlation values, for the second mouse, and second pair of “left-right” ROIs .....  | 46 |
| <b>Figure 3.15:</b> Registration from functional to structural space.....  | 47 |
| <b>Figure 3.16:</b> Registration from structural to atlas space.....   | 48 |
| <b>Figure 3.17:</b> Anatomical location of pertinent brain areas.....  | 48 |
| <b>Figure 3.18:</b> Connectivity map from an individual low-resolution run with the baseline preprocessing pipeline, with a seed in the left visual cortex (VC).....                     | 49 |
| <b>Figure 3.19:</b> Statistical map from 25 individual connectivity maps, from the lower resolution dataset, with a seed in the VC, thresholded at $p < 0.01$ .....                      | 49 |
| <b>Figure 3.20:</b> Connectivity maps, averaged from 25 runs from the low-resolution dataset (LRD), preprocessed with the baseline pipeline .....  | 49 |
| <b>Figure 3.21:</b> Connectivity maps, averaged from 25 runs from the low-resolution dataset, preprocessed with the pipeline performing GSR .....  | 50 |
| <b>Figure 3.22:</b> Connectivity maps, averaged from 25 runs from the low-resolution dataset, preprocessed with the pipeline performing ventricular signal regression .....              | 50 |
| <b>Figure 3.23:</b> Coincidence map for the baseline preprocessing pipeline, for the lower resolution dataset .  | 51 |
| <b>Figure 3.24:</b> Boxplots showing representative correlation coefficients between 3 interhemispheric regions and 3 preprocessing pipelines, in the low-resolution dataset (LRD).....  | 52 |
| <b>Figure 3.25:</b> Connectivity map from an individual high-resolution run with the baseline preprocessing pipeline, with a seed in the left visual cortex (VC).....                    | 52 |
| <b>Figure 3.26:</b> Statistical map from 9 individual connectivity maps, from the high-resolution dataset, with a seed in the VC, thresholded at $p < 0.01$ .....                        | 53 |
| <b>Figure 3.27:</b> Connectivity maps, averaged from 9 runs from the high-resolution dataset (HRD), preprocessed with the baseline pipeline .....  | 53 |
| <b>Figure 3.28:</b> Connectivity maps, averaged from 9 runs from the high-resolution dataset, preprocessed with the pipeline performing GSR .....  | 54 |
| <b>Figure 3.29:</b> Connectivity maps, averaged from 9 runs from the high-resolution dataset, preprocessed with the pipeline performing ventricular signal regression.....               | 54 |
| <b>Figure 3.30:</b> Coincidence maps for the baseline preprocessing pipeline, for the high-resolution dataset.   | 55 |
| <b>Figure 3.31:</b> Boxplots showing representative correlation coefficients between 3 interhemispheric regions and 3 preprocessing pipelines, in the high-resolution dataset (HRD)..... | 56 |

# List of Tables

|  |    |
|--|----|
| <b>Table 3.1:</b> Features and measurements of 5 mice under a dosage of 1.5g/kg of urethane.....   | 42 |
| <b>Table A.1:</b> Summary of 10 rsfMRI studies performed in mice, highlighting the objective, parameters used in the acquisition and details on animal preparation ..... | 73 |
| <b>Table A.2:</b> Summary of 10 rsfMRI studies performed in mice, highlighting the preprocessing and analysis pipelines, results and main conclusions .....              | 74 |



# List of Acronyms

|                         |  |
|-------------------------|--|
| <b>2-D</b>              | Two-dimensional                                      |
| <b>ACA</b>              | Anterior Cingulate Area                              |
| <b>AFNI</b>             | Analysis of Functional NeuroImages                   |
| <b>ALFF</b>             | Amplitude of Low Frequency Fluctuation               |
| <b>AMBMC</b>            | Australian Mouse Brain Mapping Consortium            |
| <b>ANOVA</b>            | Analysis of variance                                 |
| <b>ANTS</b>             | Advanced Normalization Tools Ecosystem               |
| <b>ATP</b>              | Adenosine triphosphate                               |
| <b>BET</b>              | Brain Extraction Tool                                |
| <b>BOLD</b>             | Blood Oxygenation Level Dependent                    |
| <b>CBF</b>              | Cerebral Blood Flow                                  |
| <b>CBV</b>              | Cerebral Blood Volume                                |
| <b>CMRO<sub>2</sub></b> | Cerebral metabolic rate for oxygen                   |
| <b>CPu</b>              | Caudate Putamen                                      |
| <b>CSF</b>              | Cerebrospinal Fluid                                  |
| <b>dFC</b>              | Dynamic Functional Connectivity                      |
| <b>dHb</b>              | Deoxygenated hemoglobin                              |
| <b>DMN</b>              | Default Mode Network                                 |
| <b>EPI</b>              | Echo Planar Imaging                                  |
| <b>FC</b>               | Functional Connectivity                              |
| <b>fMRI</b>             | Functional Magnetic Resonance Imaging                |
| <b>FOV</b>              | Field of view  |
| <b>FSL</b>              | FMRIB Software Library                               |
| <b>FT</b>               | Fourier Transform                                    |
| <b>FWE</b>              | Family-wise error                                    |
| <b>FWHM</b>             | Full-Width-Half-Maximum                              |
| <b>GE</b>               | Gradient Echo  |
| <b>GLM</b>              | General Linear Model                                 |
| <b>GSR</b>              | Global Signal Regression                             |
| <b>GUI</b>              | Grafical User Interface                              |
| <b>HASTE</b>            | Half-Fourier Acquisition Single-shot Turbo Spin Echo |
| <b>Hb</b>               | Hemoglobin   |
| <b>Hip</b>              | Hippocampus  |
| <b>HR</b>               | High-resolution                                      |

|                |   |
|----------------|---|
| <b>HRD</b>     | High-resolution Dataset   |
| <b>HRF</b>     | Hemodynamic Response Function   |
| <b>IC</b>      | Independent Component   |
| <b>ICA</b>     | Independent Component Analysis  |
| <b>LC</b>      | Locus Coeruleus   |
| <b>LED</b>     | Light emitting diode  |
| <b>LFP</b>     | Local field potential   |
| <b>LGN</b>     | Lateral Geniculate Nucleus  |
| <b>LR</b>      | Low-resolution  |
| <b>LRD</b>     | Low-resolution Dataset  |
| <b>M1</b>      | Primary Motor Cortex  |
| <b>MELODIC</b> | Multivariate Exploratory Linear Optimized Decomposition into Independent Components |
| <b>MGE</b>     | Multiple Gradient Echo  |
| <b>MR</b>      | Magnetic Resonance  |
| <b>MRI</b>     | Magnetic Resonance Imaging  |
| <b>PVE</b>     | Partial Volume Effects  |
| <b>RARE</b>    | Rapid Acquisition with Relaxation Enhancement                                       |
| <b>ReHo</b>    | Regional Homogeneity  |
| <b>RF</b>      | Radiofrequency  |
| <b>ROI</b>     | Region of Interest  |
| <b>rsfMRI</b>  | Resting state fMRI  |
| <b>RSN</b>     | Resting State Network   |
| <b>RSP</b>     | Restrosplenial Area   |
| <b>S1</b>      | Primary Somatosensory Cortex  |
| <b>S2</b>      | Secondary Somatosensory Cortex  |
| <b>SBA</b>     | Seed-Based Analysis   |
| <b>SC</b>      | Superior Colliculus   |
| <b>SE</b>      | Spin Echo   |
| <b>SNR</b>     | Signal-to-Noise Ratio   |
| <b>SPEN</b>    | Spatiotemporal encoding   |
| <b>SyN</b>     | Symmetric Normalization   |
| <b>TE</b>      | Echo Time   |
| <b>Thal</b>    | Thalamus  |
| <b>TR</b>      | Repetition Time   |
| <b>tSNR</b>    | Temporal SNR  |
| <b>VC</b>      | Visual Cortices   |

# 1. Introduction

This chapter introduces the topic of the dissertation. It states the motivation behind this project, while providing the required context and theoretical background for its understanding. Specifically, Magnetic Resonance (MR) and its basic physical concepts, resting state functional MRI and considerations on its analysis and the bias of anesthesia are addressed.

## 1.1. Motivation

On average, the human brain accounts for less than 2% of a person's weight, yet it is responsible for the consumption of up to 20% of all the energy produced by the human body [1]. This occurs even in the absence of a specific cognitive task, making the study of the resting brain and its intrinsic activity a target of research focus. More specifically, resting-state fMRI has been a rapidly growing technique [2] which can be used to extract information about the inherent organization and function of the brain, but also to study pathologies [3]–[5] and different arousal states [6].

Resting-state fMRI also allows the mapping of resting state networks (a set of brain regions whose signal shows similarities across time, during rest), and notably, these networks can be observed across species [7]–[9]. This can be exploited in controlled preclinical experiments through functional connectivity (FC) modification induced by pharmacological alterations [10], and might additionally be combined with various techniques such as electrophysiological recordings or optogenetics [11]–[14]. More specifically, the use of a mouse model can be particularly advantageous due to the wide range of possible genetic manipulations, enabling the use of such techniques [15]. Additionally, transgenic mouse models can be considered as good models for neurological diseases, because of their inherent physiological similarities with humans, and genetic flexibility due to recent technological advances [16]–[18]. Thus, preclinical experiments in mice are becoming highly attractive options for a wide range of fMRI resting state studies.

However, rsfMRI is inherently noisy [19], technically difficult to perform in mice [20], and the mapping of functional networks has been performed so far at relatively low spatial resolution [21]. These factors limit resting-state fMRI in the mouse, namely when considering the study of potentially interesting small structures, such as the Locus Coeruleus (LC). The LC is a small nucleus deep in the brainstem, considered the center of noradrenergic stimulation in the brain, and thought to be associated with many cognitive functions such as attention, memory and learning [22]–[24]. Due to its extremely small size, this and other structures could not be directly imaged and the subject of focus of resting-state experiments. Hence, there is a need to overcome these shortcomings, as the mapping of functional murine networks with a higher resolution could offer valuable and unique insights on the workings of complex systems based on smaller structures.

## 1.2. Magnetic Resonance Imaging

Magnetic resonance imaging (MRI) is a non-invasive three-dimensional imaging technique, which can achieve high spatial and temporal resolutions, and provide various soft-tissue contrasts. It allows imaging in any plane through the body, and does not cause any damage to the tissues, making repeated acquisitions tolerable. This section describes the basic principles of this versatile technique in detail, including magnetic resonance (MR) physics, signal generation, and the image formation process.

### 1.2.1. Magnetic Resonance Physics

For a nucleus to generate MR signal, it must have an odd atomic number and/or an odd number of neutrons. This feature is crucial, as it results in a nonzero nuclear magnetic moment [25], granting the nucleus a quantum property denominated “spin”. Thus, the hydrogen nucleus, which contains a single proton, is the most commonly used one in MR, since it is prevalent in water molecules and consequently abundant in biological tissues. [26]

#### 1.2.1.A. Spins in an External Static Magnetic Field

The spin property can be seen as analogous to a proton revolving around an internal rotation axis. Thus, considering a nucleus capable of MR signal generation, it will have an angular momentum ( $J$ ), defined as:

$$|J| = \frac{h}{2\pi} \sqrt{I(I+1)} \quad (1.1)$$

where  $h$  is Planck’s constant and  $I$  is the spin quantum number of the nucleus. As the proton is a charged particle, this rotation will also originate a magnetic ( $\mu$ ) momentum, defined as:

$$|\mu| = \gamma * |J| \quad (1.2)$$

where  $\gamma$  is the gyromagnetic ratio of the nucleus. Since spin quantum number ( $I$ ) for protons equals  $\frac{1}{2}$ , equations 1.1 and 1.2 can be combined, resulting in a magnitude for the protonic magnetic moment of:

$$|\mu| = \frac{\gamma h \sqrt{3}}{4\pi} \quad (1.3)$$

In the absence of a magnetic field, the spins are randomly oriented in their system, causing the net magnetization  $M$ , which is the vector sum of all their magnetic moments, to be approximately zero, as the individual magnetic moments will annul each other. However, if an external magnetic field  $B_0$  is applied, the

spins align with it, starting a precession around the field's axis [27]. This results in a finite net magnetization. Both the  $B_0$  field and the consequent initial net magnetization are aligned along the  $z$ -axis, by convention, as represented in Figure 1.1.

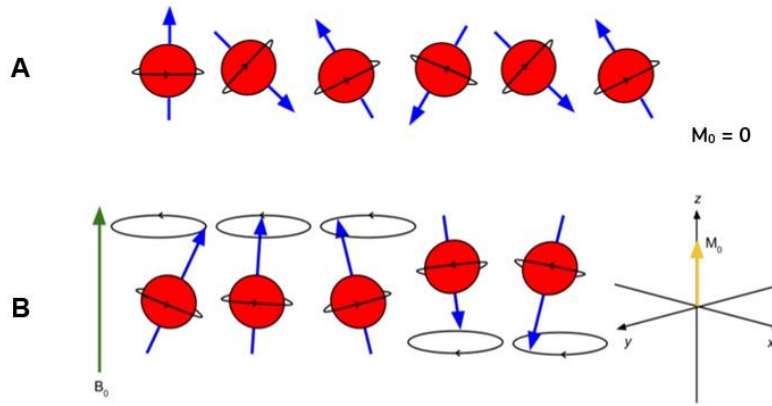


**Figure 1.1:** Spin distributions in the presence of a magnetic field  $B_0$ . (A): Randomly oriented spins, without an external magnetic field applied (and the resulting null net magnetization). (B) (Left): Aligned spins (with parallel and antiparallel orientations) when an external magnetic field  $B_0$  is applied, and (Right): consequent net magnetization  $M_0$ . Adapted from [28].

After the proton is subjected to this external magnetic field  $B_0$ , the interaction energy  $E$  between the magnetic field and the magnetic moment of the proton along the  $z$ -axis can be computed as:

$$E = -\mu_z B_0 \quad (1.4)$$

with

$$\mu_z = \pm \frac{\gamma h}{4\pi} \quad (1.5)$$

From equations 1.4 and 1.5, the following equation can be derived:

$$E = \mp \frac{\gamma h B_0}{4\pi} \quad (1.6)$$

From equation 1.6, it is possible to infer the existence of two energy states: a lower one, composed by the protons whose magnetic moments are aligned with the magnetic field  $B_0$  (parallel state) and against it (antiparallel state). Under the effect of the  $B_0$  field, there is a slightly higher number of protons that have its magnetic moment parallel with  $B_0$ , since it has a lower interaction energy [26]. After some manipulations, it is also possible to note that the protonic population difference between levels is proportional to the strength of the applied  $B_0$  field.

Since the difference between proton populations in parallel and antiparallel states heavily determines the measured MR signal, to obtain said signal, energy must be provided to the system, inducing transitions between states. This energy will be supplied by an oscillating electromagnetic field, and there is a well-defined energy gap  $\Delta E$  defined by:

$$\Delta E = \frac{\gamma h B_0}{2\pi} \quad (1.7)$$

This means the energy provided to the system should also have a specific frequency. From equation 1.7 and Bohr model:

$$\Delta E = h * f \quad (1.8)$$

where  $f$  is the frequency of the electromagnetic pulse, it is possible to derive:

$$f = \frac{\gamma B_0}{2\pi} \quad (1.9)$$

or

$$\omega_L = \gamma B_0 \quad (1.10)$$

where  $\omega_L$  is the angular frequency corresponding to  $f$ . This frequency is also known as Larmor frequency, which is equivalent to the frequency of the spins precessing around  $B_0$  magnetic field axis, as well as the frequency of the provided electromagnetic pulse.

#### 1.2.1.B. Excitation and Relaxation of a Spin System

When the protons are subjected to the  $B_0$  field, the initial net magnetization  $M_0$  has only a longitudinal component (along the  $z$  axis), and a null transverse magnetization (along the  $xy$  plane). Transverse magnetization is initially null, since the spins are randomly distributed around the precession axis (here considered as the conventional  $z$  axis). This can be easily visualized in Figure 1.2.

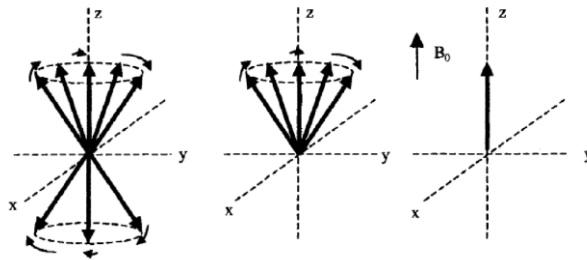


**Figure 1.2:** Net magnetization concept. (*Left*): Representation of the individual protonic magnetic moments, precessing around the  $z$ -axis. It can be noted that there are more protons aligned with the  $B_0$  field than against it. (*Center*): The excess of protons on the parallel state cancels the effect of those on the antiparallel state. (*Right*): The net magnetization only has only a longitudinal component, since it corresponds to the vector sum of the magnetic moments, and no transverse component ( $M_z = M_0$  and  $M_{xy} = 0$ ). Extracted from [26].

As previously mentioned, to measure MR signal, energy must be provided to the system, and this occurs in the form of a radiofrequency (RF) pulse, applied by a transmit coil. This RF pulse is also referred to as  $B_1$  field, and it oscillates at the Larmor frequency. When it is applied, the net magnetization is tipped

towards the axis of that pulse. Thus, the magnetization vector will describe a movement known as nutation, which corresponds to the combination of its precession around the longitudinal axis, and its rotation from the longitudinal to the transverse plane, as illustrated in Figure 1.3 (left). It is possible to simplify this representation by adopting a rotating reference frame, also shown in Figure 1.3 (right). In this reference coordinate system, the  $z$  axis remains in the same orientation, while  $x_{rot}$  and  $y_{rot}$  correspond to the original  $x$  and  $y$  axis respectively but are rotating at the Larmor frequency.

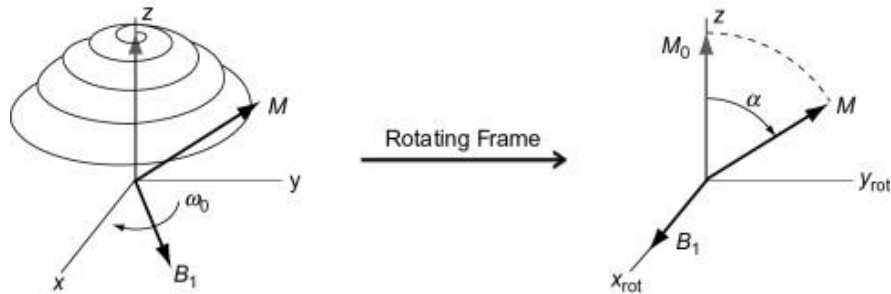


**Figure 1.3:** Laboratory and rotating frames. (Left): Net magnetization  $M$  performing a nutation movement. (Right): Tipping motion of the net magnetization  $M$  towards the transverse plane, with a flip angle of  $\alpha$ . Extracted from [29].

The angle formed between the net magnetization vector  $M$  and the longitudinal axis is known as the flip angle ( $\alpha$ ), and depends on the duration  $T$  of the pulse:

$$\alpha = \gamma B_1 T \quad (1.11)$$

If an ideal  $90^\circ$  pulse is applied, the magnetization vector will be fully rotated into the transverse plane, as is shown in Figure 1.4. The transverse component of the net magnetization is responsible for the detectable MR signal

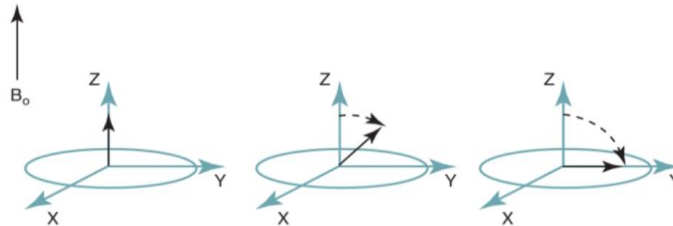


**Figure 1.4:** Excitation of a spin system through a  $90^\circ$  RF pulse. (Left): Initially, the net magnetization vector only has a longitudinal component, as previously explained ( $M_z = M_0$  and  $M_{xy} = 0$ ). (Center): While the RF pulse at Larmor frequency is applied, the magnetization vector starts tipping towards the transverse ( $xy$ ) plane. (Right): The magnetization vector is fully on the transverse plane ( $M_z = 0$  and  $M_{xy} = M_0$ ). Extracted from [30]

After the excitation RF pulse, the system is in a non-equilibrium state, thus it tends to progressively return to its original state. This is attained through the release of the absorbed energy, through two mechanisms: longitudinal and transverse relaxation [25].

Longitudinal relaxation, also known as spin-lattice relaxation or  $T_1$  recovery, occurs after the spins, which have been tipped to the transverse plane after the  $B_1$  field application, start returning to the lower

energy level (which is the parallel state), with their magnetic moments aligned with the  $B_0$  field. This causes the net magnetization vector to be gradually restored to its initial direction. The time constant governing this mechanism is denominated  $T_1$ , which reflects the time it takes for the regrowth of the longitudinal magnetization component to approximately two thirds of its initial value. Therefore, a tissue with a higher  $T_1$  will recover the longitudinal magnetization slower than a tissue with a lower  $T_1$ .

Transverse relaxation, also known as spin-spin relaxation or  $T_2$  decay, occurs as the magnetization on the transverse plane returns to its initial null value. Immediately after the RF pulse application, the transverse magnetization peaks, as the spins are coherent, but the spin-spin interactions cause an irreversible dephasing of the spins, which in its turn, causes the exponential decay of the transverse magnetization. The time constant governing this process is  $T_2$ , and it corresponds to the time it takes for the transverse magnetization to fall to approximately  $e^{-1}$  times its peak value. Thus, analogously to  $T_1$ , a tissue with a higher  $T_2$  will experience a slower decay of transverse magnetization than a tissue with lower  $T_2$ .

The magnitude of the longitudinal and transverse components of magnetization following a pulse of flip angle  $\alpha$  can be described, respectively, as:

$$M_z(t) = M_0 \cos \alpha + (M_0 - M_0 \cos \alpha)(1 - e^{-\frac{t}{T_1}}) \quad (1.12)$$

and

$$M_{xy}(t) = M_0 \sin \alpha e^{-\frac{t}{T_2}} \quad (1.13)$$

If we consider an ideal  $90^\circ$  pulse, equations 1.12 and 1.13 become

$$M_z(t) = M_0 (1 - e^{-\frac{t}{T_1}}) \quad (1.14)$$

and

$$M_{xy}(t) = M_0 e^{-\frac{t}{T_2}} \quad (1.15)$$

The longitudinal and transverse magnetization relaxations over time can be visualized on Figure 1.5.

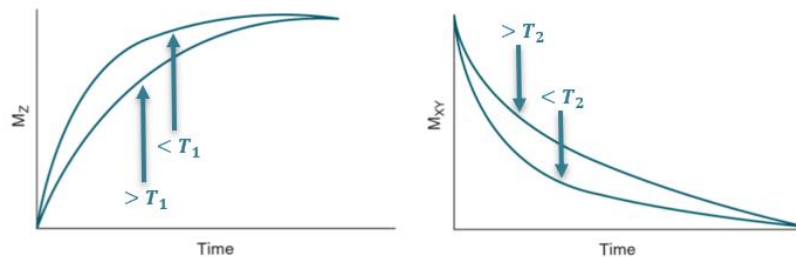


**Figure 1.5:** Longitudinal and transverse relaxation. (Left): Longitudinal magnetization recovery across time. It is possible to verify that a tissue with a lower  $T_1$  recovers its longitudinal magnetization faster than the tissue with the higher  $T_1$ . (Right): Transverse magnetization decay across time. It is possible to verify that a tissue with a lower  $T_2$  recovers its longitudinal magnetization faster than the tissue with the higher  $T_2$ . Adapted from [30].

Transverse magnetization can also be lost as a consequence of spatial magnetic field inhomogeneities. The joined effect of spin-spin interactions and these inhomogeneities can be described by a time constant  $T_2^*$ , which is always lower than  $T_2$ , since it is responsible for a faster magnetization decay [26]. It should be noted that this type of coherence loss is reversible, through the use of specific pulse sequences, such as a spin-echo sequence [26], that uses refocusing pulses to remove inhomogeneous dephasing effects. The time constants  $T_1$ ,  $T_2$  and  $T_2^*$  are specific for each tissue and depend on the magnetic field  $B_0$ . Thus, they will determine the obtained signal for each tissue and should consequently be considered upon imaging.

Briefly, for the MR signal to be obtained, a receiver coil measures variation of the transverse magnetization, caused by the aforementioned excitation and relaxation phenomena. This will generate an electric signal which will afterwards be demodulated, amplified, and Fourier transformed, ultimately resulting in what is known as an MR spectrum. However, this spectrum does not allow the differentiation of spatial properties of the tissue being imaged, i.e. it is not possible to distinguish signal from protons at different locations, as it is merely the sum of individual protonic signals.

## 1.2.2. Magnetic Resonance Imaging

As mentioned by the end of section 1.2.1, the signal described so far does not provide any spatial information, as it is merely the sum of all the individual signals. It was not until 1973 that, through the use of gradient coils, MR signal could be exploited towards image generation [31]. These coils generate uniform gradient fields which, when superimposed with the  $B_0$  magnetic field, cause the protons in different locations to precess at different frequencies, allowing spatial information encoding.

### 1.2.2.A. Slice Selection

In a common MRI experiment, multiple slices are acquired, in a defined anatomical region of interest. For each slice to be acquired, a gradient (conventionally along the  $z$ -axis) with a slice-selective RF pulse are applied. This pulse will only tip the magnetizations of the protons precessing between a defined frequency band, leaving all other magnetizations unaltered [26]. The thickness  $T$  of the slice coinciding with protons affected by the selective RF pulse can be defined as:

$$T = \frac{\Delta\omega_s}{\gamma G_z} \quad (1.16)$$

where  $\Delta\omega_s$  is the frequency bandwidth,  $\gamma$  the gyromagnetic ratio of the nucleus and  $G_z$  the strength of the slice gradient field [26].

To correct spin dephasing and loss of coherence, which occurs after the spins are subjected to the main slice-selection gradient, a rephasing  $z$ -gradient is applied, with half the duration and opposite polarity of the slice selection gradient, as can be seen in Figure 1.6. It should be noted that since an ideal slice

profile is nearly impossible to attain due to inherent technical constraints, excitation of one slice can interfere with adjacent slices, causing slice preexcitation and MR signal saturation, and subsequent intensity and contrast changes. To avoid it, gaps between the slices can be added (rule of thumb, a minimum of ten percent of slice thickness), although this is highly dependent on the used pulses and gradients. As an alternative to slice gaps, which don't allow an optimal spatial coverage, slice acquisition can be performed in an interleaved pattern [26].

### 1.2.2.B. Phase and Frequency Encoding

After slice selection, the remaining two dimensions still have to be encoded, to form the two-dimensional image in the defined slice. This is achieved for one dimension by applying a phase-encoding gradient, which imposes a spatially dependent phase on the precessing protons. For the second dimension to be encoded, a frequency-encoding gradient is applied, provoking a spatially dependent frequency of precession, during signal acquisition [26]. Conventionally, the phase-encoding gradient is represented in the  $y$ -axis, while the frequency-encoding gradient must be orthogonal to the phase-encoding, thus it is typically represented in the  $x$ -axis.

In a complete acquisition sequence, a number  $N_p$  of different values of the phase-encoding gradient is applied before each data acquisition, whereas the frequency-encoding is applied during data acquisition, as can be seen in Figure 1.6. This results in a two-dimensional acquired dataset, sized  $N_p \times N_r$ , considering  $N_r$  as the number of data points acquired during the readout.

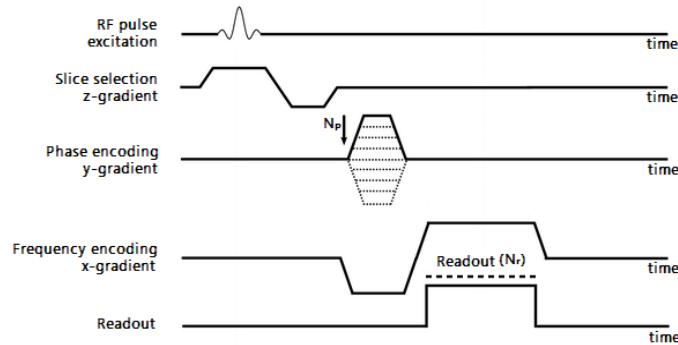


**Figure 1.6:** Schematic representation of a pulse sequence. Slice selection is accomplished by applying a gradient along the  $z$ -axis, followed by the rephasing gradient. Afterwards, a phase-encoding gradient is applied along the  $y$ -axis, and a frequency-encoding along the  $x$ -axis, at the same time as the data acquisition. As shown by the arrow on the phase-encoding, this process must be repeated  $N_p$  times, so that each time a different phase encoding can be acquired. During the readout,  $N_r$  data points are acquired. Therefore, the resulting two-dimensional dataset has a size of  $N_p \times N_r$ . Adapted from [32].

It is at this point possible to define the MR signal  $S(t)$  as:

$$S(t) = \iiint_{xyz} M_{xy} e^{-iy \int_0^t (G_x(r)x + G_y(r)y + G_z(r)z) dr} dx dy dz \quad (1.17)$$

where  $G_i$  is the slope of the magnetic field on the  $i$ -direction:

$$G_i = \frac{\partial B_i}{\partial i} \quad (1.18)$$

Since after slice selection this signal no longer depends on the  $z$ -direction, equation 1.17 can be reduced to:

$$S(t) = \iint_{xy} M_{xy} e^{-i\gamma \int_0^t (G_x(\tau)x + G_y(\tau)y) d\tau} dx dy \quad (1.19)$$

Finally, an important formalism to understand how the acquired two-dimensional matrix is converted into the final image is the k-space concept, developed by Ljunggren [33]. Defining the axes of this k-space as  $k_x$  and  $k_y$ :

$$k_x(t) = \frac{\gamma}{2\pi} \int_0^t G_x(\tau) d\tau \quad (1.20)$$

and

$$k_y(t) = \frac{\gamma}{2\pi} \int_0^t G_y(\tau) d\tau \quad (1.21)$$

where  $x$  and  $y$  are the frequency and phase encoding directions, respectively, it is possible to write equation 1.17 as:

$$S(t) = \iint_{xy} M_{xy} e^{-i2\pi k_x(t)x} e^{-i2\pi k_y(t)y} dx dy \quad (1.22)$$

From this equation, it is possible to conclude that the k-space data and the image data are related through a 2-D Fourier Transform (FT). This means the acquired MR data can be used to fill the k-space, which can posteriorly be 2-D Fourier transformed into the final image.

Considering the k-space as a grid, its  $k_x$  and  $k_y$  axes represent spatial frequencies. Thus, a point  $(k_x, k_y)$  in k-space does not correspond to a specific position  $(x, y)$  of the final image, but rather it contains information on both spatial frequency and phase of every pixel of the final image [34]. The most common and easily understandable method to fill k-space is the Cartesian method. Through this process, each line of the k-space will correspond to a digitized MR signal acquired in a specific phase encoding, making the phase information along the  $y$ -axis. Conversely, the frequency information will be encoded along the columns, or  $x$ -axis [35].

Rows near the center of k-space encode low-frequency spatial frequencies. This translates into the “image bulk”, or global shape of the image. Contrastingly, rows near the upper or lower edge of the k-space will encode higher spatial frequencies, which after the 2-D Fourier Transform will be converted into the sharp edges and finer details of the image. In Figure 1.7, there is a schematic representation of the filling of k-space.

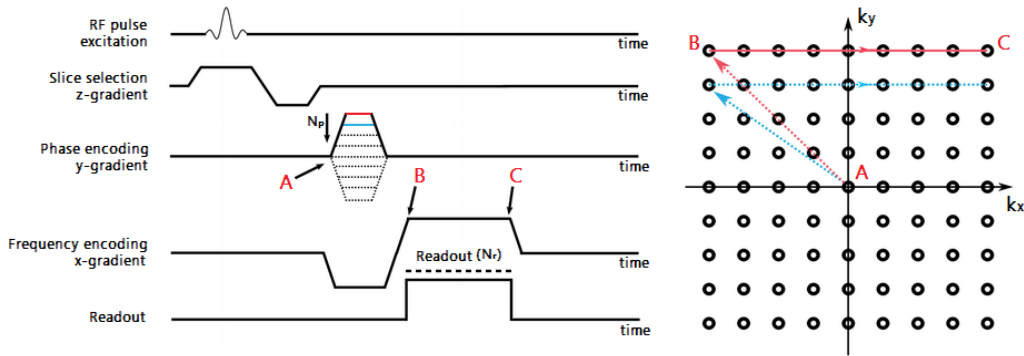


**Figure 1.7:** K-space cartesian filling. (Left): Pulse sequence with specific highlighted timepoints, and (Right) its corresponding k-space trajectory. (A): The trajectory begins at the center of the k-space, before any gradient is applied. (B): K-space trajectory was moved towards the  $+k_y$  direction, due to the phase encoding gradient, which determines the k-space row being filled. The negative frequency-encoding gradient moved the trajectory in the  $-k_x$  direction. (C): A k-space line is filled, along the frequency-encoding direction. After the red trajectory is finished, the same process will take place, but this time with a different phase encoding gradient (represented in blue, in both the pulse sequence representation, and k-space trajectory). Adapted from [32].

The k-space also has a direct relationship with the field of view (FOV) of the final image, and its resolution. The spacing between adjacent k-space points is inversely proportional to the final image's FOV. On the other hand, the size of the k-space - the difference between the maximum and minimum values of k-space - is inversely proportional to the final image's pixel size, i.e. if the k-space covers a larger range of values, the image will have a smaller pixel size (a higher resolution).

### 1.2.2.C. Image Contrast and Primary MRI Pulse Sequences

As mentioned in the previous subsection, time constants  $T_1$ ,  $T_2$  and  $T_2^*$  determine the obtained signal for each tissue. Therefore, they should be considered upon imaging, so as to choose suitable parameters for the pulse sequences, to obtain appropriate image contrasts. The most important parameters would be the Echo Time (TE), which is the time between the RF pulse application and the MR signal acquisition, and the Repetition Time (TR), which is the time between successive RF pulses, as depicted in Figure 1.9. Manipulations on both TE and TR originate different tissue contrasts. In Figure 1.8 it is possible to observe how the different relaxation times can originate these contrasts.

| Tissue              | $T_1$ (ms) | $T_2$ (ms) |
|---------------------|------------|------------|
| White matter        | 600        | 80         |
| Gray Matter         | 950        | 100        |
| Cerebrospinal Fluid | 4500       | 2200       |
| Muscle              | 900        | 50         |
| Fat                 | 250        | 60         |
| Blood               | 1200       | 100-200*   |

**Figure 1.8:** Different tissue contrasts. (Left): Table with typical  $T_1$  and  $T_2$  relaxation values at 1.5T (\* For  $T_2$  values of blood, higher value applies to arterial blood, and lower value to venous blood), and (Right): T1- and T2-weighted images, with a CSF region highlighted. Adapted from [36] and [37].

For example, CSF has extremely high  $T_1$  and  $T_2$  values. Thus, in an image based on  $T_1$  contrast ( $T_1$ -weighted), it appears as a darker region, as it takes longer than other tissues to recover its magnetization. Since it also takes longer to lose its transverse magnetization component, in a  $T_2$ -weighted image, it appears as a brighter region.

Briefly, a pulse sequence can be based on two of the elementary pulse types used in MRI: Gradient Echo (GE) or Spin Echo (SE), both represented in Figure 1.9.

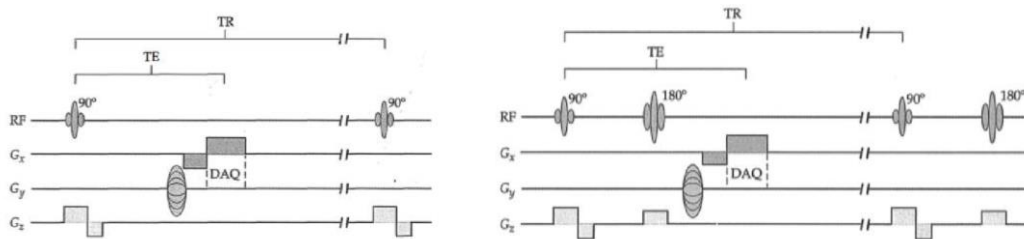


**Figure 1.9:** Primary MRI pulse sequences. (Left): Gradient-echo sequence and (Right): Spin-echo sequence. TE: Echo Time, TR: Repetition Time, DAQ: Data acquisition. (Adapted from [26]).

GE sequences use gradients to refocus the MR signal and are susceptible to inhomogeneities of the magnetic field. Therefore, they are dependent on the  $T_2^*$  time constant and are prone to signal losses and distortions (off-resonance artifacts), particularly in transitions between tissues or air-filled cavities.

SE sequences also begin with a  $90^\circ$  excitation pulse but applies a supplementary  $180^\circ$  refocusing pulse (combined with an additional slice selection gradient), which cancels the effect of the spatial magnetic field inhomogeneities and reverses the loss of phase coherence. Thus, SE sequences are dependent on the  $T_2$  time constant.

### 1.3. Functional Magnetic Resonance Imaging

A functional magnetic resonance imaging (fMRI) experiment allows the indirect imaging of brain function. This is typically achieved through the use of the Blood Oxygenation Level Dependent (BOLD) contrast. In order to gain a better understanding of fMRI, and more specifically, resting-state fMRI, it is useful to grasp the basic concepts of this contrast. In this section, the basis of the BOLD contrast and its imaging will be explained. Afterwards, resting-state fMRI will be introduced, as well as general considerations on its analysis.

#### 1.3.1. The Blood Oxygenation Level Dependent Contrast

In 1936, L. Pauling discovered that hemoglobin oxygenation state strongly influenced its magnetic properties [38]. More specifically, that oxygenated hemoglobin (Hb) is diamagnetic, and deoxygenated hemoglobin (dHb) is paramagnetic. Paramagnetic substances attract and, consequently, distort the magnetic field surrounding them, even if on a small scale. This causes the neighboring protons to be affected

by magnetic fields of slightly different intensities, thus precessing at different frequencies. Subsequently, this results in a faster transverse magnetization decay, which is translated into a shorter  $T_2^*$ , as experimentally proven for high magnetic fields in the 80s [39]. A few years later, it was hypothesized that a manipulation of the proportion of oxygenated and non-oxygenated blood could alter visibility of blood vessels on images that relied on  $T_2^*$  contrast ( $T_2^*$ -weighted images), and it was demonstrated that deoxygenated blood decreased the acquired MRI signal in  $T_2^*$ -weighted images [38][39]. This led to speculation that this blood-oxygenation level dependent contrast might be valuable in the indirect identification of active brain areas through two possibly complementary processes. Firstly, neuronal activity enhances oxygen consumption in that area. For a static blood flow, this would cause an increase of deoxygenated hemoglobin (dHb). Secondly, an increased blood flow might reduce the amount of dHb, if there is no increment on the metabolic demand [25]. These theories were proven accurate with time, although the mechanism behind the BOLD contrast was actually shown to be more intricate than originally thought, and to this day is still not fully understood [42].

#### 1.3.1.A. Neuronal Activation and its Hemodynamic Effects (Neurovascular Coupling)

Neurons are the main components of the nervous system and can be divided into three parts. These are the dendrites, which receive inputs from other neurons; the soma, also known as the cell body, which contains the nucleus and organelles of the cell; and the axon, in which the electrical impulses are transmitted to other neurons. This signal transmission occurs in specific junctions denominated synapses and are also regulated by supporting non-neuronal cells such as glial cells (or glia).

The synaptic process begins when the presynaptic neuron releases chemicals which travel through the synaptic gap, i.e. the space between pre and postsynaptic neurons, and are detected by receptors on postsynaptic neurons. These chemicals, better known as neurotransmitters, are responsible for inducing changes in the permeability of the membrane of the postsynaptic neuron. It is important to note that, due to active pumps (transport systems which require energy input to move ions across their concentration gradient) there is a higher concentration of  $K^+$  inside the neuron resting membrane, and a higher concentration of  $Na^+$ ,  $Ca^{2+}$  and  $Cl^-$  outside [25], which causes the neuron's membrane to be polarized (typically at a resting potential of approximately -70 mV). The changes in permeability caused by neurotransmitter reception can occur through the opening of ion channels, such as  $Na^+$  channels, which are usually closed. This causes the ions to move towards their concentration gradient, depolarizing the membrane. If a certain potential threshold is reached, an action potential is triggered, and the membrane will depolarize completely, transmitting the electrical impulse. Afterwards,  $K^+$  channels, which are closed in a resting neuron, will also open. This allows the membrane to restore its resting potential. However, to ensure that further action potentials can be propagated, it is necessary to restore the initial ion concentrations. This is accomplished through the use of pumps, notably the sodium-potassium pump, which returns the ions to their original concentrations, but requires energetic input. [25]

It is well established that, although it has a low energetic storage ability, the brain is the organ with the highest energetic demand [1], mostly due to the energy needed to restore the resting potentials following synaptic activity [43]. Adenosine triphosphate (ATP) is the primary energy source of biological systems, and it can be produced in the mitochondria by aerobic processes. These require two components: glucose and oxygen. Thus, in order to meet its strong energetic demands, the brain needs an external continuous source of glucose and oxygen.

This continuous supply is provided by the complex vascular system of the brain. There are two main arterial systems that supply the brain with oxygenated blood: the internal carotid arteries (right and left), and the basilar artery. These systems are merged in what is denominated as the circle of Willis, which is then branched into cerebral arteries, which supply blood to separate brain regions. The jugular veins are responsible for venous drainage in the brain. [25]

In a microcirculation scale, it is known the cortical blood supply originates from meningeal arteries. These arteries ultimately branch into much smaller arterioles, which permeate the cortex perpendicularly to its surface, perfusing it with multiple capillaries. After the oxygen diffusion into the tissues, and carbon dioxide diffusion into the bloodstream, deoxygenated blood is drained by ascending and pial veins, as schematically represented in Figure 1.10. It should also be noted that the vascularization density is not homogeneous across cortical layers, and a higher density of blood vessels can be observed in regions with a higher neural cell density [25].

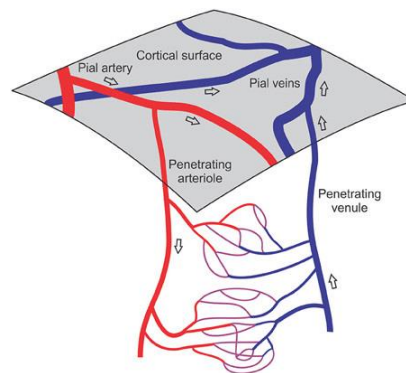


**Figure 1.10:** Cortical vasculature on a microscopic level. Extracted from [44].

Blood flow can be considered as the volume of traversing blood in a given time interval. To ensure its control, resistance vessels allow for a steady flow to pass to the capillaries by opposing said flow. There are several factors influencing the resistance of a vessel to blood flow, namely: vessel length, blood viscosity and, the most impactful aspect, vessel diameter [45].

Neuronal activity can influence this flow by causing the release of vasoactive substances such as nitric oxide, which cause vessel dilation. The vessels' enlarged diameter provokes a lower resistance, increasing blood flow. The action of both resistance vessels and this vasodilation mechanism work coordinated to maintain a controlled blood flow. Even though the focal point of neuronal activation is where the majority of the blood flow changes occur, they can also be observed in other locations, where there is

no synaptic activity. This means there is an inherent spatial specificity limitation on measuring the BOLD signal [25].

### 1.3.1.B. The BOLD Signal

After grasping the essential concepts of neuronal activation and its hemodynamic effects (also referred to as neurovascular coupling), it is necessary to understand how these effects impact the acquired MR signal. As previously mentioned, the BOLD contrast is based on differences in the proportion of oxygenated and de-oxygenated blood.

Firstly, a local field potential (LFP) is the sum of excitatory and inhibitory potentials in the area of the recorded region, and it is thought to be reflected more accurately in the BOLD signal, rather than individual neuronal spikes [42][46]. Considering an area with strong neuronal activity, the increased blood flow will allow a higher supply of oxygenated blood to reach the area. Since the oversupply of oxygen is much larger than the increased consumption in the active brain region, this results in a higher amount of oxygenated blood, and consequently oxygenated hemoglobin (Hb) compared to deoxygenated hemoglobin (dHb) in the region. Since dHb leads to a faster dephasing and consequent loss of MR signal, reflected in a  $T_2^*$  shortening, the activated brain region, where there will be a higher concentration of Hb, will have a stronger measured MR signal and appear brighter in the final MR image.

It can be acknowledged that the BOLD signal reflects a complex interaction of changes in the cerebral metabolic rate for oxygen (CMRO<sub>2</sub>), as well as cerebral blood flow (CBF) and cerebral blood volume (CBV). These factors influence the fluctuations in the MR signal in  $T_2^*$ -weighted images, which can be characterized by the hemodynamic response function (HRF). The common HRF has three main phases, as depicted in Figure 1.11 (as modelled for the human brain).

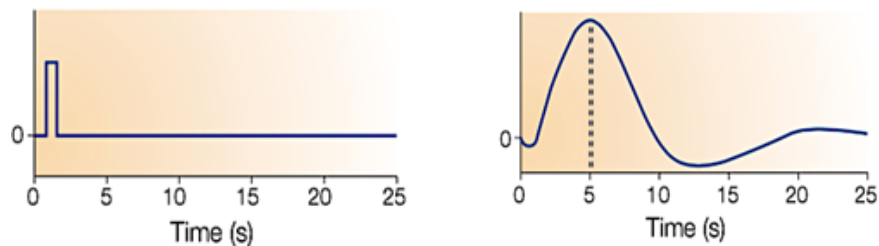


**Figure 1.11:** The Hemodynamic Response Function (HRF). (*Left*): Neuronal activation and (*Right*): consequent BOLD response. Adapted from [47].

Starting with the initial dip, it is not always observed, but it is more often detected at high magnetic field strengths. It is thought to reflect the initial metabolic extraction i.e. the oxygen consumption in the brain tissue, which leads to a higher proportion of dHb, reducing the BOLD signal. Although the origin and “behavior” of this dip not yet fully understood, it remains an attractive focus of research, as it has an inherently higher spatial specificity, when compared to the large peak, and it is hypothesized to reflect more

closely neuronal activity [48]. However, it can be observed that this peak only occurs a few seconds after the neuronal activation occurs, so it can be considered that the BOLD response is slow and has an inherently limited temporal specificity.

Following this initial dip, there is an over compensatory response, and there is an increase of CBF to cope with the demanding metabolic needs. This will result in a steep increase of Hb, which translates into a BOLD peak. This is the bulk of the BOLD response, and it can be rather slow and delayed.

Finally, the post-stimulus undershoot is also quite variable and its mechanisms not fully understood. It is thought to be caused by an abrupt decrease in CBF after the neuronal activation, but with a slower decrease of CBV. The reduced CBF in a comparably high CBV cause a temporary undershoot, which tends to stabilize as the CBV recovers. It should be noted that the HRF shape are known to greatly vary according to many factors, such as age, anesthesia and species [49][50].

### 1.3.2. BOLD Signal: Imaging Considerations

Considering some intrinsic features and limitations of the BOLD signal, there are several factors that need to be taken into account when performing functional MRI.

Since functional changes in the BOLD contrast occur in a time frame on the order of a few seconds, functional images must be acquired in a temporal resolution suitable for properly resolving these signal fluctuations. Structural images, on the other hand, are aimed to have a higher spatial resolution, as there are no time constraints for recording structural parameters.

When analyzing and drawing conclusions from fMRI studies, it is crucial to keep in mind that BOLD contrast is an indirect measure of neuronal activity, and cannot differentiate between feedforward and feedback signals, as well as between excitatory and inhibitory signals [51]. Still, if correctly exploited, fMRI can be a powerful and insightful tool for studying function in the brain.

#### 1.3.2.A. Gradient-Echo and Spin-Echo Sequences

GE sequences are frequently used in fMRI experiments, since they are sensitive to  $T_2^*$  contrast. Therefore, they are affected by magnetic field inhomogeneities, and susceptible to signal losses and image distortions, which occur particularly at transitions between tissues or air-filled cavities. These artifacts, also known as off-resonance artifacts, become particularly relevant when considering the mouse brain, where there is a low volume proportionally to the mouse brain area [52], and a high ratio of air space to volume of tissue [20]. The use of shimming coils might attenuate these inhomogeneities' effects, as they optimize field homogeneity, but their performance is better in lower strength magnetic fields. Additionally, GE sequences are less spatially specific, as they might reflect hemodynamic effects from large vessels. This might cause BOLD signal detection in areas where no neuronal activation occurs.

SE sequences reflect more accurately changes in the vasculature on a microscopic level instead of large vessels and are consequently more spatially specific. However, they are sensitive to  $T_2$  contrast, which translates into a lower BOLD sensitivity, and a subsequent lower obtained MR signal [25].

The choice between a GE or SE sequence depends on the purpose and context of the study being performed.

### 1.3.2.B. Temporal Resolution

There are several sequences that can be used, when considering the need for high temporal resolution acquisition. One of the most popular and standard sequences used, developed in 1977 by Mansfield and colleagues [53], is the Echo Planar Imaging (EPI). The so-called “single-shot” EPI allows the acquisition of all the lines of k-space with a single excitation. This greatly reduces the acquisition time of each image. This is accomplished by filling the k-space in a “back and forth” pattern, which results from alternating frequency-encoding gradients, with short phase-encoding bursts, or “bleeps”, as can be seen in Figure 1.12.

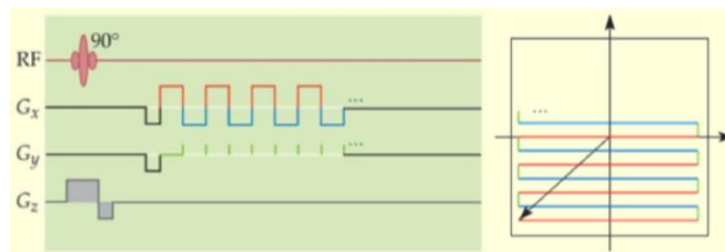


**Figure 1.12:** GE-EPI sequence. (Left): A blipped GE-EPI sequence and (Right): its corresponding k-space trajectory. The red k-space lines are resultant from red part of the frequency-encoding gradients (positive), and analogously, the blue k-space lines result from the blue part of the frequency-encoding gradient (negative). The phase-encoding bleeps are responsible for shifting the trajectory to the next line. Extracted from [25].

Multi-shot EPIs are based on an identical principle but acquire partial blocks of the k-space in each shot. For example, a two-shot EPI acquires the full k-space from 2 RF pulses. Although it does not reduce acquisition as significantly, it has been shown to be less susceptible to off-resonance artifacts [54].

Even though the main concern when acquiring a functional image is indeed the high temporal resolution, spatial resolution cannot be completely overlooked. To acquire images with a reasonable spatial resolution, a significantly large k-space must be filled in a rather short time period, since the entire image must be acquired before a meaningful transverse decay. Thus, the gradients need to be very rapidly shifted, which is extremely burdensome on the hardware. Additionally, EPI sequences are highly susceptible to inhomogeneities on the magnetic field, which, as previously mentioned, can cause image distortions and signal losses. These are more visible and severe in air-tissue interface areas, i.e. the frontal cortex and temporal lobes in humans, or the olfactory bulb and the cerebellum, in mice [20].

It is also possible to consider other kinds of sequences instead of the EPI. There are techniques which only acquire a partial k-space sampling, such as conjugate mirroring, or which have more effective k-

space trajectories, like the Spiral (which less taxing on the gradients compared to the EPI) [25]. Sequences such as SPEN or HASTE have also been used in fMRI studies [55][56]. They all have pros and cons, compared to the GE-EPI, but an exhaustive description of these pulse sequences is not on the scope of this project.

Regarding more practical issues, the temporal resolution is restricted by the repetition time (TR) and the biological variations due to the neurovascular coupling. By reducing TR, the number of slices that can be acquired per repetition is also reduced. Additionally, TR shortening increases the sampling rate, but forces the flip angle to be decreased. Therefore, the time required for a complete longitudinal magnetization recovery can be reduced, but the transverse magnetization decreases as well. Thus, there will be a lower obtained MR signal. The Ernst angle  $\alpha_E$ , given by:

$$\alpha_E = \cos^{-1} \left( e^{-\frac{TR}{T_1}} \right) \quad (1.23)$$

should ideally be chosen as the flip angle, so that the Signal-to-Noise ratio (SNR) is maximized for a given TR, and a given average  $T_1$  on the tissue of interest. It can be noted that when  $TR \gg T_1$ , the Ernst angle  $\alpha_E$  will be approximately 90-degree, as could be anticipated since, if there are no time constraints, the 90° pulse will result in the maximum transverse magnetization.

### 1.3.2.C. Spatial Resolution

The spatial resolution of an MR image is defined by its voxel size, which can be computed from the FOV, matrix size (the number of rows and columns that constitute the image) and slice thickness. However, although a smaller voxel size translates into a higher spatial resolution, it also results in a lower measured signal, i.e. a lower SNR. Furthermore, in order to decrease voxel size, more k-space lines must be acquired, which results in a longer acquisition time, and consequently a lower temporal resolution. Yet, if the voxel size is larger, more partial volume effects (PVE) will occur. Even considering that a region of interest in a single tissue will have an approximately homogeneous signal, if a voxel contains multiple tissues, the signal measured from that voxel will be a weighted average of their individual signals. This becomes a more relevant issue when considering, for example, small structures in the brain. If the resolution is not high enough, it is impossible to accurately measure BOLD signal contributions from a small region, as its signal might be diluted in the surrounding tissue's.

In the context of small rodents imaging, spatial resolution is a critical aspect. Considering that the MR signal is dependent of the number of protons which are contributing to the signal, this means that a smaller sized body will result in a lower acquired signal. This is problematic considering that, especially when compared to an average human brain, the mouse brain is extremely small (typically with a volume no larger than 600mm<sup>3</sup> [57]). Thus, in order to obtain a reasonable spatial resolution when imaging mice, the voxel size must be very small, which greatly limits the achieved SNR. To overcome this challenge, high intensity magnetic fields can be used, to increase the obtained signal. One additional factor that may prove

crucial is the use of cryogenic coils. They can be based, for example, on a closed cycle helium cryocooler, which cools down the coil. Thus, thermal noise contributions resulting from the electrons' thermal motion in the conductors are reduced, which leads to an increased SNR. This enhancement is a possible way of dealing with the demanding signal sensitivity associated with rodent imaging [58].

### 1.3.3. Blocked and Event Related Experimental Designs

A suitable and optimized experimental design is crucial for an efficient fMRI study, especially considering the time-consuming and extensive resources required for a successful data acquisition and analysis. Typically, in fMRI, there are two commonly used designs: blocked and event related.

Briefly, blocked designs are based on using different conditions, alternated in distinct blocks. For example, blocks of a resting condition can be interleaved with blocks of a stimulus condition, and BOLD responses are compared between the two blocks. This design is powerful regarding detection of activation, but the summation of the hemodynamic response across time must be considered, as there can be habituation issues [25].

Event related designs rely on events, separated by a varying interstimulus interval. These designs are therefore more flexible and focus on measuring neural activity occurring for very brief periods of time. Their detection power is weaker, comparing to blocked designs, although they allow the determination of the HRF shape, unlike the latter [25].

### 1.3.4. Resting State Functional Magnetic Resonance Imaging

Resting-state fMRI (rsfMRI) is a technique that has been steadily growing over the last years [2], and it is based on measuring spontaneous BOLD signal fluctuations when the subject is not performing any cognitive task or responding to sensory stimuli. Applied for the first time in 1995 in humans [59], rsfMRI has also been used in rats [60], and more recently in mice [61]. This tool allows the study of the intrinsic activity of the brain, and its inherent organization and functioning, as well as different arousal states and diseases [4]–[6][62]. Besides, it allows the mapping of reliable networks across subjects in a single acquisition [63].

Functional connectivity (FC) can be defined as the temporal correlation of the resting state activity between spatially distinct regions of the brain and can be extracted from rsfMRI experiments. Typically, it is possible to identify regions which appear as functionally connected and are known as Resting State Networks (RSNs). In humans, these networks can be found consistently across subjects, and specifically, the Default Mode Network (DMN) is the most commonly studied and more robustly reproduced [64][65]. Representative networks can be seen in Figure 1.13.

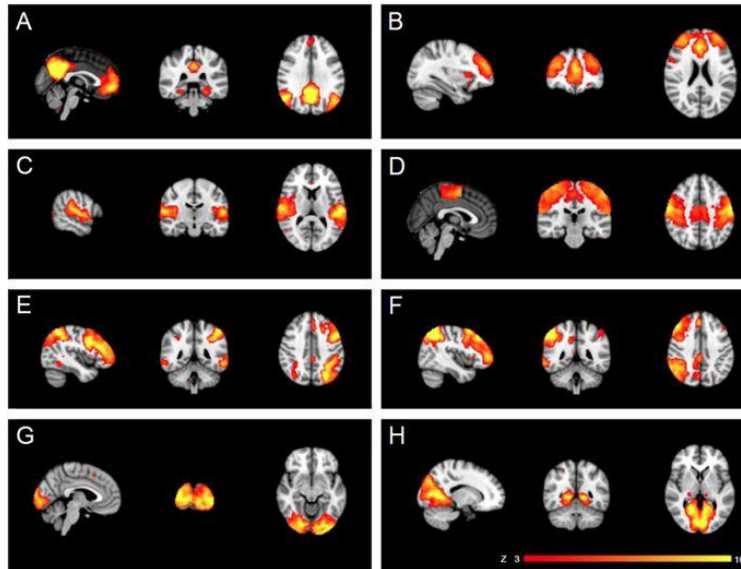


**Figure 1.13:** Typical RSNs in the human brain. Sagittal, coronal and axial slices on a standard space are shown, and the Default Mode Network (DMN) can be observed in (A). Extracted from [66]

Since BOLD signal is an indirect measure of hemodynamic activity, there has been research towards the validation of the neural basis of the rsfMRI signal. Indeed, growing empirical evidence shows that rsfMRI signal seems to have an electrophysiological origin [67]–[70]. However, unlike stimulus evoked fMRI, resting state fMRI is a paradigm-free method, making the removal of spurious noise especially important.

Additionally, in animal experiments, the use of anesthesia can heavily impact vasculature response, further challenging the interpretation of rsfMRI results. Thus, the bias of noise and the anesthetic are both crucial issues that need to be considered when choosing a suitable protocol for preclinical resting state imaging and subsequent analysis. These issues will be addressed in the following sections.

### 1.3.5. Analysis of Resting State fMRI Data

Functional MRI is, in general, a noisy technique. This is aggravated in the case of resting state fMRI, due to its model-free and data-driven exploratory nature. The presence of various confounding factors can severely hamper the obtained results and their interpretation. For example, one of the most problematic sources of noise is head motion, which is difficult to completely avoid, and results on the misalignment of the volumes within the timeseries. This can, and must be, corrected, since the following analysis is often based on the assumption that the same voxel in each volume represents the same spatial location. Besides this misalignment, head motion raises more intricate complications since it changes field inhomogeneities (which render the action of shimming coils suboptimal) and the spins' precession on specific locations, causing local BOLD abnormal changes and so-called spin-history effects. These are more difficult to correct

for, so head motion should be minimized as much as possible [62]. Hardware noise and physiological factors such as heart rate or breathing are other issues which can contaminate measured MR signal.

Therefore, it is essential to apply a series of preprocessing steps in order to decrease data variability unrelated to the experiment, before extracting functional connectivity information from a rsfMRI study.

#### 1.3.5.A. Preprocessing

There are several typical preprocessing steps that can be applied to the raw resting state data. Some of the most commonly used ones will now be briefly described:

**Quality control** is crucial in any fMRI study, and it is used to verify that all following steps are properly applied, as well as to prevent error propagation. It includes inspecting raw data and data after each correction, to ensure there are no abnormal spikes or artifacts which may compromise the final results.

**Slice-timing correction** is performed to correct for the difference in the time of each slice acquisition, within the same TR. It uses interpolation in time to shift the BOLD time courses slightly, to correct for this small difference. For acquisitions with a very short TR ( $\leq 1$  second), it is generally not advisable to perform slice-timing correction, as the use of interpolations should be avoided, and considering the slowness of the hemodynamic response, the difference on slice acquisition time might be negligible [62].

**Motion correction** algorithms align each volume of the time series to a reference volume (e.g. the first acquired volume) by applying a rigid transformation which minimizes a cost function. They return six motion parameters (three for each translational direction – x, y and z, and three for each rotational movement – pitch, yaw, and roll). Considering that, head motion is practically unavoidable and extremely problematic, and it might even cause spurious correlations between regions, this step is extremely important should be always performed [62]. It should be noted that in mice, motion can be minimized using a bite bar and ear bars to fixate the head, but some movement might still be difficult to avoid. Considering their very high heart and respiratory rate (600 beats per minute and 150 breaths per minute, respectively) [18], this could result in a higher susceptibility to motion effects, due to enhanced pulsatory forces [71].

**Bandpass temporal filtering** is a conventional step applied in fMRI studies. A high pass temporal filter is used to remove slow drifts caused by the scanner hardware [62], while the low pass filter is applied to remove noise fluctuations, since functional connectivity is thought to be correlated with low-frequency BOLD oscillations. Thus, classic cut-off frequencies of these bandpass filters are 0.01-0.1Hz (for high- and low-pass filtering, respectively). It has been repeatedly shown that functional connectivity is driven by signal fluctuations at these frequency range, both in humans and rodents [72][73]. Additionally, there is currently a consensus that bandpass filters used in rsfMRI should be similar, across species [74]. There is some evidence, however, that higher frequencies might also include relevant functional connectivity information [62][71][21], and as such, a higher low-pass frequency cut-off ( $\sim 0.2$  Hz) can also be considered [73].

**Spatial smoothing**, or spatial filtering, is commonly applied in many fMRI studies. In each voxel, a weighted average on neighboring voxels is computed, blurring the image. This weighting can be created by

a Gaussian kernel, and its full-width-half-maximum (FWHM) defines the amount of smoothing to be applied. The smoothing should be minimal to the particular study being conducted, since, although the averaging might reduce some noise (increasing the image SNR), it also results in a loss of spatial accuracy, which is particularly relevant when focusing on a small region of interest [62].

**Normalization** is a crucial step if there is the need for all the subjects to be in a “standard” space, as it is common in most studies conducting group analyses. Firstly, the functional images are registered onto higher resolution anatomical images, within the same animal. Then, the images in the structural space are warped to match as closely as possible the shape of a standard image (e.g. a brain atlas). Since linear transformations only help on a superficial level, to achieve a suitable registration, non-linear algorithms are recommended, as they allow the proper alignment of finer brain structures [62].

**Nuisance regression** is also a standard step, based on the removal from the data of variances associated with nuisance regressors, through a multiple linear regression. These nuisance regressors are time courses assumed to reflect signal from a non-neural source. The motion regressors outputted from the motion correction algorithm are commonly used as nuisance regressors, as well as signal from the ventricles or white matter. In mice, these regions are extremely small, so it can be hard to accurately define the regions from where to extract the timeseries [21]. It is also possible to regress out the average timeseries of the whole brain through global signal regression (GSR). GSR is a controversial step which assumes that this global component reflects noise, as neuronal activity is assumed to be localized [75]. There is a continuing debate on whether or not GSR should be performed, as there is growing evidence that it might introduce spurious anti-correlations between networks [76][77] and also that the global BOLD signal might be correlated with local neuronal activity [78].

Although there is currently no consensus on the best preprocessing pipeline, species specific considerations should be taken, i.e. although several steps are standard in human rsfMRI studies, they might not be appropriate in rodent studies [79].

#### 1.3.5.B. Postprocessing

After preprocessing the data, a functional connectivity analysis can be conducted.

One of the most popular methods to extract functional connectivity information from rsfMRI data is Seed-Based Analysis (SBA). In this technique, a “seed” or region of interest (ROI) is chosen. Then, its timeseries is compared with the timeseries of all voxels in the brain, typically by linear correlation. The output of an SBA should be a map displaying correlation values relating to the chosen seed, and it is generally considered that regions showing stronger correlation values are more functionally connected to the seed.

Some drawbacks of the SBA approach are that it is inherently a hypothesis-driven method, since its results are limited by the seed definition [62]. The shape, size and location of the seed are also aspects which can heavily influence the final connectivity maps [80][81]. Still, its straightforward interpretation and simplicity make it an attractive and widely used technique.

Another used tool in functional connectivity analyses is the Independent Component Analysis (ICA). This is a more data-driven approach that decomposes the four-dimensional rsfMRI data into independent components, composed by spatial maps displaying regions with a similar temporal pattern, and their respective timeseries [62]. Disadvantages of ICA include its dependency on the user-defined dimensionality (number of independent components to be identified). Additionally, difficulties may arise when manually classifying each component as a network or artifact. Still, it is considered a robust method, widely used in FC analyses [71][61], and the maps obtained with ICA appear to be mostly consistent with those found with SBA [82].

Other possible approaches for FC studies include Regional Homogeneity (ReHo) analysis [83], which provides information on local brain activity; Amplitude of Low-Frequency Fluctuations (ALFF) [84], which measures the amplitude of spontaneous BOLD variations in each voxel; and Graph Theory [85], which unlike the previous voxel-based analyses returning spatial maps, is a node-based analysis. This type of analysis allows the answering of questions more related to how different brain regions (nodes) are connected [62].

It should be noted that all these techniques assume a stationary FC. It is possible to study dynamic functional connectivity (dFC), which is a potential biomarker of multiple disorders, and it is predicted to have direct upcoming therapeutic applications [86], by using sliding window methods, or time-frequency coherence techniques.

Although a more detailed explanation of each of these methods is not considered to be in the scope of this thesis, it is clear that the vast variety of preprocessing steps, combined with the numerous ways to derive information from functional connectivity studies, render rsfMRI study comparison a difficult task.

#### 1.4. Anesthesia in Rodent fMRI Experiments

Although resting state studies have been carried out in awake animals, such as monkeys [10] and rats [87], imaging of awake mice has been more difficult to achieve [88], due to various factors, such as their motion, irregular breathing and heart rate. Also, despite intensive acclimation training, substantial animal distress must be taken into account. Thus, the use of awake mice in resting state studies remains a controversial matter [89].

Considering these issues, the use of anesthetics is a common procedure in preclinical experiments [90], as it ensures a proper restraint of the animals while reducing their distress. However, it has been shown that anesthetics might deeply influence cardiovascular, respiratory and thermoregulatory systems, consequently affecting neuronal activity and neurovascular coupling [91][92]. Moreover, resting state networks appear to be dependent on the type and dosage of the chosen anesthesia [21][89][92]–[94].

Preferably, the anesthetic regime should provide a stable sedation for an adequate time period for the image acquisition, always ensuring the animal's well-being. Special care must be taken when monitoring small rodents in MRI acquisitions, especially regarding their body temperature. The high surface to body

weight ratio makes mice especially prone to considerable heat losses, which can result in hypothermia – a recurrent cause for anesthetic complications and deaths [95]. Breathing patterns should also be monitored, as they are valuable indicators of the animal's current physiological status. Endotracheal intubation and ventilation can also be performed to stabilize the animal's breathing, and have been used in rsfMRI mice studies [89][96]. However, they are known to be very technically challenging, requiring specialized apparatus and extensive practice until adequate technique is accomplished [97].

Although there is no ideal anesthetic without limitations, several regimes have been used in rsfMRI. A common one, isoflurane, is a potent fast-acting volatile vasodilator anesthetic [98], which has severe respiratory and cardiovascular effects, limiting neurovascular reactivity [99]. It has been reported to result in poor FC patterns [91], although it has been used as an anesthetic to map functional patterns in rsfMRI [20].

In order to minimize these respiratory and cardiovascular effects, medetomidine sedation can be used. This  $\alpha$ 2-adrenoreceptor agonist has negligible effects on both systems [100], and its action can be quickly reversed by using  $\alpha$ 2-antagonist atipamezole, making it a suitable choice for various rsfMRI studies [101][93]. It has been shown to cause a prominent decrease of norepinephrine release and an overall inhibition in the sympathetic nervous system, as it acts mainly on presynaptic receptors in the Locus Coeruleus [100][102][103]. It has also been shown to be appropriate for the detection of bilateral FC in mice [93], although there is literature suggesting that a combined use of low dosages of medetomidine and isoflurane might be a more suitable alternative [89][91].

It should be noted that medetomidine sedation might not have a constant effect during the acquisitions and could result in altered functional connectivity over time [104]. Furthermore, several mouse strains have been reported to be resistant to this sedative [105].

Urethane is yet another suitable choice for rsfMRI studies. It is a long-lasting anesthetic, with minor cardiovascular and respiratory effects [106]. It has been shown to result in good FC patterns in rats, similar to awake animals [91], although there is also literature pointing otherwise in mice [89]. It should be noted that the apparently inconsistent findings in literature can be due to different dosages and methods used in the experiments.

A major drawback of urethane are its carcinogenic properties [107], making it a terminal anesthesia and not allowing longitudinal studies. Extreme care should be taken when manipulating this substance, and after the experiment the animal must be euthanized [108]. Thus, urethane is only recommended in particular situations, when other alternatives are not suitable for the specific project.

## 1.5. State of the Art of Resting State fMRI in Mice

The potential of resting state fMRI as a tool to extract information about functional connectivity was uncovered for the first time in humans. In 1995, Biswal and colleagues compared activation maps from subjects performing a motor task, and correlation maps using the activated areas as seeds. They noticed

strong spatial similarities, which suggested that intrinsic spontaneous BOLD fluctuations in a resting brain hold information on its functional organization [59].

The number of rsfMRI studies has exponentially grown ever since [2], and even if the majority of them have been performed in humans, there have been studies using murine models. Specifically, since 2008, studies mapping functional networks were conducted in rats [60], and since 2011 in mice [61].

A succinct description of the main rsfMRI experiments conducted in mice can be found in Table A.1 and Table A.2, in the Annexes. There, it is possible to compare further details on animal preparation, MRI acquisition and analysis pipeline. It should be noted that only the results and conclusions relating to the mapping of functional networks are discriminated, as several studies had a wider focus of research, not considered on the scope of this thesis.

In 2011, Jonckers et al. used the mouse model for the first time in an rsfMRI study, applying an ICA approach to identify murine networks [61]. Using a medetomidine sedation regime, they found that the resting state networks (RSNs) showed strong dependency on the number of components defined by the user, and that mice networks seemed to be more unilateral, whereas the rat's RSNs showed bilateral components.

Later, in 2013, by using only isoflurane as anesthetic, Guilfoyle et al. were able to map mice functional networks [20]. By using a seed-based analysis (SBA), they found evidence of a "Default Mode Network"-like network for their cortical seeds, although the results were more unclear for insular and prefrontal seeds, as they only showed a more focused network. However, the very large voxel size and consequent low spatial specificity was considered one of the major drawbacks.

As previously discussed, the anesthetic regime has been a matter of debate, and has been shown to alter FC, namely in rats [91]. Thus, in 2014, Grandjean et al. compared networks found in mice under different anesthetics (isoflurane, propofol, medetomidine and urethane) [89]. Through an SBA approach, they mapped mice functional networks, and compared mean connectivity values between bilateral regions. While isoflurane, propofol and urethane showed bilateral correlation for cortical seeds, striatal connectivity did not seem to be compromised. Medetomidine, in contrast, showed bilateral striatal connectivity, but a low cortical bilateral connectivity. An anesthetic regime using a combination of low dosages of medetomidine and isoflurane was found to deliver the higher bilateral connectivity, both cortical and striatal. The data acquired in this study was later studied by Bukhari et al. in 2017 who, by using ICA, network modelling and dual regression, reached similar conclusions, namely regarding the use of medetomidine and isoflurane combined to obtain bilateral FC patterns [96]. The same dataset was again used in 2017 by Wu et al., who used a ReHo analysis to further investigate anesthesia effects [109].

Considering that different dosages of the same anesthetic could have different effects on mice RSNs, in the same year, Nasrallah et al. compared different dosages (0.1/0.6/1 mg/kg/h) of medetomidine and their effects on murine networks [93]. For the two lower dosages (0.1 and 0.6 mg/kg/h), bilateral networks were found using six seeds (two striatal and four cortical) in an SBA approach. The highest dosage (1 mg/kg/h) was found to result in a significantly lower interhemispheric connectivity, and even in poor animal recovery. An example of the bilateral maps obtained in this study can be seen in Figure 1.14.

Other interesting works in this field include the 2015 study by Zerbi et al.. Motivated by the great preprocessing pipeline variety, the authors were able to validate an automatic artifact component classification and data cleaning algorithm based on ICA, named FIX [110]. Additionally, in 2016, Sforazzini et al. observed differences in the networks of “normal” and BTBR mice, which is a transgenic mouse model for autism [111].

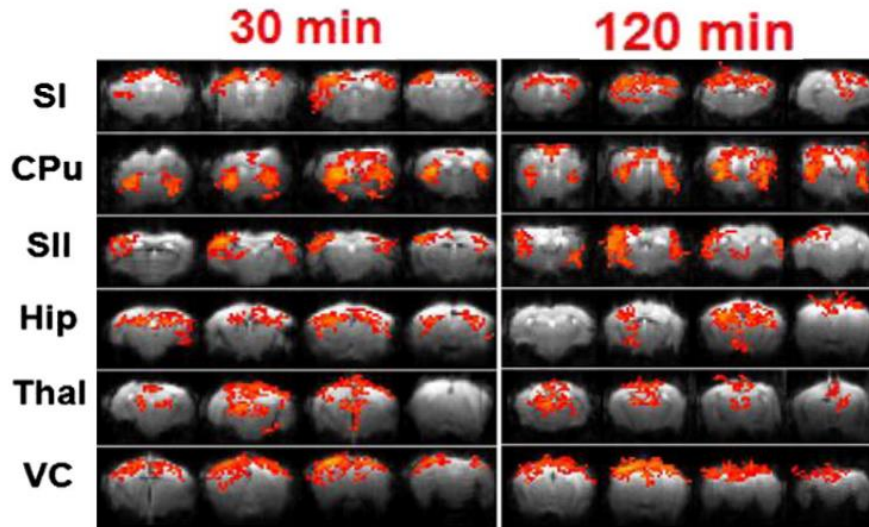


**Figure 1.14:** Final connectivity maps obtained with a 0.6mg/kg/h medetomidine dosage, at two time points, in six seeds. S1 – Primary somatosensory area, CPu – Caudate Putamen, S2 – Secondary somatosensory area, Hip – Hippocampus, Thal – Thalamus, VC – Visual cortices. Adapted from [93].

More recently, in 2019, a multicenter study was conducted, where it was possible to compare a wide variety of preprocessing pipelines, anesthetic regimes and animal preparation protocols. Grandjean et al. suggested that, using a universal and robust pipeline, large-scale networks could still be observed in most of the used datasets [112]. Still in 2019, a very high-resolution rsfMRI study was conducted in mice, and although no networks were mapped, it was possible to analyze data using a connectivity matrix of 52 segmented regions, and ALFF [84].

Resolution in these studies usually ranged from 0.23 mm × 0.23 mm to 0.469 mm × 0.469 mm, with a non-isotropic pixel dimension found in [61] (0.16 mm × 0.31 mm). An exception to this exists [84] (0.1 mm × 0.1 mm), but no functional network mapping was carried out, and the brain was segmented into 52 areas, averaging signals in ROIs with 80 to 2000 voxels, making the effective resolution of the studied areas quite smaller.

All these studies conducted in mice in the last years suggest that although mostly bilateral functional networks have been observed, agreement on anesthesia and preprocessing has not yet been reached. Moreover, murine rsfMRI acquisitions have been performed under a large variety of settings, including different animal preparation, field strengths, coil type, MRI parameters, rendering study comparison difficult and sometimes filled with inconsistencies.

## 1.6. Thesis Objectives

As reported, the variety of pipelines and settings used to conduct rsfMRI studies in mice, and their typical low spatial resolution are current limitations of this field. Additionally, fMRI experiments are typically carried out with a medetomidine sedation regime, which, as it was previously stated, affects the locus coeruleus (LC) noradrenergic system, which is of interest to specific researchers in the lab. Since no resting state experiments had been performed in the lab, so far, and the LC itself is a very small structure, this project aims to:

- Establish an MRI protocol in the current lab, adequate for rsfMRI acquisition in mice;
- Explore urethane anesthesia in mice, to facilitate LC imaging;
- Establish and optimize a robust preprocessing and analysis pipeline that allows mapping of mice RSNs;
- Validate the pipeline through replication of results consistent with previous works;
- Observe consistent RSNs in mice on higher resolution datasets, towards the study of smaller structures, such as the LC.

## 1.7. Thesis Outline

This thesis is organized in five main sections. The present one aims to provide a motivational perspective on this project, the theoretical background required for its understanding, and an overview of the relevant literature on this field. Section 2 describes the protocols and methods used in this work. In Section 3, the results of the optimization stage and the later stage of rsfMRI acquisition are shown. Section 4 presents the discussion of the results previously displayed. Finally, main conclusions and considerations on possible future work are provided in Section 5.

## 2. Materials and Methods

This chapter describes the protocols and methods used in this work. Specifically, it presents in detail the steps optimized and used to perform rsfMRI acquisitions. These are also depicted in Figure 2.1.

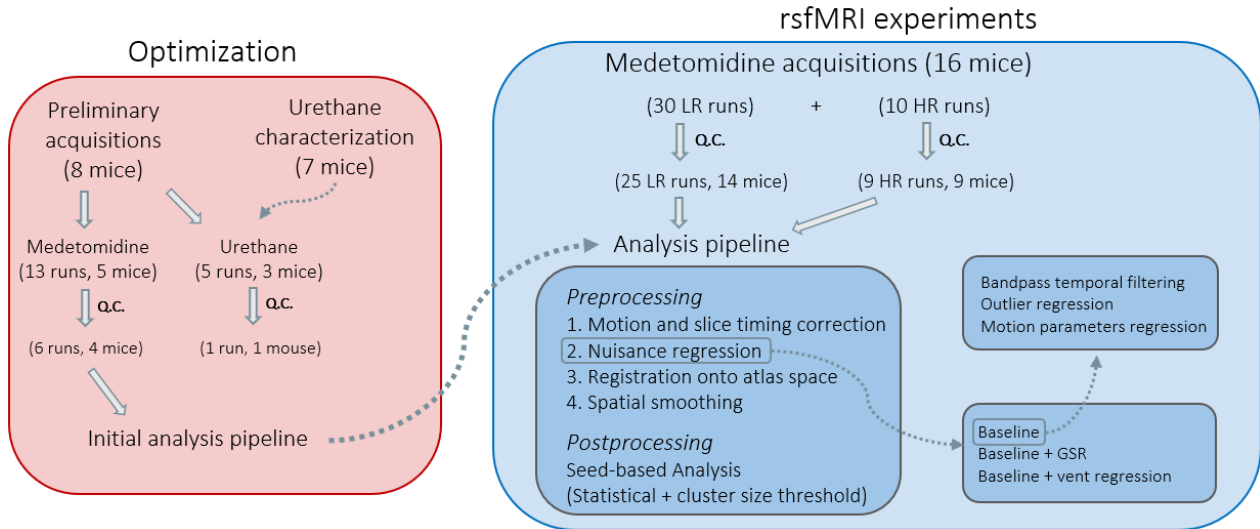


**Figure 2.1:** Schematic representation of the main steps performed in the optimization stage, and in the final resting state acquisition phase. Q.C.: Quality control, LR: Low-resolution, HR: High-resolution, GSR: Global Signal Regression, Vent regression: Ventricular Signal Regression.

All aspects of this study were preapproved by the Champalimaud Centre for the Unknown's Ethics Committee operating under Portuguese and EU Law.

### 2.1. Optimization of Acquisition Parameters

In this optimization stage, an initial MRI acquisition protocol was established, and rsfMRI datasets were acquired in mice under medetomidine. Urethane anesthesia was characterized, as it had not been previously used in the lab, although it has been used in rsfMRI studies by other groups [89][91]. Mice were also scanned under urethane. The following subsections further describe the setups used for these experiments, animal preparation, and details on urethane characterization.

#### 2.1.1. Animal Preparation

A total of 8 female C57BL/6J mice were used in these experiments: 5 weighing  $25.2 \pm 1.4$  g for the preliminary medetomidine acquisitions, between 8 to 9 weeks old, and 3 weighing  $30.4 \pm 0.8$  g for preliminary urethane acquisitions, between 9 to 10 weeks old (weight values presented as mean  $\pm$  standard

deviation). Between experiments, the animals were kept in a temperature-controlled room and held under a 12/12-hour light/dark regimen with standard nutrition and water supply *ad libitum*.

For the medetomidine acquisitions, the animal was placed in a transparent custom-built plastic anesthetizing container, above an electrical heating pad, to prevent body temperature drops. Oxygen concentrations were kept between 27% and 30% with the aid of a portable oxygen monitor (MX300-I, Viamed, United Kingdom). Anesthesia was induced with a mixture of medical air and 5% isoflurane (Vetflurane, Virbac, France), and this concentration was maintained by an isoflurane vaporizer (VetEquip, United States of America). After approximately 2 minutes, once the mouse lost its righting reflex (which is the ability of the mouse to correct and maintain a stable posture and is typically used to ensure loss of consciousness), the concentration of isoflurane was reduced down to 3%. The mouse was then weighed using an analytical scale (Traveler TA1501, Ohaus, Switzerland), and carefully moved to the animal bed, in prone position.

Once on the bed, the animal's head was placed with its upper incisors secured with a bite bar and a nose cone for continuous gas circulation. Ear bars were also used to fixate the head, as a safe and efficient positioning is crucial in animal imaging. A rectal temperature probe and a respiration sensor (Model 1030 Monitoring Gating System, SAI, United States of America) were placed for real-time monitoring of these physiological measurements, to ensure the animal's well-being and immobilization. Respiration rates and temperature were monitored and maintained at physiological levels throughout fMRI scanning.

Throughout the experiments, warm water circulated in a heating pad placed under the animal, through the action of a water pump, and its temperature adjusted to be between 38°C and 45°C, to maintain the mouse body temperature at physiological levels. Ophthalmic drops (Bepanthen Eye Drops, Bepanthen, Germany) were applied to prevent drying and damaging of the cornea.

For the anesthesia infusion, a catheter was inserted subcutaneously in the mouse, and a bolus of previously diluted medetomidine (Dormilan 1 mg/ml, Vetpharma Animal Health S.L., Spain) (1:10 in saline) at 0.4 mg/kg was administered by a syringe pump (GenieTouch, Kent Scientific, United States of America). Isoflurane concentration was gradually reduced, until a concentration of 0.5% was reached after 10 minutes of bolus administration. At this point, a constant infusion of 0.8 mg/kg/h medetomidine began, until the end of the experiment, similarly to a robust protocol previously described [52]. Tape was applied on the animal back, to minimize any possible lower body motion, as well as to ensure the catheter would remain inserted in the animal.

The preparation protocol was similar for urethane, except that after induction, the animal was injected intraperitoneally with a 1.5 g/kg dosage of urethane (Urethane  $\geq 99\%$ , U2500-100G, Sigma-Aldrich, United States), as used in previous studies [89]. The solution had been previously diluted in saline allowing the injection of 0.1 mL of solution per 10 g of animal. The mouse was then placed on the open plastic container, above an electric heating pad, for approximately one hour, to allow for the full effect of the anesthetic. Afterwards, they were positioned in the animal bed, as described, for the duration of the experiment., with no isoflurane mixed in the breathing air.

## 2.1.2. MRI Protocol

All MRI experiments were conducted on a 9.4T horizontal MRI scanner (BioSpec 94/20 USR, Bruker BioSpin, Germany) equipped with a gradient system capable of producing up to 660 mT/m in all directions. An 86 mm resonator volume coil was used for transmittance, and a 4-channel array surface cryocoil was used for reception, allowing SNR enhancing [58]. Imaging was performed using Paravision 6.0.1 (Bruker Biospin MRI GmbH, Ettlingen, Germany).

After mouse sedation, the animal bed was introduced in the scanner bore, placing the receiver coil above the animal head. Scout images, also named Localizers, were acquired in three orthogonal planes to assess the positioning of the brain. Although ear bars allow the head to be fixated in similar and stable positions across experiments, if the brain appeared to be tilted, it would be repositioned to be as aligned as much as possible. After suitable positioning of the animal was confirmed, scan adjustments were performed, and a  $B_0$  map was acquired. This map was used for an appropriate shimming (correction of magnetic field inhomogeneities) in a cylindrical volume covering the brain volume.

Structural images were acquired for anatomical reference. A 3D Multiple Gradient Echo (MGE) sequence was used for the structural images covering the whole brain, with the following parameters: TR = 100 ms, TE = [2.2 : 2.2 : 35.2] ms ([first TE : echo spacing : last TE]), FOV =  $18 \times 9 \times 11.52$  mm<sup>3</sup>, Data matrix =  $180 \times 90 \times 115$ , Number of averages = 1. This resulted in an isotropic spatial resolution of  $0.1 \times 0.1 \times 0.1$  mm<sup>3</sup>, and an acquisition time of 12m16 s. An image covering only a slab in the LC region was also acquired, for potential accurate positioning of a seed, but it was ultimately not used.

After structural acquisitions, a visual stimulation fMRI acquisition was performed, to ensure regular physiological status of the mouse. Standard parameters from previous experiments in the lab were used: GE-EPI sequence, TR = 1000 ms, TE = 12 ms, FOV =  $16 \times 13.9$  mm<sup>2</sup>, Data matrix =  $100 \times 96$ , Bandwidth = 400 kHz, Partial FT (Read/Phase) = 1.00/1.43, Automatic ghost correction and double-sampling. This resulted in a spatial resolution of  $0.145 \times 0.145$  mm<sup>2</sup>, over 8 slices with a thickness of 0.5 mm, oriented axially, i.e. in the transverse plane, as depicted in Figure 2.2. Its acquisition was interleaved, with the order [1 3 5 7 2 4 6 8]. The number of repetitions was 408, and considering that one volume was acquired per second, the acquisition time was 6m48s.

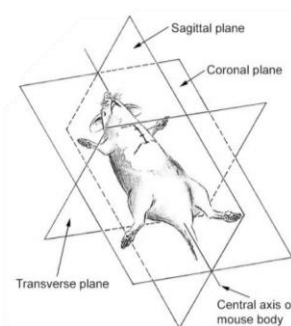


**Figure 2.2:** Three orthogonal planes, as applied conventionally to the mouse body. Adapted from [113].

The visual stimulation setup and protocol are well established in the lab and were only used for confirmation of animal physiological stability, so they will not be described extensively. A fiber-coupled LED with central wavelength located at 470 nm (blue color) (LEDC\_HB01B\_FC, Doric Lenses, Canada) was used for the stimulation. The stimulation paradigm consisted in 5 blocks of 48 seconds rest followed by 24 seconds of visual stimulation, as represented in Figure 2.3. During stimulation periods, the LEDs flashed bilaterally at a frequency of 2 Hz, with a 10 ms pulse width.

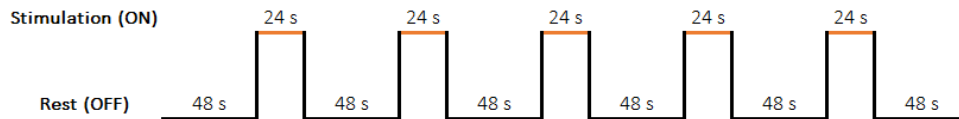


**Figure 2.3:** Paradigm used for visual stimulation.

After the visual stimulation run, there was an interval, 3 to 5 minutes, during which a quick automatized analysis was run on the Paravision software, to confirm normal BOLD activation in expected areas for visual stimulation in mice. A more robust analysis was performed after the scanning period, for more accurate confirmation, and will be described briefly in subsection 2.3. Data Analysis).

After ensuring the animal physiological status, the resting state acquisitions were started. A tentative protocol was established, with the following parameters: two-shot GE-EPI sequence (chosen to reduce image distortion as much as possible), TR = 2000 ms, TE = 10.8 ms, FOV = 15.1 × 12.5 mm<sup>2</sup>, flip angle = 55°, Data matrix = 116 × 96. The spatial resolution was 0.130 × 0.130 mm<sup>2</sup>, over 15 coronally oriented slices. Slice thickness was 0.44 mm, and its acquisition was interleaved. 300 resting state repetitions were acquired, resulting in a total acquisition time of 10 minutes.

Regarding the medetomidine acquisitions, between 2-4 resting state runs were completed for each mouse, per imaging session, with an interval of ~5 minutes between each run. The unbalance of runs between the 5 mice was difficult to avoid, since as soon as the animals would start moving or showing signs of physiological instability, the experiments would be stopped, as this could indicate they would soon wake up. In total, 13 runs were completed: 2 runs were acquired for two mice, 3 runs for other two mice, and 4 runs for the remaining mouse. For the urethane acquisitions, a total of 5 runs were acquired: 2 for two mice and 1 for the remaining mouse, with an interval of ~5 minutes between each run.

After the resting state acquisitions, when possible, a visual stimulation acquisition, similar to the one already described, was performed, aiming to confirm that the mouse physiology remained stable throughout the session.

After the medetomidine experiments, a subcutaneous injection of the previously diluted medetomidine-antagonist atipamezole (Antidorm 5 mg/ml, Vetpharma Animal Health S.L., Spain) (1:10 in saline) was administered, and the mice was placed on the open plastic container, above an electric heating pad, to allow for a quick and full anesthesia recovery (which typically occurred 10 to 15 minutes after the

antagonist injection), after which animals were placed in their original home cages. Regarding urethane experiments, the mice were immediately euthanized after the sessions.

The average time of a session depended greatly on animal stability, and consequent number of fMRI acquisitions, and ranged from 1h30 to 3h. A standard imaging session is represented in Figure 2.4.



**Figure 2.4:** Schematic representation of a normal medetomidine imaging session, with the main steps and their relative, approximate duration. C. inf: Constant Infusion.

In the case of medetomidine acquisitions, material preparation took variable time, since if consecutive mice were being scanned, this step involved merely the cleaning of the setup to be used by the following mouse, while for an initial acquisition, the entire setup had to be prepared. After isoflurane induction, the animal was swiftly prepared, taking between 5 to 10 minutes until the bolus administration, after which isoflurane could be gradually decreased. It was crucial to optimize this step as much as possible, as long periods under high isoflurane concentrations could affect posterior fMRI acquisitions, due to its respiratory and cardiovascular effects. Scanner adjustments and preparatory scans (including structural images acquisition) took approximately 30 minutes, during which isoflurane was dropped to 0.5% and a constant infusion was started. Afterwards, a visual stimulation run was carried out followed by a short break (in a total of roughly 15 minutes), and the resting state acquisitions followed (between 25 minutes to one hour, depending on how many runs could be acquired). By the end, a final visual stimulation run was acquired, and the animal could recover after antagonist injection.

Regarding urethane acquisitions, animal preparation took a longer time, since it took almost one hour for the anesthetic to be fully effective, causing mice to lose their righting reflex and exhibit signs of physiological stability (which is essential for ethical reasons, and for a successful experiment). The bolus, constant infusion and antagonist injection do not apply to these acquisitions, but the remaining steps are identical.

### 2.1.3. Urethane Characterization

Bench tests were conducted to understand the temporal dynamics of urethane effects, as well as to determine a suitable dosage for mouse fMRI.

Urethane solution was prepared and diluted as to allow injection of 0.1 mL of solution per 10 g of animal. A total of 7 female C57BL/6J mice, aged between 9 to 10 weeks, were used in these experiments. Two animals weighing  $26.4 \pm 1.9$  g were tested with a dosage of 1.2 g/kg, but both mice were highly unstable throughout the entire session. Thus, the following five mice, weighing  $27.6 \pm 2.6$  g were tested with a dosage

of 1.5 g/kg, since it appeared to be more stable. These dosages were used based on a previous study using urethane in mice resting state experiments [89].

Anesthesia induction was carried out with isoflurane, identically as described in the previous subsection. Each mouse was then injected intraperitoneally. The animals were then placed in a bed outside the scanner, with isoflurane being discontinued, and with warm water circulating below them, and their respiratory rates and temperatures were monitored, as previously described. These parameters were measured for 3 hours per mouse, and afterwards, the mice were euthanized.

## 2.2. Resting State fMRI Experiments

In this acquisition phase, a final MRI protocol was established, and rsfMRI datasets were acquired in mice under medetomidine. The following subsections further describe the setups used for these experiments, animal preparation and the chosen MRI parameters.

### 2.2.1. Animal Preparation

A total of 16 male C57BL/6J mice aged between 7 to 9 weeks old were used in these experiments, weighing  $26.7 \pm 2.8$  g (weight values presented as mean  $\pm$  standard deviation). The animals were kept in the same conditions as previously described.

All animal preparation was identical to the preliminary medetomidine acquisitions, except the bolus and constant infusion dosages were slightly lower (0.3 mg/kg and 0.6 mg/kg/h, respectively) and after the constant infusion was started, isoflurane was completely discontinued, instead of being kept at 0.5%. These parameters were chosen following previous work [93], reporting bilateral functional networks on free-breathing mice. It should be noted that in this previous study, medetomidine was infused intraperitoneally while, in the present study, a simpler and less invasive subcutaneous approach was adopted.

Respiration rates were constant throughout fMRI scanning, ranging between 110 to 160 breaths per minute for all mice, except two mice who exhibited irregular breathing patterns, and woke up before any resting state run could be acquired. Animal body temperature was meticulously kept between 36°C and 36.5°C during the rsfMRI acquisitions, as this lower dosage of medetomidine and the lack of any isoflurane rendered the animals more prone to waking up, frequently when temperature rose above these values. Moreover, even slight temperature oscillations might cause variations in the BOLD signal baseline [114], thus they should be avoided as much as possible.

### 2.2.2. MRI Protocol

As in the preliminary experiments, structural images were acquired to be used as anatomical reference. The acquisition parameters of the structural image covering most of the brain (roughly from mid-

olfactory bulb to mid-cerebellum) were: RARE sequence, Number of averages = 4, RARE factor = 8, TR = 2200 ms, TE = 9ms,  $TE_{\text{effective}} = 36$  ms, FOV =  $17 \times 11\text{mm}^2$ , Data matrix =  $180 \times 90 \times 115$ . The spatial resolution was  $0.085 \times 0.085\text{mm}^2$  over 25 slices, with a thickness of 0.35 mm. Slices were axially oriented, and its acquisition was interleaved. This resulted in a total acquisition time of 2m20s.

Visual stimulation runs were performed in the beginning, and if possible, at the end of the session, identically as described for the preliminary runs, in subsection 2.1.2. MRI Protocol. After ensuring animal physiological stability, the resting state acquisitions were started. A protocol was established based on [93], with the following parameters: single-shot GE-EPI sequence, TR = 2000 ms, TE = 15 ms, FOV =  $20 \times 20\text{mm}^2$ , flip angle =  $75^\circ$ , Data matrix =  $64 \times 64$ , Bandwidth = 250 kHz, Partial FT (Read/Phase) = 1.00/1.00, Automatic ghost correction. The spatial resolution was  $0.3125 \times 0.3125\text{mm}^2$ , over 17 axially oriented slices, covering brain areas from the end to the olfactory bulb to the beginning of the cerebellum. Slice thickness was 0.5mm, and its acquisition was interleaved. 300 resting state repetitions were acquired, performing a total acquisition time of 10 minutes. Another protocol was established, for a higher resolution acquisition, with identical parameters, except: FOV =  $15 \times 15\text{mm}^2$ , Data matrix =  $90 \times 90$ , resulting in a spatial resolution of  $0.167 \times 0.167\text{mm}^2$ , but with the same acquisition time. These “high-resolution” runs were only performed after the lower-resolution ones, as the main priority was to reproduce literature results. A schematic representation of structural and functional slices coverage can be found in Figure 2.5.

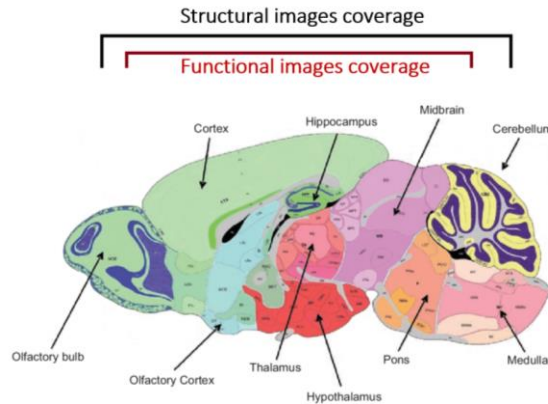


**Figure 2.5:** Mouse brain regions, with average coverage of structural and functional scans. Adapted from [115].

Between 2 to 3 lower resolution resting state runs were completed for each mouse, with an interval of ~5 minutes between each run, except for two mice that woke up before any resting state acquisition could be completed. The imbalance of runs between the 14 mice which were scanned was since some of them woke up mid-experiment or showed signs of physiological instability. In total, 30 lower-resolution runs were completed: 2 runs were acquired for twelve mice, 3 runs for the remaining two mice. For the high-resolution runs, a total of 10 runs were acquired, 1 run per mouse. After the resting state acquisitions, when possible, a visual stimulation run was performed. It was identical as the one previously described, and it was aimed to confirm that the mouse physiology remained stable throughout the session.

## 2.3. Data Analysis

The visual stimulation runs were analyzed using the Statistical Parametric Mapping (SPM) package [116] (SPM12, Wellcome Trust Centre for Neuroimaging, London, UK) for MATLAB, and a Graphical User Interface (GUI) named fmRAT [117], which provided a simple and efficient pipeline for these standard fMRI acquisitions. All these steps are well-established and common practice in this lab and considering that they are only used for quality control, they will be succinctly described: The individual datasets were motion corrected, smoothed with a 3D Gaussian Filter with a FWHM of 0.2 mm, after which the data was fit in a General Linear Model (GLM). The activation maps were thresholded at a p-value  $p < 0.01$  and clusters with less than 15 voxels were removed.

The resting state runs were analyzed using FSL (FMRIB Software Library, v5.0.11, [www.fmrib.ox.ac.uk/fsl](http://www.fmrib.ox.ac.uk/fsl)), AFNI (ver 17.2.05, National Institutes of Health, USA), ANTS [118] (v2.3.1, <http://stnava.github.io/ANTs/>), and Nipype [119] software Nibabel (<https://github.com/nipy/nibabel>) and Nilearn (<http://nilearn.github.io/>), as well as Python 3.0 functions in the SciPy ecosystem [120].

In the following subsections, the main steps in the final preprocessing and analysis pipelines are explained. Some considerations are made regarding the choice of specific parameters, as the construction of the final pipeline was an iterative process.

### 2.3.1. Preprocessing Pipeline

Firstly, structural and functional images were converted to NIFTI format. Regarding functional runs, an initial quality control was performed, by watching videos of each slice across time. This allowed the detection of atypical movements or artifacts which might prevent further analysis.

After raw data quality was ensured, a motion and slice timing correction algorithm was applied [121]. The motion parameters were stored to be later used as regressors. A typical set of motion parameters is plotted in Figure 2.6.

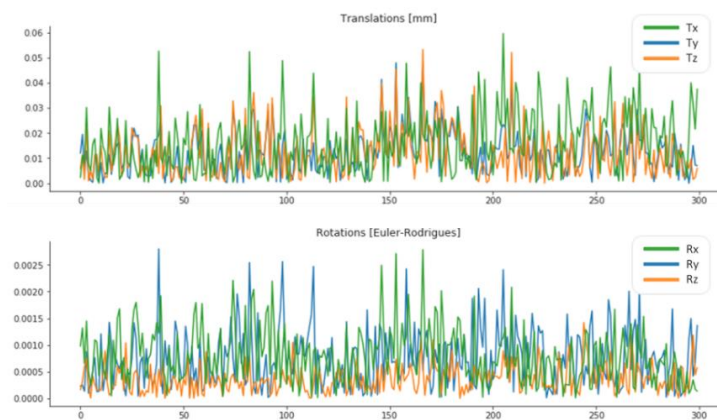


**Figure 2.6:** Example of the 6 motion parameters returned by the motion correction algorithm. (*Top*): Translation (T) parameters, in mm, (on the x, y and z direction), over the 300 repetitions. (*Bottom*): Rotation (R) parameters (Euler angles) on the y-axis, over the 300 repetitions on the x-axis.

Another quality control was performed, to ensure data quality, as some motion correction algorithms might introduce artifacts in the data [93]. Afterwards, a mean image was computed, and a brain mask was automatically created. After individual inspection of the functional brain masks, an outlier detection algorithm was applied on the masked data. If a volume had a displacement larger than 0.3 mm, in relation to the mean image, or a mean intensity image deviating more than 3 standard deviations from the mean, it was detected as an outlier. An example of this outlier detection step can be found in Figure 2.7. Only runs with less than 4 outliers ( $\leq 1\%$ ) were further processed.

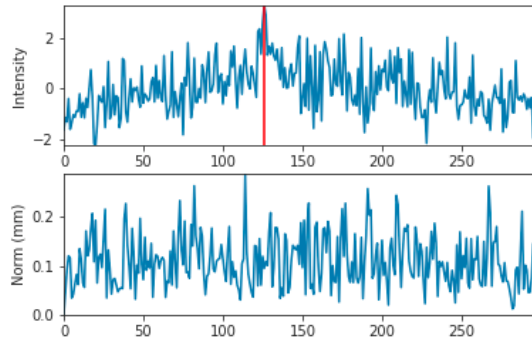


**Figure 2.7:** Outlier detection with a translation threshold of 0.3 mm and intensity threshold of 3 standard deviations from the mean. (*Top*): Intensity of the image over the 300 repetitions, in units of standard deviation from the mean. It can be observed that time point 126 has a mean image intensity exceeding the intensity threshold, thus being detected as an outlier. (*Bottom*): Displacement of each frame from the mean image, over the 300 repetitions.

A nuisance removal step was then performed, and it included motion parameter and outlier regression, where the variance associated with these factors was removed from the data, through a multiple linear nuisance regression. Bandpass filtering was also applied, with cut-off frequencies of 0.01 Hz and 0.2 Hz. The low-pass cut-off was initially chosen as 0.1 Hz, according to previous studies, but since there is no agreement on the exact cutoff frequencies to be used in mice, a more conservative approach was chosen. Steps such as detrending were also considered but ultimately removed, as they did not have a significant effect on the final results, since the remaining preprocessing steps already included spatial and temporal filtering. Thus, redundant and unnecessary manipulations of the data were avoided.

This was considered the “baseline” nuisance removal step, but two variants of this step were also performed. One of the variants also included a time series of the mean signal of the brain as a regressor, performing a Global Signal Regression (GSR). The final variant used a timeseries representing the average signal in the CSF as a regressor. As previously explained, this step is performed since it can be assumed that the CSF doesn’t characterize neuronal activity, therefore representing only spurious signal such as motion, heartbeat and breathing. For this step, ventricular masks were manually delineated for all functional runs, based on an intensity threshold, and an example can be seen in Figure 2.8.

The functional images were registered onto the structural space, using a rigid transformation, followed by a non-linear transformation using SyN (Symmetric Normalization), which was considered one of the best-performing non-linear algorithms, in the context of MR image registration [122]. Global correlation

and mutual information were used as similarity measures for each transformation, respectively. A linear registration was also tested, but it delivered inferior results.

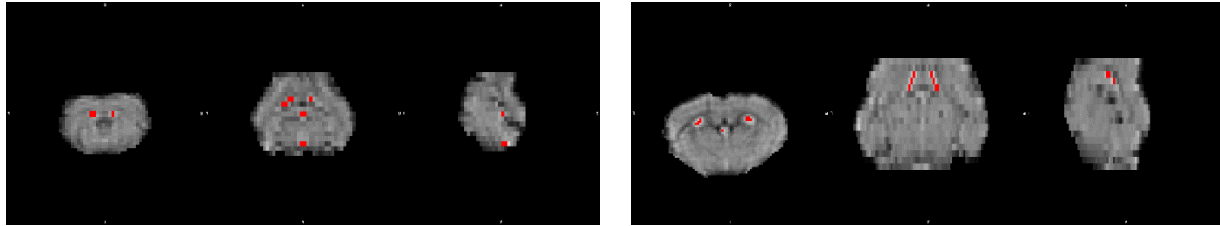


**Figure 2.8:** Ventricular masks used for CSF signal regression. Masks (in red) overlaid on the masked functional data of a (*Left*): lower resolution run and (*Right*): a higher resolution run. In each run, axial, coronal and sagittal views are portrayed (from left to right in the figure).

The structural images were registered onto an atlas – the C57BL/6J model of the Australian Mouse Brain Mapping Consortium (AMBMC) [123][124], using a rigid, followed by an affine, and lastly a non-linear transformation, so that the latter is performed on an already roughly aligned image. Several parameters were tested in this stage, such as transformation type, number of iterations, and restrictions on deformation in each direction, and the final optimized parameters were chosen through visual inspection of the registration results. After registration, the data was assumed to be in the same space, i.e. the same pixel in each individual run is thought to correspond to the same brain region, and a 2-D spatial smoothing using a Gaussian kernel with a FWHM = pixel size (0.3125 mm and 0.167 mm for the lower and high-resolution runs, respectively).

### 2.3.2. Postprocessing

After the preprocessed data was registered to the template space, a seed-based analysis was carried out. The seeds were manually defined from labelled regions on the atlas. They were drawn in the left hemisphere of the following regions: Caudate putamen (CPu), Hippocampus (Hip), Primary motor cortex (M1), Primary (S1) and Secondary (S2) somatosensory cortex, Thalamus (Thal) and Visual Cortices (VC), as most of these regions were chosen in a previous study reporting bilateral networks in mice [93].

The individual connectivity maps were obtained for each run through a correlation analysis, between the averaged BOLD timeseries of the seed region with all voxels in the brain. Correlation analysis was performed using Pearson's correlation, which assumes a predominant linear relationship between rsfMRI signal timeseries, and is considered standard for FC analyses [62].

For the statistical analysis, the individual connectivity maps were concatenated temporally, and a non-parametric (not assuming any specific data distribution) 1-sample t-test was performed, using FSL's *randomise* function [125]. The output of this function is an FWE-Corrected P map, which means it returns P-values with a controlled family-wise error (FWE) rate, corrected for the multiple comparison problem.

The final maps were obtained by averaging individual connectivity maps, and by thresholding connectivity at a value of 0.2 for the lower resolution runs and 0.15 for high-resolution runs, FEW corrected P-value  $p < 0.01$  and a minimum cluster size of 10 voxels.

Coincidence maps were also computed with the same thresholds. These measured the percentage of times across runs that each voxel in the brain had a correlation equal or higher than the used threshold.

To evaluate the different preprocessing pipelines (baseline, ventricular signal regression, and GSR), an interhemispheric connectivity analysis was conducted, where the correlation between larger ROIs, anatomically defined in the atlas space in both hemispheres of the brain, was computed. The ROIs were drawn in the same regions that were previously mentioned. The correlation values were then tested with a two-sample two-tailed t-test with unequal variance to check for pairwise significant differences, as well as a Kruskal-Wallis test, to test for differences of the data distribution (the non-parametric equivalent of ANOVA).

For the preliminary acquisitions, statistical thresholding and posterior small cluster removal were not performed, but an additional ICA was carried out, as a purely exploratory, more data-driven approach. FSL's MELODIC tool was used, with default parameters.



## 3. Results

In this section, relevant and representative results are shown, regarding both the optimization stage and the rsfMRI acquisitions.

### 3.1. Optimization of Acquisition Parameters

In this subsection, a brief overview of some results of the optimization phase are shown, including raw data from both functional and structural images, illustrative results from the analyses, and measurements from the urethane characterization.

#### 3.1.1. Preliminary Resting State fMRI Acquisitions

In Figure 3.1, it is possible to observe an example of a typical raw structural image from the preliminary acquisitions, which possess a high resolution.

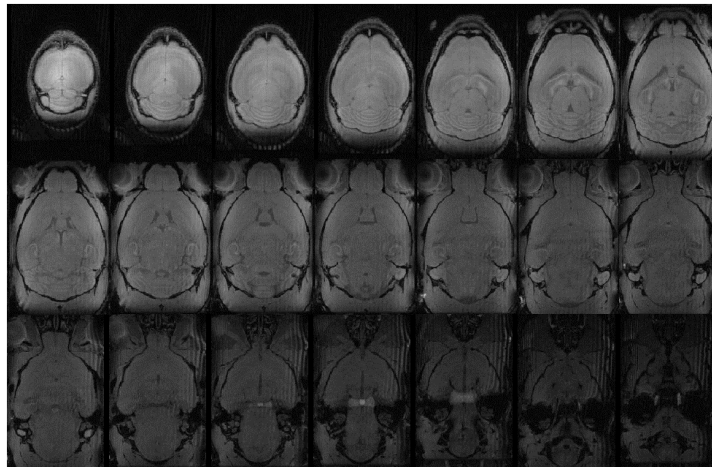


**Figure 3.1:** Raw structural images from one representative mouse. Slices are presented from the dorsal (upper) to the ventral (lower) part of the brain (from left to right and top to bottom in the figure).

While the structural image has high SNR, few distortions, and a very good resolution, functional images have a higher temporal resolution, which indirectly limits these parameters. There are distortions and signal losses typical in EPI sequence, but these were attenuated using a two-shot EPI. Raw functional images can be seen in Figure 3.2, with highlights on some of the most evident artifacts. Slightly higher signal can be observed on dorsal slices compared to ventral slices, since the cryocoil used for reception is a surface coil, closer to the dorsal part of the brain. tSNR, which can be used as a data quality index [79][56], was computed as the ratio between temporal mean signal of the brain area, and its standard deviation. The runs exhibited an average tSNR of  $29.7 \pm 1.2$  (mean  $\pm$  standard deviation of tSNR across animals).

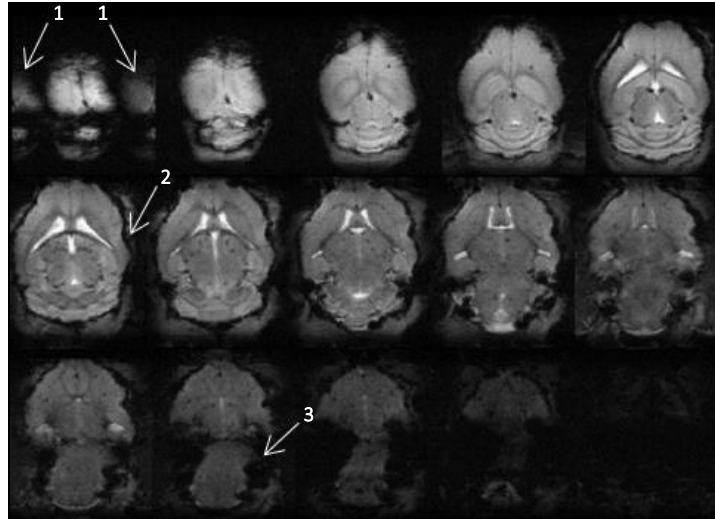


**Figure 3.2:** Raw functional images from one representative mouse. Slices are presented from the dorsal (upper) to the ventral (lower) part of the brain (from left to right and top to bottom in the figure). White arrows highlight some of the most evident (1) ghost artifacts, (2) signal losses and (3) distortions.

Nyquist ghosts were recurring artifacts throughout the functional acquisitions, rendering many runs unusable. Following quality control steps, including the discarding of datasets with too many outliers, 6 medetomidine runs were considered adequate, and were further analyzed. For the urethane runs, there was only 1 run which was not discarded, and, considering the unsatisfactory results of the medetomidine runs, it was not further processed. Due to the preliminary modest results, urethane acquisitions were ceased, as urethane is a terminal anesthesia. Posterior acquisitions were performed only under medetomidine.

A representative connectivity map, with a seed on the primary motor cortex (M1), can be seen in Figure 3.3. The other preprocessing pipelines (with GSR, and ventricular signal regression) delivered identical results. It is evident that this map is rather noisy, showing apparently random connectivity patterns on most slices, with low correlation values. Slight bilateral signal can be seen in the second slice, but it is not very clean or well defined.

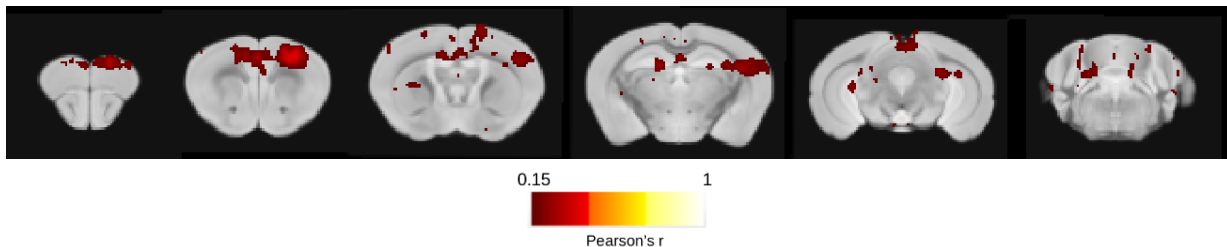


**Figure 3.3:** Connectivity map with a seed on M1, using the baseline preprocessing pipeline. The 6 individual connectivity maps were averaged, and thresholded at a connectivity of 0.15. Results are overlaid on the used mouse brain atlas, on an axial view. Slices are shown from rostral (forward) to caudal (backwards) direction, from left to right, in the figure.

An exploratory ICA was carried out, in an attempt of identifying possible networks using a different analysis method. Three examples of obtained spatial maps can be found in Figure 3.4.

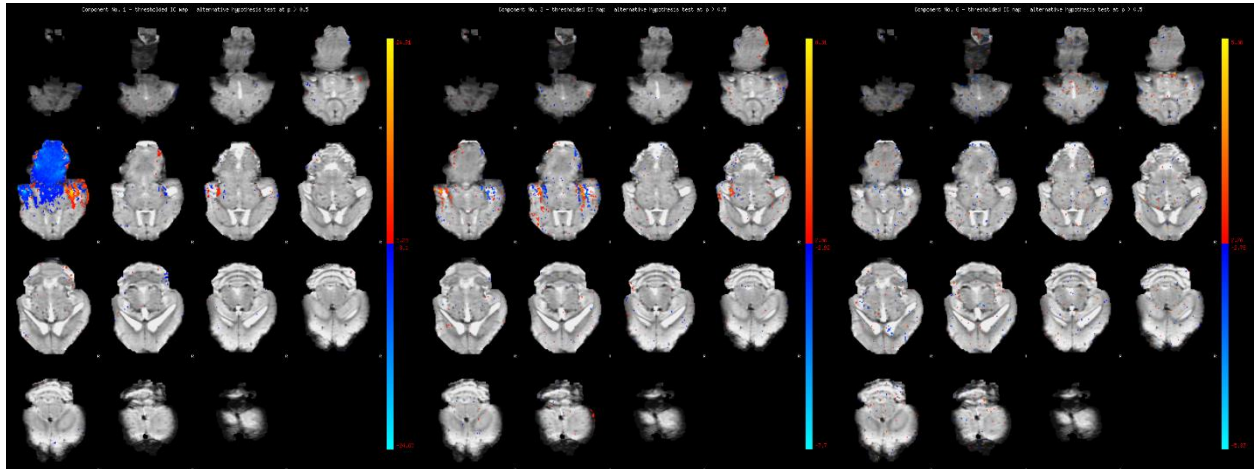


**Figure 3.4:** Three representative spatial maps obtained from an ICA. (*Left*): Spatial map from independent component (IC) 1, (*Middle*): Spatial map from IC 3, and (*Right*): Spatial map from IC 6.

The spatial maps mostly consist on either very large regions restricted on a single slice, striped patterns, or numerous small and sparse clusters. An example of the power spectrum of an IC's typical time course can be seen in Figure 3.5, and it is possible to observe it does not appear to have a predominant low frequency distribution, and its strongest peak is above 0.1 Hz.

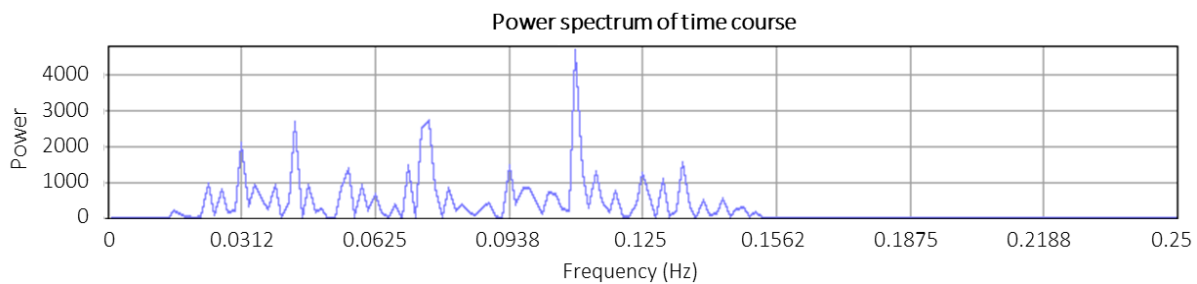


**Figure 3.5:** Representative power spectrum of one of the IC time courses.

### 3.1.2. Urethane Characterization

As described in subsection 2.1.3. (Urethane Characterization), two different dosages were tested. For the 1.2 g/kg dosage, both mice were highly unstable throughout the entire session, ultimately moving and waking up. Therefore, the dosage was increased to 1.5 g/kg.

Regarding the 5 mice tested with the latter concentration, it took between 40 to 80 minutes for the mice to be stable and cease to spontaneously wake up and/or move. In Table 3.1, the measurements acquired in these 5 mice are shown. Temperature variations are small, but it should be noted that some MRI sequences, namely EPIs, might increase the rodent's body temperature, and this is not accounted for in the bench tests. Additionally, respiration rates are largely higher than in medetomidine experiments, which range from 110 to 160 bpm.

**Table 3.1:** Features and measurements of the 5 mice under a dosage of 1.5g/kg of urethane.

| Mouse | Age (weeks) | Weight (g) | Respiratory rate (bpm) | Temperature (°C) |
|-------|-------------|------------|------------------------|------------------|
| 1     | 10          | 30.1       | 182.84 ± 19.55         | 36.72 ± 0.15     |
| 2     | 9           | 29.7       | 176.14 ± 23.46         | 36.54 ± 0.10     |
| 3     | 9           | 24.2       | 206.12 ± 26.66         | 36.45 ± 0.24     |
| 4     | 10          | 29.5       | 221.26 ± 24.72         | 36.56 ± 0.26     |
| 5     | 9           | 24.7       | 216.35 ± 11.59         | 36.46 ± 0.09     |

## 3.2. Resting state fMRI Experiments

In this subsection, the main outcomes of the resting state acquisitions are shown, including some results regarding quality control, as well as connectivity and coincidence maps.

### 3.2.1. Quality Control

An example of raw structural images can be seen in Figure 3.6. As anticipated, they present a very high resolution and negligible distortions.

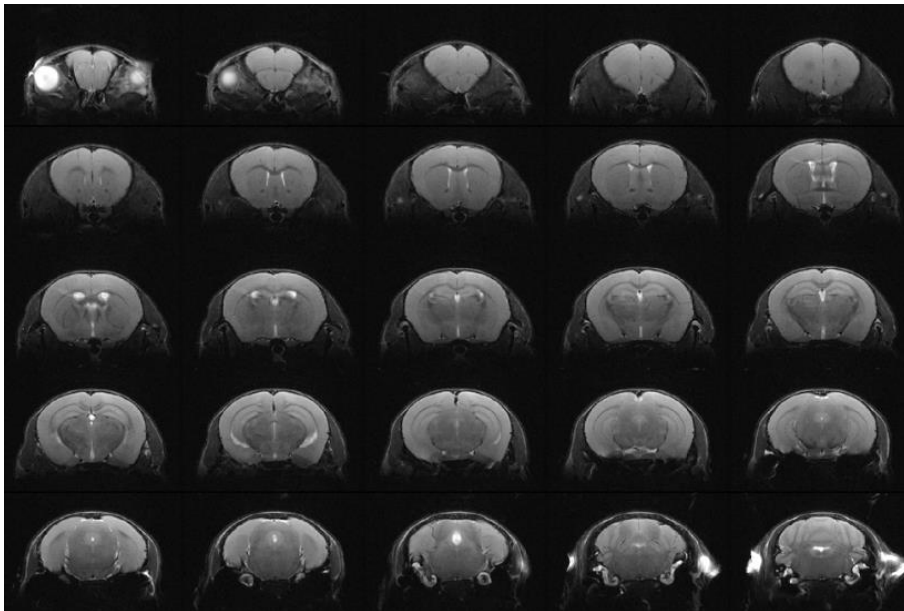


**Figure 3.6:** Raw structural images from one representative mouse. Slices are presented from the rostral to the caudal part of the brain (from left to right and top to bottom in the figure).

Functional images were expected to have a much lower resolution and the typical EPI distortions. Still, they were reliable and robust across mice. tSNR was also computed, and the lower resolution runs exhibited an average tSNR of  $92.7 \pm 10.4$  (mean  $\pm$  standard deviation of tSNR across animals). For the high-resolution runs, this value was equal to  $53.8 \pm 6.3$ , a foreseeable decrease due to the smaller pixel dimensions (0.3125 mm to 0.167 mm). An example of raw functional images can be seen in Figure 3.7 and Figure 3.8, for lower and high-resolution runs, respectively.

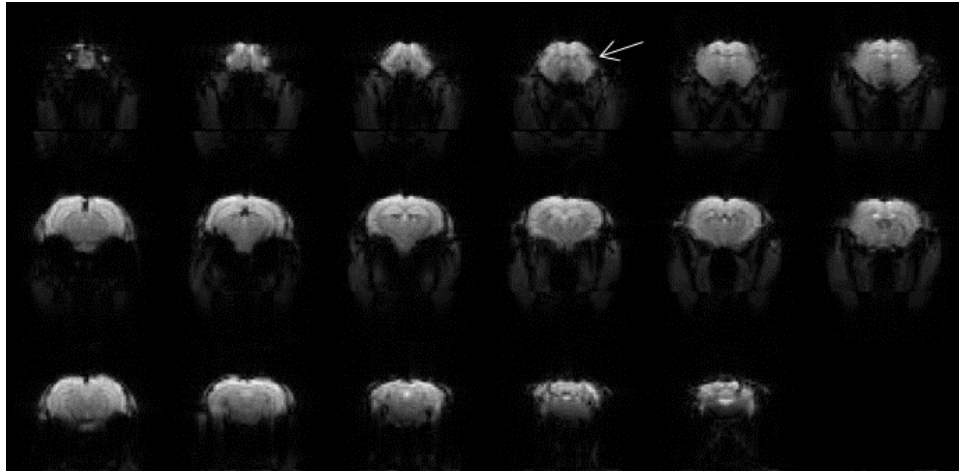


**Figure 3.7:** Raw functional images from one representative mouse (lower resolution run). Slices are presented from the rostral to the caudal part of the brain (from left to right and top to bottom in the figure). The white arrow highlights an area with signal loss.

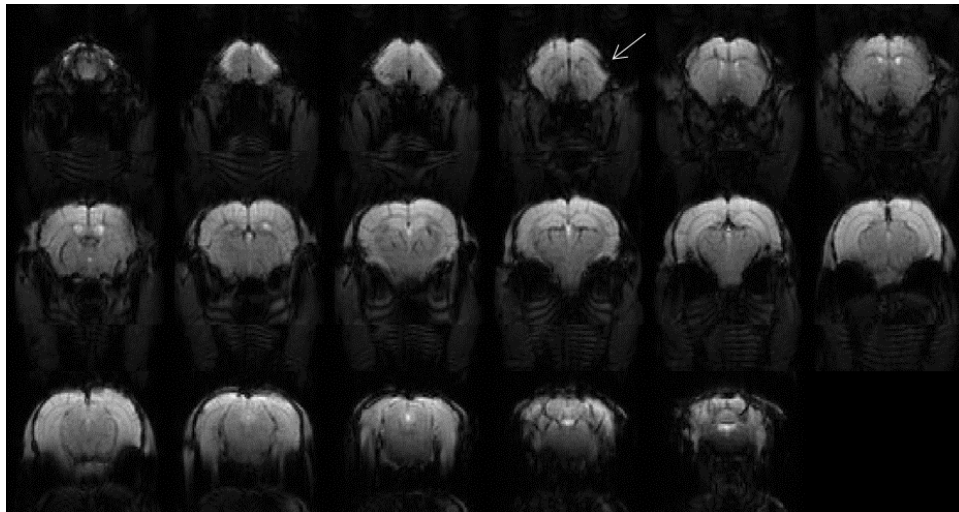


**Figure 3.8:** Raw functional images from one representative mouse (high-resolution run). Slices are presented from the rostral to the caudal part of the brain (from left to right and top to bottom in the figure). The white arrow highlights an area with signal loss.

It can be noticed that these images show much less distortions than the preliminary ones. In both cases, areas with signal losses can be identified, but these are not very severe, and the distortions are minimal. Notably, no ghost artifacts were detected.

Regarding the tSNR, it should be noted that, since the cryocoil used for signal reception is a surface coil, the measured signal is higher in cortical areas, closer to the coil, than in striatal regions. Thus, considerable tSNR variation within the same animal must be considered.

Visual stimulation runs were performed to ensure animal physiological stability, and a map from a representative mouse can be seen in Figure 3.9.

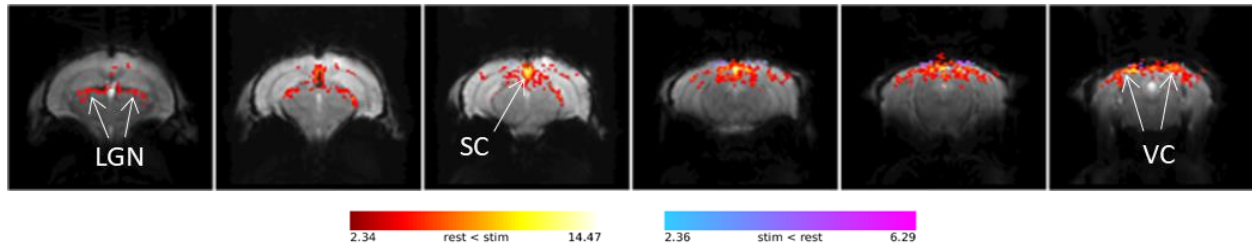


**Figure 3.9:** Brain map of significant ( $p < 0.01$ , minimum cluster size = 15) BOLD activation to binocular visual stimulation with 2 Hz flashing frequency and 10 ms of pulse width. Lateral geniculate nucleus (LGN), superior colliculus (SC) and visual cortices (VC) are identified. Slices are presented from the rostral to the caudal part of the brain (from left to right in the figure).

Areas including the lateral geniculate nucleus (LGN), superior colliculus (SC) and visual cortices (VC), are well-established as belonging to the mouse visual pathway [126] and known to have strong BOLD responses upon visual stimulation [127], and it can be observed that these areas show clear BOLD activation upon stimulation. For all used resting state runs, a comparable activation map was obtained from the stimulation performed before and/or after the resting state acquisition, which is indicative of regular physiological status of the mice.

In order to verify that the preprocessing pipeline of the resting state data had an appropriate performance, a brief ROI analysis was conducted. This analysis had the aim to confirm that after preprocessing, there would be a high temporal correlation between the same regions across hemispheres, compared to a low correlation between these regions and another region in the brain. Time series from different ROIs were compared before and after preprocessing, using the baseline pipeline. The other two preprocessing variants were also tested, but the results were identical. Two pairs of “left” and “right” ROIs, and a single “other” ROI, were created for each mouse. Correlation values within each “left-right” pair were computed, as well as between “left” and “other” ROIs. Illustrative results from two mice are shown in the following figures. The location of the ROIs used in the analysis can be seen in Figure 3.10. Resulting timeseries are plotted in Figure 3.11, Figure 3.12, Figure 3.13, and Figure 3.14, for the first mouse, first and second “left-right” ROI pair, and for second mouse, first and second “left-right” ROI pair, respectively.

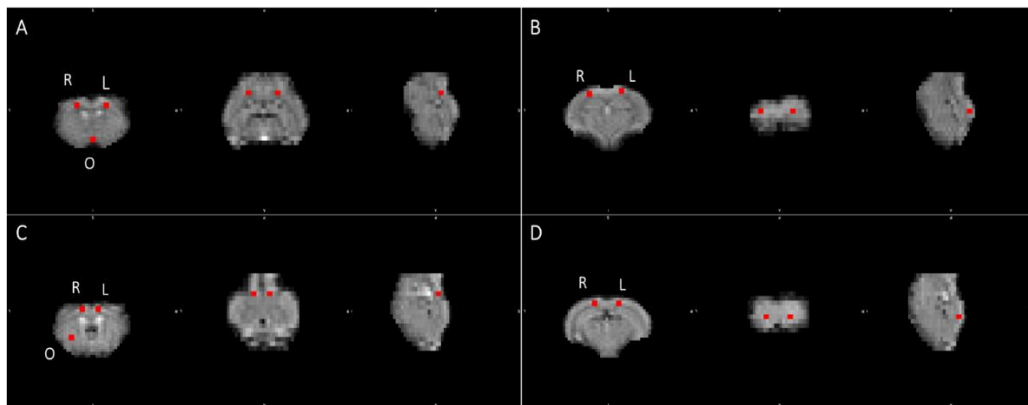


**Figure 3.10:** Location of the ROIs (in red) used in the analysis. L = Left ROI, R = Right ROI, O = Other ROI. Axial, coronal and sagittal views are portrayed (from left to right in each figure). (A): Mouse 1, with identification of the first pair of “left and right” ROIs, and “other” ROI. (B): Mouse 1, with identification of the second pair of “left and right” ROIs. (C): Mouse 2, with identification of the first pair of “left and right”, and “other” ROI. (D): Mouse 2, with identification of the second pair of “left and right” ROIs.

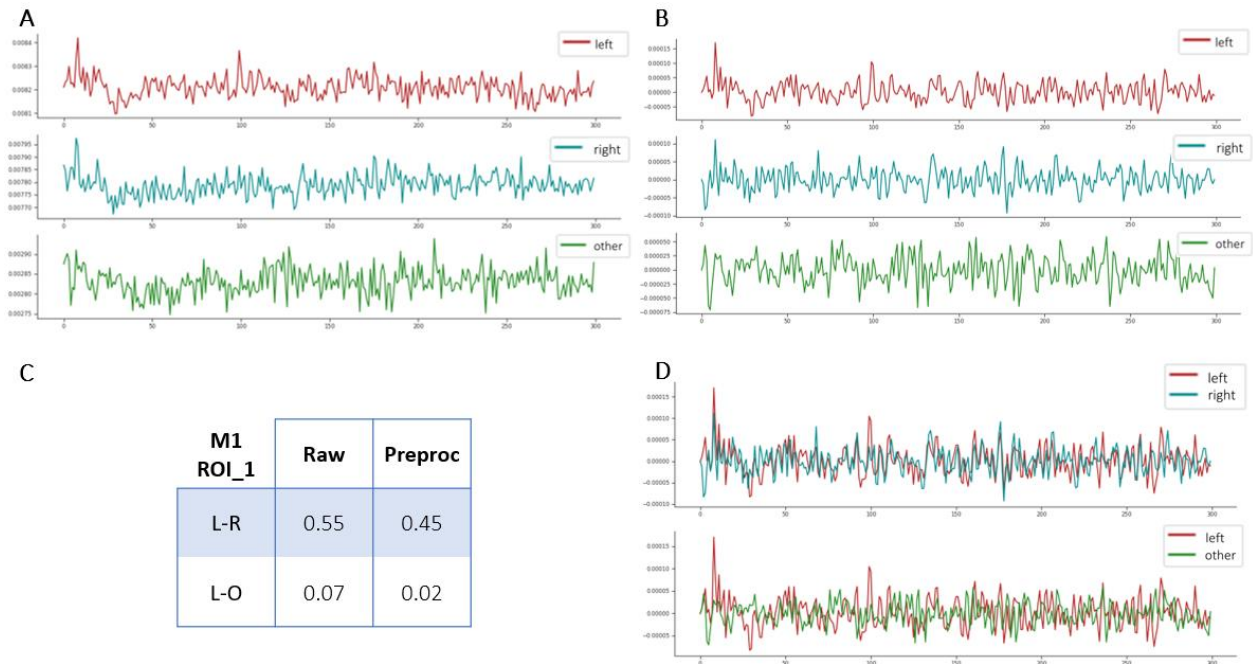


**Figure 3.11:** Timeseries and correlation values, for the first mouse, and first pair of “left right” ROIs. (A): Timeseries of the left, right and other ROI, in the raw data. (B): Timeseries of the left, right and other ROI, in the preprocessed data. (C): Correlation coefficients (in Pearson’s  $r$ ) between the timeseries of the left and right ROI pair (L-R), and between the left and other timeseries. (D): Overlaid timeseries of the ROIs being compared.

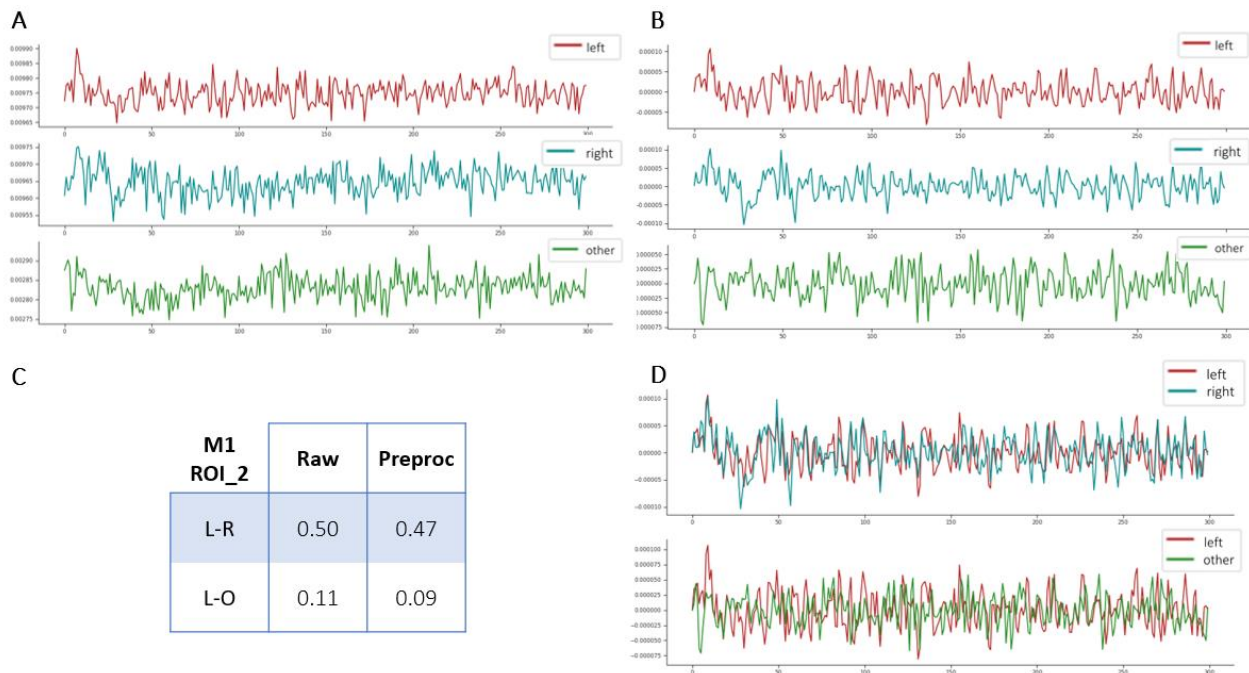


**Figure 3.12:** Timeseries and correlation values, for the first mouse, and second pair of “left right” ROIs. (A): Timeseries of the left, right and other ROI, in the raw data. (B): Timeseries of the left, right and other ROI, in the preprocessed data. (C): Correlation coefficients (in Pearson’s  $r$ ) between the timeseries of the left and right ROI pair (L-R), and between the left and other timeseries. (D): Overlaid timeseries of the ROIs being compared.

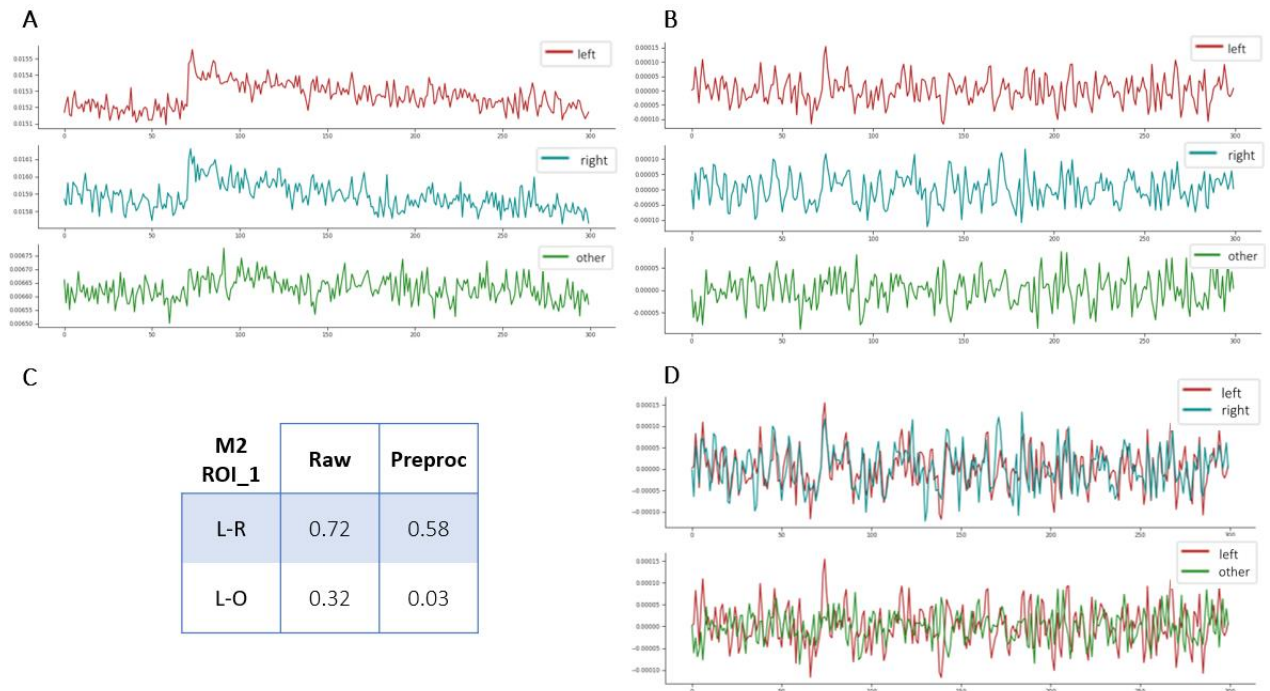


**Figure 3.13:** Timeseries and correlation values, for the second mouse, and first pair of “left right” ROIs. (A): Timeseries of the left, right and other ROI, in the raw data. (B): Timeseries of the left, right and other ROI, in the preprocessed data. (C): Correlation coefficients (in Pearson’s  $r$ ) between the timeseries of the left and right ROI pair (L-R), and between the left and other timeseries. (D): Overlaid timeseries of the ROIs being compared.

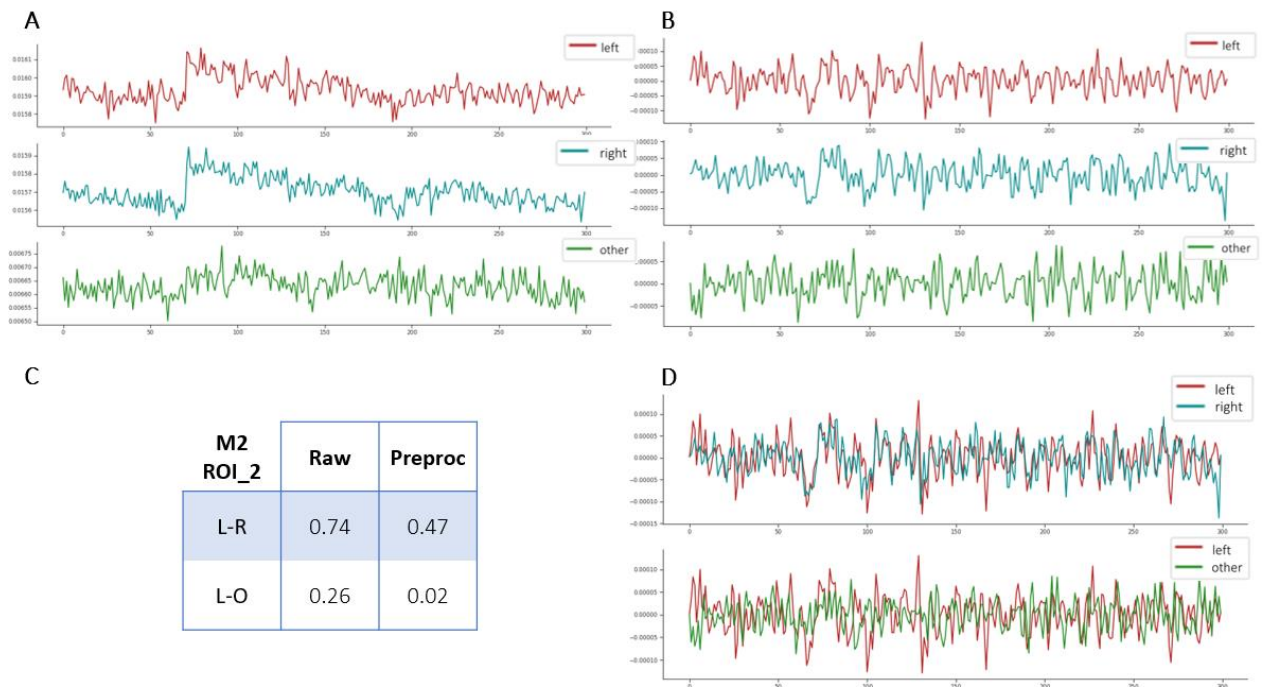


**Figure 3.14:** Timeseries and correlation values, for the second mouse, and second pair of “left right” ROIs. (A): Timeseries of the left, right and other ROI, in the raw data. (B): Timeseries of the left, right and other ROI, in the preprocessed data. (C): Correlation coefficients (in Pearson’s  $r$ ) between the timeseries of the left and right ROI pair (L-R), and between the left and other timeseries. (D): Overlaid timeseries of the ROIs being compared.

After the analysis of these four figures, some common features can be noticed. Firstly, correlation between “left” and “right” ROIs is higher than correlation between “left” and “other” ROIs, on both raw and preprocessed timeseries. This was predictable, as the “left” and “right” ROIs were placed in locations where bilateral signal was likely, and the “other” ROI was delineated at a greater distance and in unrelated areas. Still, in Figure 3.13 and Figure 3.14, it is observed that this unrelated area had a correlation higher than the thresholds used in the final maps (0.2 and 0.15, in lower and high-resolution runs, respectively). It can also be noticed that after preprocessing, all correlation values are reduced. Although a decrease in the “left-right” correlation could seem like a negative result, it is actually predictable, assuming the pipeline’s good performance. By removing artifacts, regressing out motion parameters, and filtering noise-related frequencies, spurious correlation will be removed. For example, in Figure 3.14, there is an abrupt signal rise on the left and right ROIs, on the first third of both timeseries, resulting in a very high correlation value of 0.74 between them. After preprocessing, these sudden changes are removed or attenuated, resulting in a more realistic correlation (in this case, 0.47, which is still a rather strong association). It can be noted that the “other” regions which had relatively high correlation values (above the threshold used for identification of functional networks) show rather minimal association after the preprocessing. From 0.32 and 0.26, there is a respective decrease to 0.03 and 0.02. These findings were recurring across mice and different ROIs, and they are consistent with a suitable preprocessing pipeline performance.

After examining raw data and the preprocessing pipeline, registrations were individually inspected. In Figure 3.15, examples of functional images from the low- and high-resolution datasets, in the structural space are shown, for an illustrative mouse. Raw slices for both datasets were presented in Figure 3.7 and Figure 3.8, respectively.

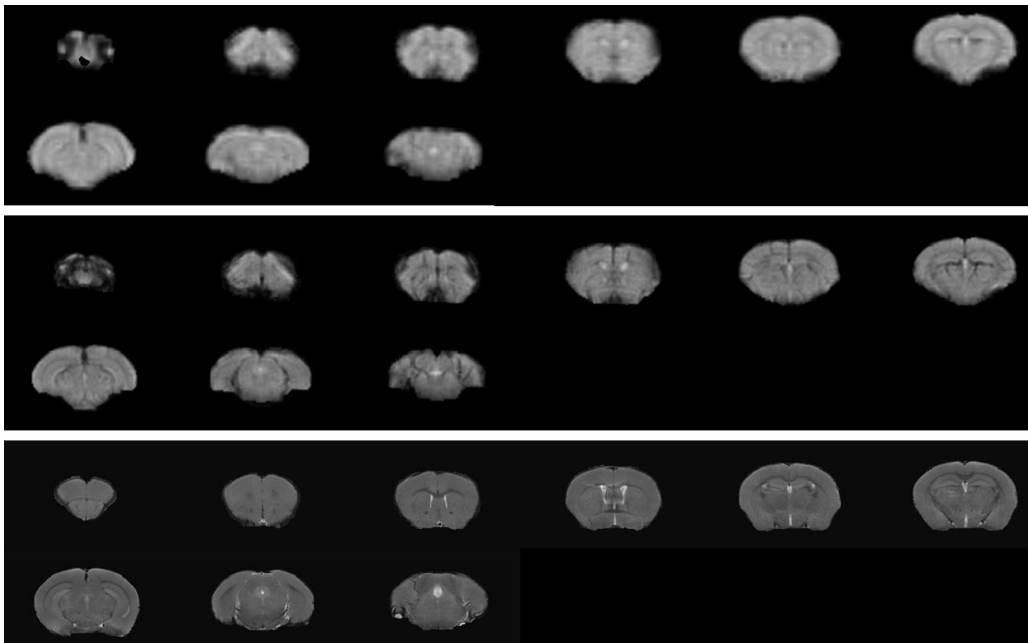


**Figure 3.15:** Registration from functional to structural space. (*Top*): Functional images of the low-resolution dataset, aligned in the structural space, (*Middle*): functional images of the high-resolution dataset, aligned in the structural space and (*Bottom*): structural images used for the registration.

It can be observed that the alignment between functional and structural images is precise. As would be predicted, higher resolution runs result in a more accurate registration, but considering the significantly higher voxel size of the lower resolution runs, the results can be considered quite good overall. Figure 3.16 depicts the registration from structural to atlas space.

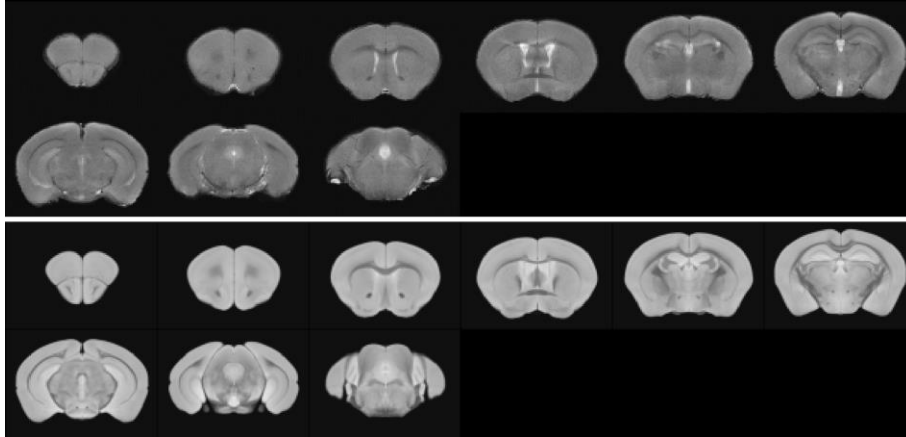


**Figure 3.16:** Registration from structural to atlas space. (*Top*): Structural images on the structural space, and (*Bottom*): Atlas images used as reference.

Upon visual inspection, structural registration was considered to perform extremely well, with near perfect positioning of the outer edges, but also regarding the finer structures in more subcortical areas.

### 3.2.2. Resting State Analysis

After ensuring data quality and verifying that the preprocessing pipeline delivered plausible results, further analysis could be performed, and their results are shown in the following subsections. For an easier visualization, Figure 3.17 illustrates the positions of relevant brain areas that will be mentioned and discussed. The previously mentioned seeds were delineated inside these regions, avoiding their edges and transitions between areas, as to minimize partial volume effects (PVE).

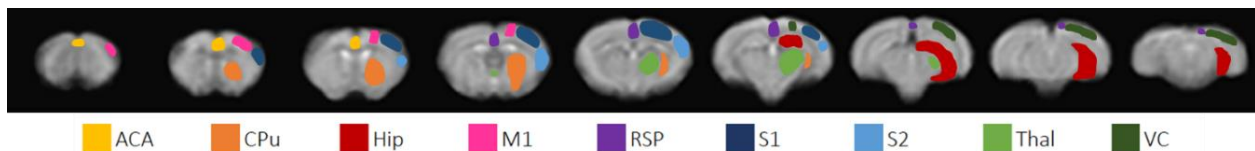


**Figure 3.17:** Anatomical location of pertinent brain areas. For clarity, only the left side of these regions is presented, overlaid on the averaged functional images, in atlas space. ACA = Anterior Cingulate Area, CPu = Caudate Putamen, Hip = Hippocampus, M1 = Primary Motor Cortex, RSP = Retrosplenial Area, S1 = Primary Somatosensory Cortex, S2 = Secondary Somatosensory Cortex, Thal = Thalamus, VC = Visual Cortices.

#### 3.2.2.A. Low Resolution

As mentioned in subsection 2.3.2. Postprocessing), the output of a seed-based analysis is a connectivity map, which is obtained for each single resting state run. An example of a typical individual connectivity map can be found in Figure 3.18.

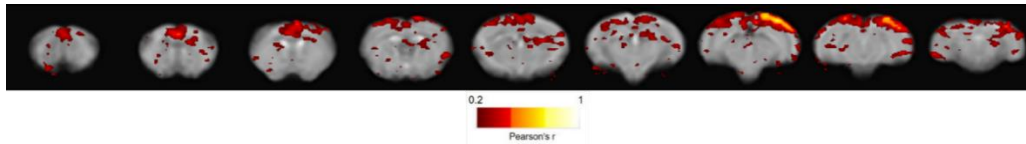


**Figure 3.18:** Connectivity map from an individual low-resolution run with the baseline preprocessing pipeline, with a seed in the left visual cortex (VC). Pearson correlation values thresholded at a minimum of 0.2, with a corresponding maximum p-value of 0.001. Slices are presented from the rostral to the caudal part of the brain.

It is possible to see that the area surrounding the VC region has the highest correlation values. Bilateral signal can also be observed, in the contralateral region of the seed. Multiple smaller and scattered regions appear as correlated with the seed region. Through these individual maps, a non-parametric 1-sample t-test was performed, resulting in a statistical map. An example of these statistical maps is depicted in Figure 3.19, which shows the areas which resulted in a FWE-corrected p-value  $< 0.01$ . These statistical maps were subsequently used to threshold the final connectivity maps, averaged across animals.

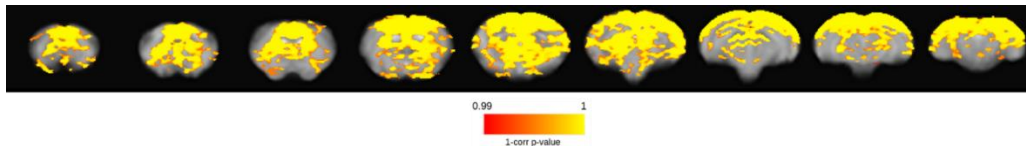


**Figure 3.19:** Statistical map from 25 individual connectivity maps, from the lower resolution dataset, with a seed in the VC, thresholded at  $p < 0.01$ . Values are presented as 1-corr p-value, i.e. 0.99 corresponds to a p-value of 0.01, corrected for FWE. Slices are presented from the caudal rostral to the caudal part of the brain.

After removing small clusters (less than 10 voxels), the final connectivity maps depicting functional networks are obtained. For the baseline, GSR and ventricular signal regression preprocessing pipelines, these maps are presented in Figure 3.20, Figure 3.21 and Figure 3.22, respectively.

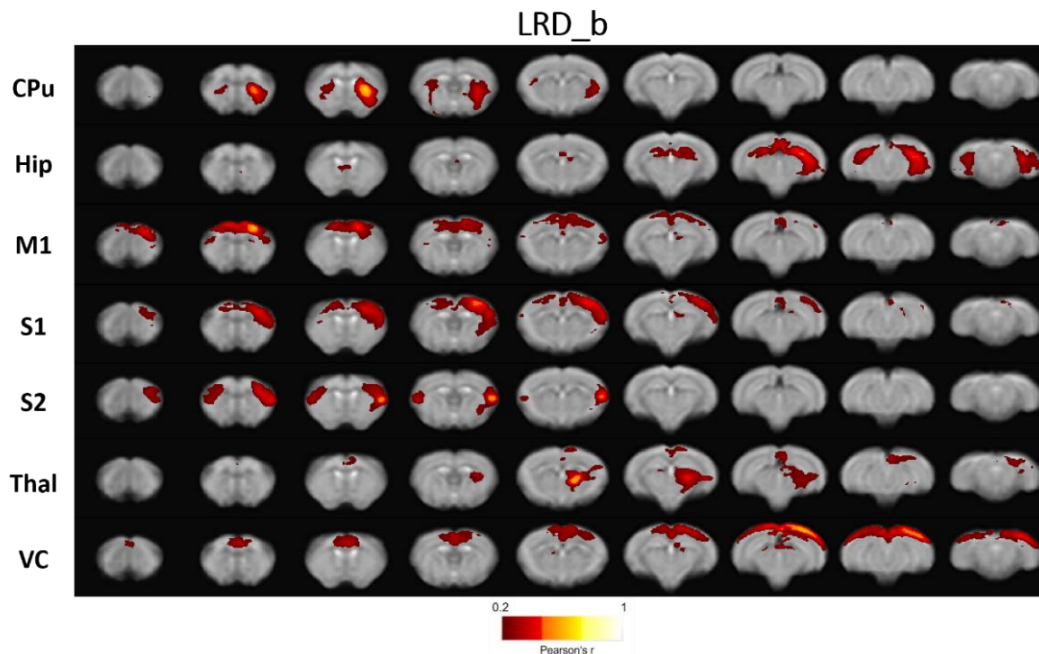


**Figure 3.20:** Connectivity maps, from 25 runs of the low-resolution dataset (LRD), with the baseline pipeline. Seven seeds were positioned on the left side of Caudate Putamen (CPU), Hippocampus (Hip), Primary Motor Cortex (M1), Primary (S1) and Secondary (S2) Somatosensory cortices, Thalamus (Thal) and Visual Cortices (VC). Thresholds at 0.2 Pearson correlation,  $p < 0.01$  and minimum cluster size of 10 voxels. Slices presented from rostral to caudal part of the brain (from left to right in the figure), and data is overlaid on top of the averaged functional runs, in atlas space.

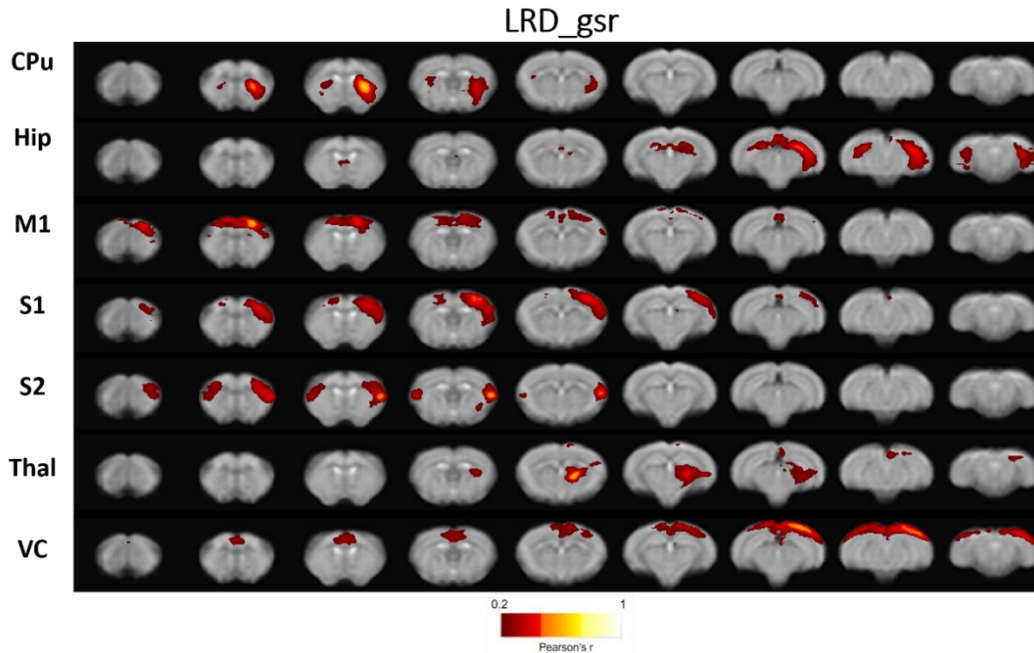


**Figure 3.21:** Connectivity maps, averaged from 25 runs from the low-resolution dataset, preprocessed with the pipeline performing GSR. Seven seeds were positioned on the left side of Caudate Putamen (CPu), Hippocampus (Hip), Primary Motor Cortex (M1), Primary (S1) and Secondary (S2) Somatosensory cortices, Thalamus (Thal) and Visual Cortices (VC). Thresholds at 0.2 Pearson correlation,  $p < 0.01$  and minimum cluster size of 10 voxels. Data is overlaid on top of the averaged functional runs, in atlas space.

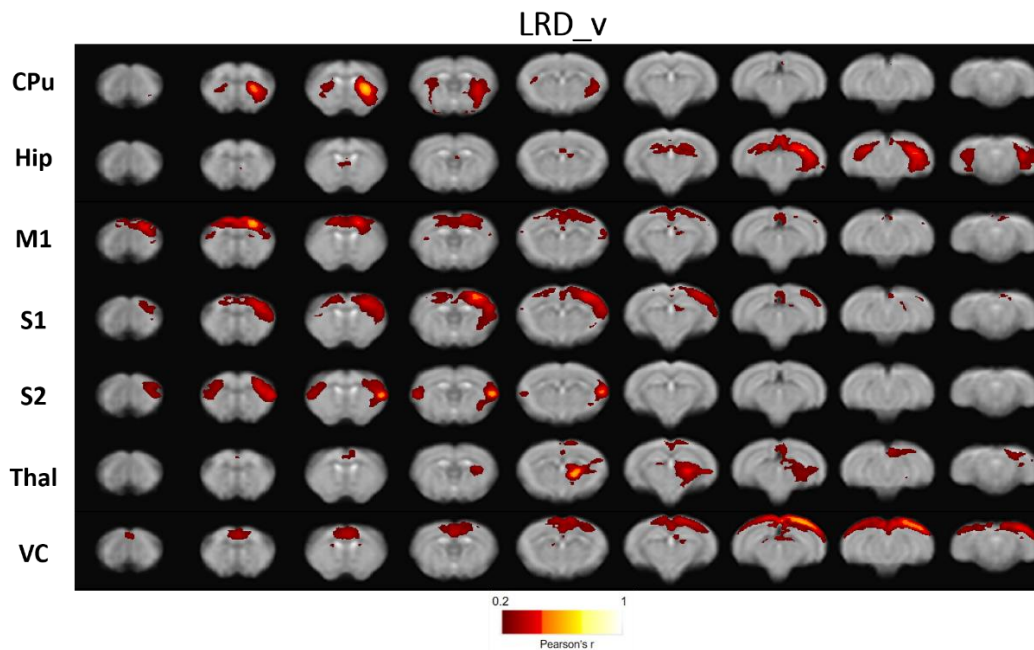


**Figure 3.22:** Connectivity maps, averaged from 25 runs from the low-resolution dataset, preprocessed with the pipeline performing ventricular signal regression. Seven seeds were positioned on the left side of Caudate Putamen (CPu), Hippocampus (Hip), Primary Motor Cortex (M1), Primary (S1) and Secondary (S2) Somatosensory cortices, Thalamus (Thal) and Visual Cortices (VC). Thresholds at 0.2 Pearson correlation,  $p < 0.01$  and minimum cluster size of 10 voxels. Data is overlaid on top of the averaged functional runs, in atlas space.

Regarding the baseline pipeline, the averaged maps have better defined connectivity regions. Scattered regions previously appearing as correlated with the seeds are mostly not present, contrarily to what occurred in individual maps.

Most networks have a bilateral signal, although the clusters in the seed's ipsilateral side appear to be slightly larger in some cases. For example, the S1 network has larger clusters on the left side, although it also shows significant connectivity on the right side.

Despite the mostly bilateral maps, it can be noticed that the Thal seed resulted in a more unilateral map. There is a clear lack of clusters in the right side of the brain for this map, and there is a striped pattern that correlates with non-grey matter areas. It can also be noticed that the VC network includes part of the anterior cingulate area (ACA), retrosplenial area (RSP), and that there are some overlapping clusters on M1, S1 and S2 networks.

Through visual inspection, it can be noticed that the three pipelines result in similar maps. Cluster size marginally varies, with a slight decrease in the number of voxels in the largest clusters in the GSR maps, i.e. the GSR pipeline generally results in smaller clusters compared to other pipelines. For example, in M1, S1 and S2 networks, the correlated area is slightly reduced, with an approximate 20% decrease of the number of voxels in the largest cluster. Most of the features identified in the maps with baseline processing are recurring across the pipelines. Additionally, some of the smaller clusters in the baseline and ventricular regression pipelines disappear, when using the GSR pipeline.

To further ensure that the final maps were not product of highly variable data, coincidence maps were computed. These present the percentage of times across runs that each voxel had a correlation equal or higher than the used threshold. Figure 3.23 shows representative coincidence maps for three seeds.

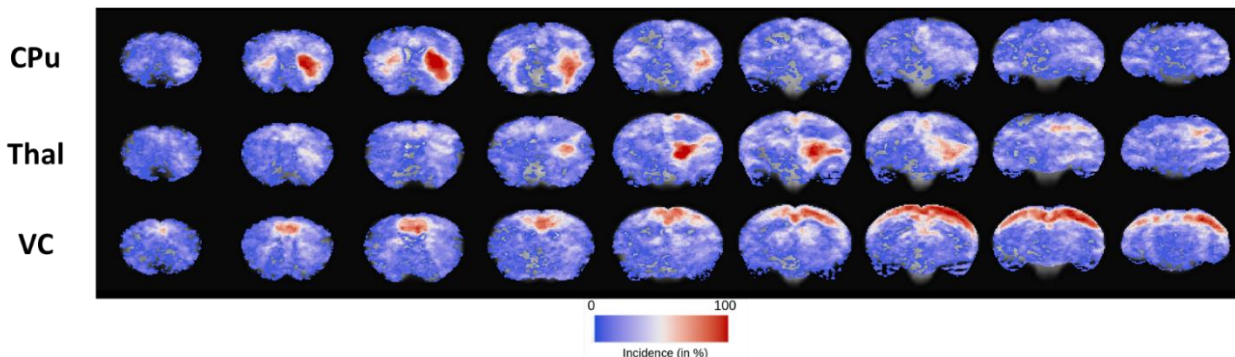


**Figure 3.23:** Coincidence map for the baseline preprocessing pipeline, for the lower resolution dataset. Example for seeds in CPu = Caudate Putamen, Thal = Thalamus, and VC = Visual Cortices. Values of incidence are presented in percentages (blue = low incidence, red = high incidence).

As can be observed, these maps are consistent with the corresponding connectivity maps, and this was verified through all seeds and pipelines. Regions showing a high incidence (from 50 to 100%) appear in the final clusters, whereas regions with a low incidence (<50%) do not.

Finally, an interhemispheric connectivity analysis was carried out, to check for preprocessing pipeline differences, and illustrative results can be found in Figure 3.24.

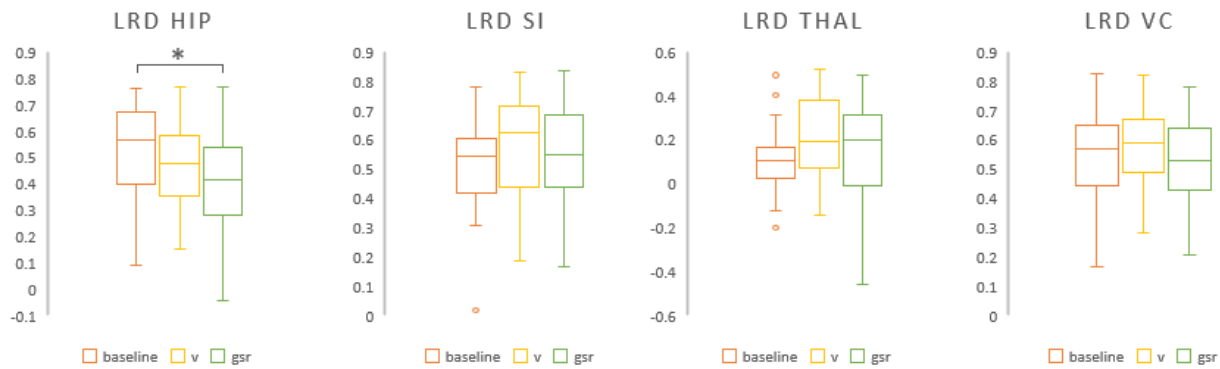


**Figure 3.24:** Boxplots showing representative correlation coefficients between 3 interhemispheric regions and 3 preprocessing pipelines, in the low-resolution dataset (LRD). HIP = Hippocampus, SI = Primary somatosensory cortex, THAL = Thalamus, VC = Visual Cortices. In the hippocampus region, a variation was found between baseline and GSR pipelines, at a significance of  $p < 0.05$ . The points outside the plots are outliers.

A two-sample two-tailed t-test was performed to check for pairwise differences between preprocessing pipelines. For the seven seeds, one significant difference was found between the baseline and the GSR pipeline for the hippocampal seed region. However, none of the seeds passed the Kruskal-Wallis test, a non-parametric test designed to search for significant differences in the distribution.

The mean correlation values found in the boxplots were consistent with the connectivity maps, as most seeds show both high interhemispheric correlation values (from 0.4 to 0.6) and bilateral networks. Accordingly, the most unilateral network, resulting from the thalamic seed, also holds the lowest mean interhemispheric correlation.

### 3.2.2.B. High Resolution

The analysis carried out on the high-resolution dataset was almost identical to the one carried out on the low-resolution one, with the exception that correlation thresholding was performed at a slightly lower value of 0.15. This was done to compensate the SNR decrease, consequence of the resolution increase. An example of a typical individual connectivity map can be seen in Figure 3.25.

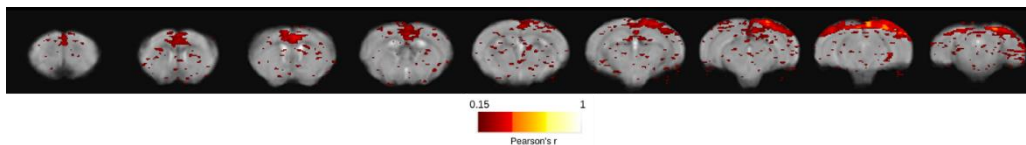


**Figure 3.25:** Connectivity map from an individual high-resolution run with the baseline preprocessing pipeline, with a seed in the left visual cortex (VC). Pearson correlation values thresholded at a minimum of 0.15, with a corresponding maximum p-value of 0.004. Slices are presented from the rostral to the caudal part of the brain (from left to right in the figure), and the data is overlaid on top of the averaged functional runs, in atlas space.

As could be verified in the lower resolution dataset, the area surrounding the seed region, in the VC, has the highest correlation values. Bilateral signal can also be observed, in the contralateral region of

the seed, and once again, multiple smaller regions also appear as correlated with the seed region. These smaller clusters appear to be even more scattered than in the lower resolution dataset, and their size is smaller than in the low-resolution datasets, which is consistent with the dataset's smaller voxel size. An example of a statistical map is depicted in Figure 3.26.

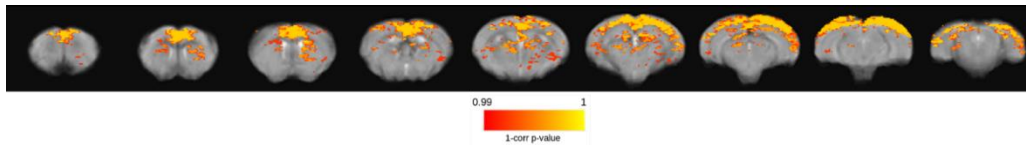


**Figure 3.26:** Statistical map from 9 individual connectivity maps, from the high-resolution dataset, with a seed in the VC, thresholded at  $p < 0.01$ . Values are presented as 1-corr p-value, i.e. 0.99 corresponds to a p-value of 0.01, corrected for FWE. Slices are presented from the rostral to the caudal part of the brain (from left to right in the figure), and the data is overlaid on top of the averaged functional runs, in atlas space.

It is possible to notice that the region corresponding to a  $p < 0.01$  is smaller than in the lower resolution dataset. The final connectivity maps for the baseline, GSR and ventricular signal regression pipelines are presented in Figure 3.27, Figure 3.28, and Figure 3.29, respectively.

Identically to the lower resolution dataset, these averaged maps have better defined connectivity regions. Scattered regions previously appearing as correlated with the seeds are mostly not present, contrarily to what occurred in individual maps.

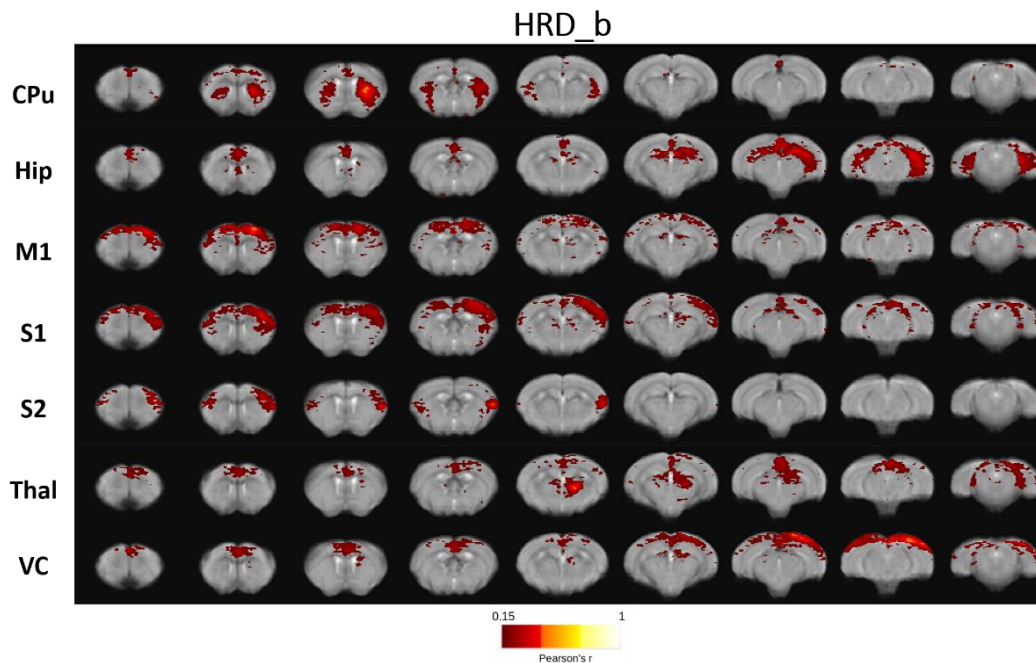


**Figure 3.27:** Connectivity maps, averaged from 9 runs from the high-resolution dataset (HRD), preprocessed with the baseline pipeline. Seven seeds were positioned on the left side of Caudate Putamen (CPu), Hippocampus (Hip), Primary Motor Cortex (M1), Primary (S1) and Secondary (S2) Somatosensory cortices, Thalamus (Thal) and Visual Cortices (VC). Thresholds at 0.2 Pearson correlation,  $p < 0.01$  and minimum cluster size of 10 voxels. Slices are presented from the rostral to the caudal part of the brain (from left to right in the figure), and the data is overlaid on top of the averaged functional runs, in atlas space.

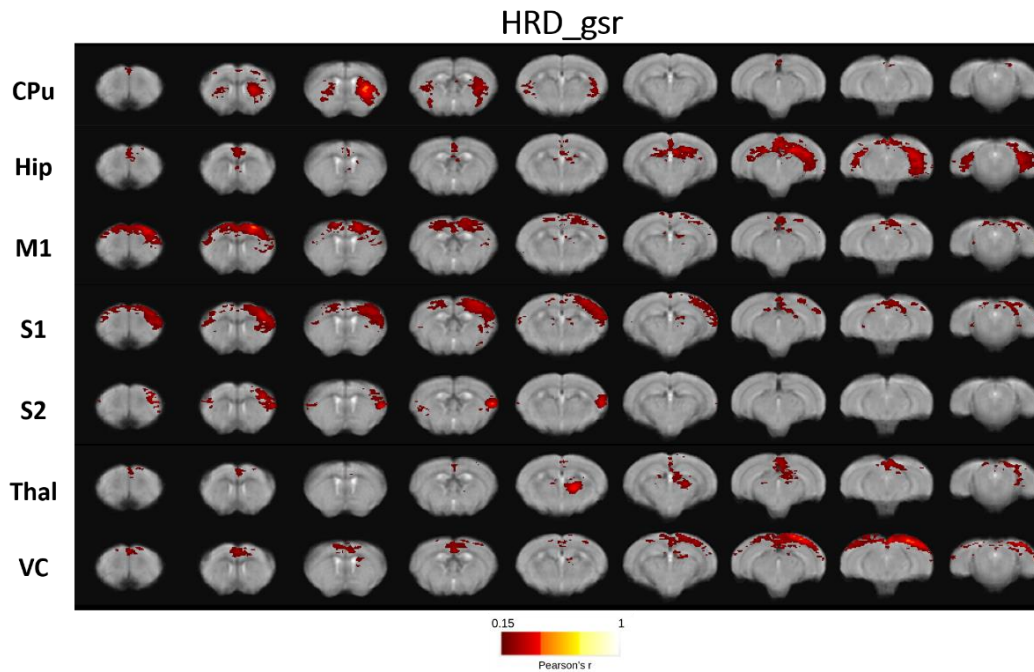


**Figure 3.28:** Connectivity maps, averaged from 9 runs from the high-resolution dataset, preprocessed with the pipeline performing GSR. Seven seeds were positioned on the left side of Caudate Putamen (CPu), Hippocampus (Hip), Primary Motor Cortex (M1), Primary (S1) and Secondary (S2) Somatosensory cortices, Thalamus (Thal) and Visual Cortices (VC). Thresholds at 0.2 Pearson correlation,  $p < 0.01$  and minimum cluster size of 10 voxels. Slices are presented from the rostral to the caudal part of the brain (from left to right in the figure), and the data is overlaid on top of the averaged functional runs, in atlas space.

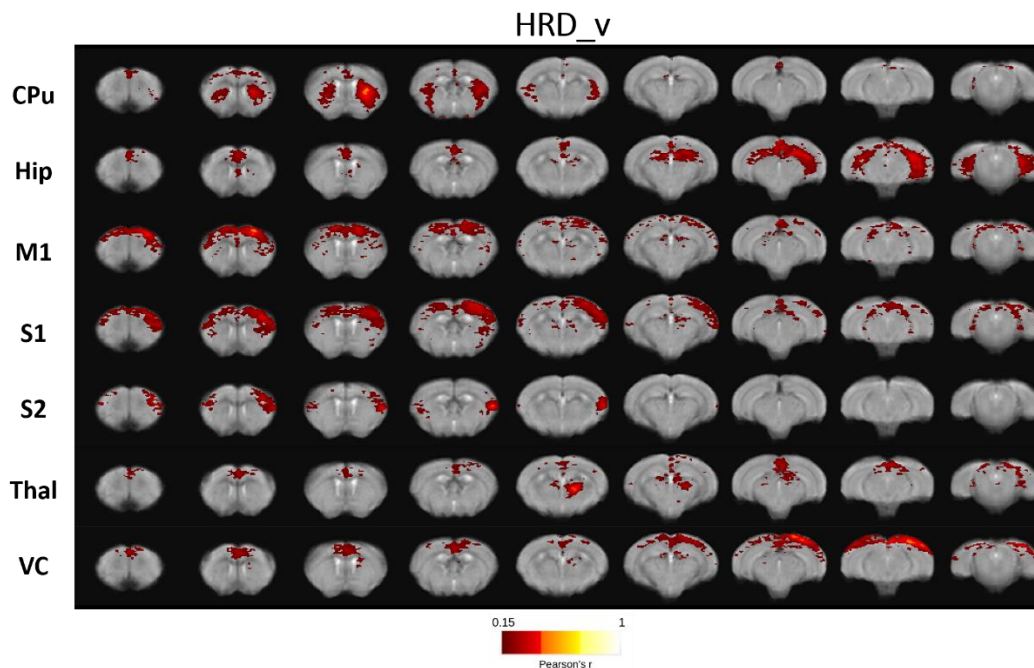


**Figure 3.29:** Connectivity maps, averaged from 9 runs from the high-resolution dataset, preprocessed with the pipeline performing ventricular signal regression. Seven seeds were positioned on the left side of Caudate Putamen (CPu), Hippocampus (Hip), Primary Motor Cortex (M1), Primary (S1) and Secondary (S2) Somatosensory cortices, Thalamus (Thal) and Visual Cortices (VC). Thresholds at 0.2 Pearson correlation,  $p < 0.01$  and minimum cluster size of 10 voxels. Slices are presented from the rostral to the caudal part of the brain (from left to right in the figure), and the data is overlaid on top of the averaged functional runs, in atlas space.

Once again, most networks have bilateral signal, although in these high-resolution datasets, contralateral clusters were more clearly smaller than ipsilateral ones. For example, in both S1 and S2 networks, a clear difference can be seen between clusters on the left and right side. The thalamic network appears once again to be more unilateral, although there is now bilateral signal. Even considering that the right cluster is smaller than the left one, the difference is not as striking as in the lower resolution dataset, since most right clusters exhibit a smaller size when compared to left clusters. Additionally, the previously observed striped pattern correlating with non-grey matter areas is no longer observed.

Similarly, to what was previously observed, it can be noticed that the VC network appears to include the ACA and RSP, which interestingly are also included in the Hip and Thal network, and that there are some overlapping clusters on M1, S1 and S2 networks.

The three pipelines resulted in similar maps, as before. Cluster size does not vary greatly, especially considering the number of voxels of the largest clusters in each map, although slightly lower values are generally found on the GSR pipeline, i.e. the clusters are tendentially smaller. Most of the features mentioned are common to all pipelines. Once again, some of the smaller clusters in the baseline and ventricular regression pipelines disappear, when using the GSR pipeline. For example, in S1 and Thal networks, the correlated area is slightly reduced, with the number of voxels on the largest cluster decreasing approximately 30%.

Coincidence maps were computed as well, measuring the percentage of times that each voxel was equal or above to the correlation threshold. In Figure 3.30, it is possible to see representative coincidence maps for three of the seeds.

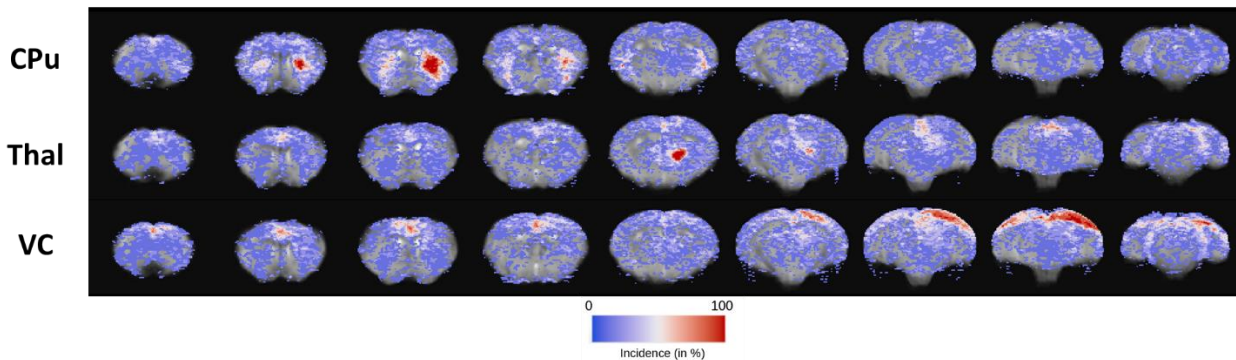


**Figure 3.30:** Coincidence maps for the baseline preprocessing pipeline, for the high-resolution dataset. Example for seeds in CPu = Caudate Putamen, Thal = Thalamus, and VC = Visual Cortices. Values of incidence are presented in percentages (blue = low incidence, red = high incidence).

Coincidence maps are consistent with the corresponding connectivity maps, and this was verified through all seeds and pipelines. Regions showing a high incidence (from 50 to 100%) appear in the final clusters, while regions with a low incidence (<50%) do not. However, overall incidence values are slightly lower than in the lower resolution dataset.

Lastly, an interhemispheric connectivity analysis was carried out, to check for preprocessing pipeline differences, and illustrative results can be found in Figure 3.31.

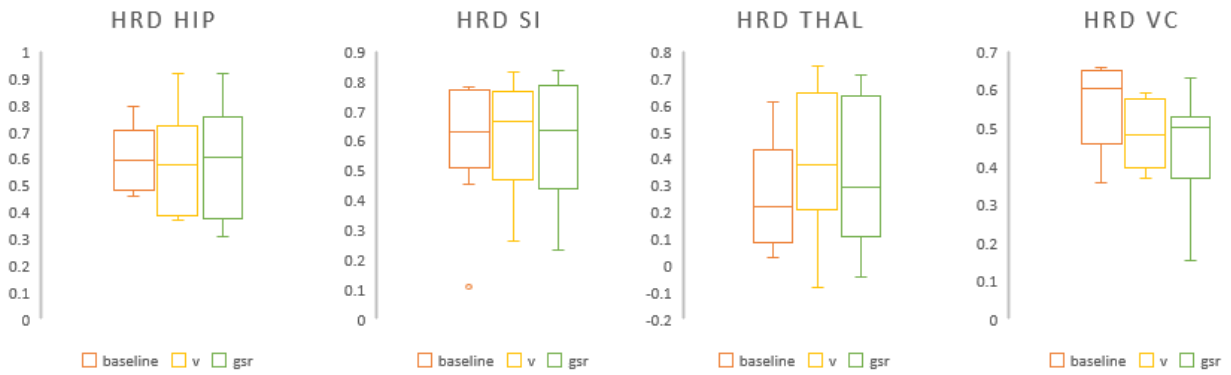


**Figure 3.31:** Boxplots showing representative correlation coefficients between 3 interhemispheric regions and 3 preprocessing pipelines, in the high-resolution dataset (HRD). HIP = Hippocampus, SI = Primary somatosensory cortex, Thal = Thalamus, VC = Visual Cortices. The points outside the plots are outliers.

A two-sample two-tailed t-test was performed, as well as a Kruskal-Wallis test, and no significant differences were discovered in either test. As in the lower resolution dataset, the mean correlation values found in the boxplots were consistent with the connectivity maps, as most seeds show both high interhemispheric correlation values (from 0.5 to 0.6) and bilateral networks. Interestingly, the thalamic network shows a slightly higher value of mean interhemispheric correlation, compared to the lower resolution dataset, also consistent with the corresponding connectivity map.

## 4. Discussion

This section presents the discussion of the results displayed in the previous chapter, as well as some general considerations, regarding the choices made throughout the experiments.

As it was previously stated, rsfMRI is a noisy technique, difficult to perform in mice, and the mapping of murine functional networks is usually performed under a rather low spatial resolution, which does not allow the targeting of smaller structures in the brain. Moreover, most studies are conducted using medetomidine anesthesia, which affects the LC noradrenergic system. In the lab in which the current work was performed, this system is of particular interest, and rsfMRI had not yet been established. Therefore, the goals of this project included: to establish an MRI protocol suitable for rsfMRI acquisition in mice; to explore urethane anesthesia (as an alternative for medetomidine); to establish and optimize a robust preprocessing and analysis pipeline for murine RSN mapping; and to map these networks on standard (low) resolution, as well as in higher resolution datasets.

Concerning the choices made for the MRI protocol, a GE-EPI was selected for this study. Since it is  $T_2^*$  dependent, it is sensitive to BOLD contrast, but it is more susceptible to magnetic field inhomogeneities' effects (which can result in distortions and signal losses, mostly in air-tissue interface areas). GE sequences might also reflect hemodynamic effects from large vessels, which can cause BOLD signal detection in areas where no neuronal activation occurs. SE sequences often reflect more accurately changes in the vasculature on a microscopic level instead of large vessels and are consequently more spatially specific. They are also less prone to distortions or signal losses caused by field inhomogeneities, since they are  $T_2$  dependent, but they are consequently less sensitive to BOLD contrast, which translates into a lower obtained MR signal. Considering that the resting state changes in BOLD signal are already quite small *a priori*, this was a too great drawback. Additionally, TE and TR values might be too short for an ideal  $T_2^*$  weighting, which is characterized by long TE and TR parameters, but these would compromise temporal resolution. It should be noticed that other contrasts can be used instead of BOLD, such as CBV [72] or even CBF. These different options could be explored in future work.

While the high field is almost indispensable when imaging mice, due to its SNR enhancement (also augmented by the combined use of cryocoils), EPIs become even more susceptible to field inhomogeneities, and those must be corrected as well as possible.

Regarding the data analysis, some considerations should be taken into account. In the preprocessing pipeline, different values were tested for the frequency cut-offs, as there is no consensus on which should be the optimal values. Although a low-pass cutoff of 0.1 Hz is typical and also delivered plausible bilateral maps, a more conservative value of 0.2 Hz was chosen for the final pipeline, to avoid unnecessary manipulations of the data. Different values for isotropic and 2-D spatial smoothing were also tested, but no significant difference was found. Therefore, a 2-D smoothing with a Gaussian kernel with a FWHM = pixel dimension was chosen, as to minimize partial volume effects especially on the slice direction, which has

already a larger thickness compared to pixel dimension. For the postprocessing, an SBA was chosen as the main analysis method. As a hypothesis-driven approach, seed-based analysis is limited to the dynamics of the seed region. By performing several analyses using different seeds, the potential limitation of this approach was attenuated, although possibly interesting networks might remain undiscovered [62]. Still, it is a robust and simple technique which allows network mapping, and given its straightforward interpretation, it was considered the most adequate approach for this study.

## 4.1. Optimization of Acquisition Parameters

Overall, the initial outcomes of this optimization phase were not entirely satisfactory, and there were many issues that could be improved. Still, most of them could be overcome or bypassed in posterior acquisitions, and there were encouraging results that could be further explored in the future.

### 4.1.1. Preliminary Resting State fMRI Acquisitions

The major obstacle encountered in these preliminary acquisitions were the ghosting artifacts, as could be observed in Figure 3.2. This issue prevailed on both medetomidine and urethane acquisitions and caused more than half of the runs to be discarded. The ghosts might have been caused by gradient coil heating, which is common in EPI acquisitions, animal motion, or even reconstruction errors. Another possible cause could be eddy currents, induced by the varying magnetic field, which distort the  $B_0$  field, and add phase shifts to the data, creating ghosts in the image, after reconstruction [128]. Reducing phase-encoding resolution might have reduced these artifacts, but that was not compatible with the ambitious goal of acquiring very high spatial resolution data. A single-shot EPI could have reduced these artifacts, and was tested as well, but the consequent EPI distortions were too great, rendering the images unusable.

Regarding the final connectivity maps obtained for the preliminary acquisitions, of which an illustrative example can be found in Figure 3.3, there were not clear and well-defined clusters of correlated areas, and FC was observed mostly in a very small region adjacent to the seed. The observed stripes could have perhaps originated from vascular signal that was not removed, and there was not much bilateral signal observed.

Considering that this was the analysis pipeline had not yet been validated, an exploratory ICA was carried out, to obtain spatial maps in a more data-driven way. The resulting independent components had to be manually classified as signal or noise, and features such as a low number of large clusters in grey matter regions, or a largely low frequency spectral density with a large peak below 0.1 Hz were considered as expected from signal ICs [129][130]. Once again, no clear networks could be identified. Spatial maps, shown in Figure 3.4, consisted of either big regions overlapping with either brain borders, white matter or CSF; striped patterns (possibly resulting from vasculature); or numerous very small clusters, scattered in an apparent random manner. Representative power spectrums of the ICs did not have a clearly defined

peak below 0.1 Hz, as could be observed in Figure 3.5, which lead to the classification of most of ICs as noise. It should be noted that this analysis was only performed as a rather quick complementary method to understand whether the main issues causing the initial underwhelming results were due mostly to data acquisition, or its posterior analysis. Since the ICA did not allow functional network mapping, and the preprocessing pipeline appeared to be robust, the major challenges were thought to lay in the data acquisition phase. Even considering only the runs that were not very severely affected by ghosting artifacts, the resolution might have been too high, causing an SNR too low for a rsfMRI experiment. The flip angle ( $55^\circ$ ) might also have been too low (compared with the  $75^\circ$  subsequently used), and not allow enough signal to be obtained. However, it was necessary for an adequate temporal resolution in the current sequence. At 9.4T, the  $T_1$  relaxation times in the brain structures used as seeds ranged between 1500 ms and 2000 ms [131], in mice. Considering a 2000 ms TR, the corresponding Ernst angles are approximately  $75^\circ$  and  $70^\circ$ , for each  $T_1$ . Hence, the initial flip angle was indeed lower than what would be optimal, perhaps not allowing enough MR signal to be measured. The  $75^\circ$  angle, that was possible to use in the following experiments, was chosen taking these factors into account, which might also elucidate the more successful acquisitions. This could also explain the low tSNR (an average of 29.7) across animals, compared to the subsequent acquisitions.

Additionally, some functional images showed severe distortions, and ultimately, only a small number of runs (6 total) remained useable, which might have not provided enough statistical power for a successful network mapping at this resolution.

Regarding the acquisitions under urethane anesthesia, since the mice were fairly stable during the bench testing, a few resting state runs were acquired, as it could help solving some of the previous issues. However, the faster breathing rate is likely to have caused additional animal movement, responsible for an increase of the proportion of runs with ghosting artifacts and runs with a very large number of outliers, resulting in only one usable dataset. Considering the very reduced sample, the small number (3 total) of scanned animals (which is an impactful confounding factor), and that the previous issues (ghosting artifacts and EPI distortions) only seemed to be enlarged, this single run was not further analyzed. Since urethane is a terminal anesthesia, further experiments are advised to be carried out, only after a more robust and high-resolution sequence has been established previously using other anesthetics, and for investigation of structures that are affected by other anesthetic regimes.

#### 4.1.2. Urethane Characterization

As could be observed from the bench testing results, in Table 3.1, breathing and temperature rates were stable for a long time. Despite the results of posterior scanning sessions, it could be observed that the mice were did not wake mid-experiment, unlike in some medetomidine cases, and seemed to be physiologically stable.

It could be observed, however, that for this stability to be achieved, the animals must be allowed to stabilize for a long time before the experiments (approximately one hour), since immediately following

urethane injection, the mice were still highly reactive, moving and showing signs of wakefulness. Considering the extremely loud noises on the scanner, putting the mice on these circumstances would be both unethical and simply not viable for adequate resting state acquisitions.

Higher dosages of urethane can perhaps be tested in the future. Even though fasting the animals prior to the experiment could prove an efficient method for a faster anesthetic effect, it has been shown to alter FC in mice [84]. If further studies using other dosages of urethane should be carried out, it might prove advisable to perform additional measurements on the bench tests, such as partial pressure of oxygen and carbon dioxide, and blood pressure, to further ensure the mouse physiology over time.

Overall, although the subsequent acquisitions were not successful, as discussed in the previous subsection, urethane proved to be a stable anesthetic throughout the sessions, and it might be a viable option in future studies. However, although the ghosting artifacts were not present in posterior experiments, this could still prove to be an issue in further urethane acquisitions.

## 4.2. Resting State fMRI Experiments

### 4.2.1. Low Resolution

The lower resolution runs exhibited only minor distortions and no ghosting artifacts, as could be observed in Figure 3.7, allowing for a bigger portion of runs to be considered in the final analysis. There was a consistent high tSNR throughout the experiments, although it should be noticed that within the same animal there are some variations across the image. This means that, since the coil used for signal reception is a surface coil, the measured signal in subcortical areas is lower. The obtained average tSNR values (92.7 and 53.8 for the low- and high-resolution dataset, respectively) are quite good comparing to previous literature. These values seem to vary greatly across experiments, due to different magnetic field strengths and spatial resolutions [112], but they might also change significantly within the same experiment, possibly due to fluctuations of physiological factors [52]. tSNR values range mostly from 20 to 70 in the literature, for fMRI experiments in the mouse brain at comparable resolution, and a tSNR equal or higher to 50 can be considered as suitable [52]. Thus, both low- and high-resolution datasets of the current experiments can be considered to have performed well, especially taking into account that most of the values in the literature were from lower resolution datasets (0.2 mm  $\times$  0.2 mm pixel dimension, or higher), and that the high tSNR value was mostly constant throughout the experiments (the worst values were 67.3 and 40.7, in the low- and high-resolution datasets, respectively).

For these acquisitions, the goal was to follow the protocol established by Nasrallah et al. [93] as closely as possible, in order to reproduce the stable bilateral networks in the current lab. Two more slices could be acquired, comparing to the original study, while keeping the remaining parameters constant, and the anesthesia protocol was changed from an intraperitoneal constant infusion, to a subcutaneous administration. Although this change might alter the time that took for the animals to be sedated, since the

absorption rate is slightly slower, subcutaneous administration is simpler and less invasive for the animal, thus being considered a good alternative to intraperitoneal injection.

Regarding the overall observed networks, in Figure 3.20, Figure 3.21, and Figure 3.22, they were mostly consistent with previous literature. Bilateral networks had already been observed in rats [132], which suggests that these networks are preserved in rodents. Although there had been previous studies where more unilateral networks had been observed in mice [61], several studies have shown ever since that it can be possible to obtain bilateral networks in mice as well [93][111]. This means that in most networks, the connected regions extended beyond the seed and had an approximately equal area on the contralateral side, which is also in accordance with optical imaging findings [133]. The lack of bilateral signal observed in some studies is thought to be due to animal physiology, which is harder to maintain in the mouse, compared with rat.

It is also interesting to notice that these bilateral networks are not merely caused by existing structural connectivity. For example, while the left and right S1 are connected via corpus callosum, left and right caudate putamen are not [21], and still show a strong interhemispheric correlation. This is caused by their synchronized activity, which is suggested to reflect communication between regions. However, this communication might not be necessarily direct, as other various inputs (from one or more different regions) might cause their covariance. Thus, it is difficult to infer causality from any of these resting state networks.

Concerning now some specific RSNs, it was possible to see that M1, S1 and S2 networks were partly overlapping. Interestingly, these regions had already been shown to be functionally connected, since the first resting state experiment ever performed, in humans [59]. Additionally, some rodent rsfMRI studies performing SBA allowed the mapping of the so-called somatomotor network [134][73], a network englobing the individual motor and somatosensory (M1, S1 and S2) RSNs. ICA studies in mice had already allowed the differentiation of these independent networks [61], with overlaps, as found in this present study.

Another consistent finding was the anteroposterior connectivity along the midline, observed in the VC network. It was possible to see that the ACA and RSP were functionally connected to the primary visual cortex, as observed in rats [132] and mice [61].

Despite the good overall results, the thalamic seed only showed ipsilateral functional connectivity. A possible reason for the inconsistency of these results with previous literature can be a misregistration of the functional data, although this hypothesis is unlikely, since the seeds were delineated on top of the averaged functional runs, in the atlas space, and there seemed to be no discrepancies across the runs. A more probable cause for this would be the seed itself, since its specific location, size and shape can have a great impact on the final maps. Different seed sizes were tested, with identical results, but perhaps a combination of these factors could have resulted in the suboptimal mapping of the thalamic network. Partial volume effects should also be considered. The seeds were delineated avoiding transitions between areas, as to minimize PVE, but even slight misregistrations could cause seed region voxels to include signal from unwanted regions. This issue is expected to be less relevant in the higher resolution datasets, due to the lower pixel dimensions. Furthermore, the times of acquisition were not equal for all runs, as they were highly dependent on animal stability in the scanner. Therefore, considering that medetomidine has time-dependent

effects on functional connectivity [104], this might have caused some additional variability on the FC patterns of the mice. Lastly, the subcortical location of this region can also be a probable cause for this result, as the inherently lower SNR in these areas could result in more inconstant individual connectivity maps, and a consequent inaccurate averaged map.

Regarding coincidence maps, in Figure 3.23, they were found to be consistent with connectivity maps, as the areas that survived the thresholding in the connectivity maps show a high coincidence value. Also, they illustrate how noisy the individual datasets are. Almost the entirety of the brain had not null coincidence values. This means that unrelated regions would appear as functionally connected to the seed region, in at least one run. This demonstrates the importance of averaging more animals, to have statistical power for a successful network mapping.

Preprocessing pipelines are a continuous source of debate, in rsfMRI. In this study, three different nuisance removal methods were tested, but no highly significant differences were found. Only one of the 21 pairwise comparisons (or 42, considering comparisons from low- and high-resolution datasets) was found to be significant at a  $p < 0.05$ , and no difference could be seen in the distribution values. As could be seen in the interhemispheric connectivity boxplots, in Figure 3.24, individual connectivity values were quite spread, normally ranging from 0.1 to 0.8, with the exception of the Thalamus, which exhibited lower values. No pipeline was found to consistently have higher or lower interhemispheric connectivity than the others, although through visual inspection, and general results, the GSR pipeline seemed to have slightly lower correlation values. This could be expected, since GSR removes a lot of variance in the data, compared with the other nuisance regression alternatives. This also explains why the typical cluster size was smaller in GSR maps. Although interhemispheric analysis is often performed to measure or compare FC patterns “quality”, it should be noted that a higher correlation value does not always necessarily indicate a better network. As was seen in the ROI analysis, perhaps spurious correlation values can be caused by structured noise, and not by physiological network dynamics. Therefore, these results should always be interpreted cautiously, and a visual inspection of the final maps can prove constructive. Besides an interhemispheric correlation analysis and a visual inspection of the data, it is difficult to further investigate differences between pipelines. Since rsfMRI does not have any paradigm, it is difficult to discern if clusters subsequent from either pipeline are indeed belonging to neuronal networks, or mere results from sources of structured noise.

While medetomidine sedation proved to result in overall successful results, a possibly better regime could be attempted, by using a combination of medetomidine and isoflurane, which has already been shown to result in better FC patterns in mice [89][96]. This was the sedation regime used in the preliminary acquisitions, but perhaps with the established MRI protocol and analysis pipeline, it might have better results in the future. An interesting way to assess pipeline performance could be by comparing the results to those obtained in awake rodents. This was done already in rats [91], instead of the typical interhemispheric correlation analysis done in mice [89]. Awake mice imaging could be an even more interesting path, as anesthesia bias is one of the current major pitfalls of preclinical fMRI studies. Endotracheal intubation and ventilation could be a possible improvement in the case of imaging of anesthetized animals, as it tightly controls the rodent’s breathing rate. However, both awake mice imaging and intubation are extremely

challenging and time-consuming. Therefore, they would not be likely to be achievable in the time frame of the current project. The use of isoflurane could also be beneficial since, in the present study, the used medetomidine dosage (0.6 mg/kg/h) was found to deliver a very light sedation. This often cause the mice to wake up mid experiment, usually after minimal increases of temperature, and ultimately lead to the session's premature end. This was not consistent with what is described in [93], where it is reported that half of this dosage would result in mice stability up to six hours.

#### 4.2.2. High Resolution

Similarly to what was found in lower resolution runs, overall results of high-resolution runs were quite positive. The raw data had a very good quality, and despite the high resolution, no ghost artifacts were found, as can be seen in Figure 3.8.

Most findings already described and discussed in the low-resolution runs were also verified in the higher resolution runs. In the connectivity maps, in Figure 3.27, Figure 3.28, and Figure 3.29, values of correlation were expected to be lower, due to the decreased tSNR, hence the reduced correlation threshold. This results in slightly "noisier" maps, with a higher number of small clusters, but bilateral networks were still clearly observed, as well as ACA and RSP connectivity along the midline. However, the decreased SNR has clear effects, for example, in the coincidence maps, in Figure 3.30. It is possible to notice that there is a general decrease of incidence in the connected areas. While it still allows for network detection, it shows that the data is slightly more variable, and not as coherent as the low-resolution data. This is also in agreement with the generally lower correlation values that can be found in the higher resolution dataset, evidenced by the slightly darker colored maps. Analyses at higher resolution will therefore require larger sample sized to overcome the impact of the reduced SNR.

Upon visual inspection, GSR pipeline seems to remove some small significant clusters appearing in the remaining pipelines, and it results in a modest decrease in the size of the largest clusters. However, interhemispheric connectivity analysis, depicted in Figure 3.31, did not deliver any significant results. Ventricular signal regression seemed to generally result in a slightly higher connectivity across several seeds. This could be since ventricular masks are delineated in very small areas, they can have severe partial volume effects, which are minimized in higher resolutions. Once again, interhemispheric correlation analysis' limitation should be acknowledged, and significant conclusions cannot be made based on such slight differences.

An unexpected change was found in the thalamic network, which showed some bilateral connectivity despite this dataset's lower tSNR. This moderate improvement might have been due to an increased spatial specificity, which could cause the vascular effects to be less severe. Additionally, any possible existing misregistration issues might have been attenuated, since the higher resolution datasets result in a more accurate alignment.

Lastly, considering a possible future project specifically targeted at LC imaging, some factors should be considered. Medetomidine is known to cause a prominent decrease of norepinephrine release and an overall inhibition in the sympathetic nervous system, since it acts mainly on presynaptic receptors in the Locus Coeruleus [100][102][103]. Thus, different sedation regimes, such as urethane or even propofol, should be used, when aiming at LC imaging. Both anesthetics have been shown to deliver good FC patterns in rodents [91], as well as suitable cortical interhemispheric connectivity in mice [89], although striatal connectivity appeared to be suboptimal. Another factor that should be taken into account is the slice coverage: LC is anatomically positioned ventrally to the beginning of the cerebellum, which coincides with the last slice of most runs in this dataset, as seen in Figure 2.5, and in two of the nine runs, the LC region could not be imaged, due to insufficient coverage. Perhaps a wider coverage could be attempted, either with a higher number of slices, or through an increased slice thickness. The latter option, however, is not recommended, since the current slice thickness is already larger than pixel dimension and can result in significant PVE. A mere shift in the slice coverage could prove sufficient, although in some cases it might compromise the imaging of the beginning of the motor cortex. Finally, when considering the seed-based analysis with the LC as a seed region, perhaps individual seeds should be defined for each individual functional run, and only the resulting connectivity map converted into atlas space. This might allow a more accurate delineation of this small structure, and a thus robust network mapping. To facilitate seed delineation, a higher resolution slab covering the LC region could be acquired since it would allow direct LC identification. This slab should be acquired using an appropriate contrast, such as T1-weighted MRI with magnetization transfer, based in the neuromelanin content, which has already allowed identification of the LC in mice [135].

In this project, a robust protocol for resting state fMRI in mice, along with a state-of-the-art analysis pipeline has been established. To our knowledge, this is the highest resolution achieved in a resting state functional connectivity study in mice, so far. Although one study has been performed with a 0.1 mm isotropic pixel resolution, no network mapping was performed, and the brain was segmented into regions composed by a group of 80 to 2000 voxels [84], making its effective resolution considerably lower. Overall, the results presented here are promising, although further improvements can be attempted in future studies.

## 5. Conclusions and Future Work

This project was aimed towards the establishment of a robust MRI protocol and an analysis pipeline allowing the mapping of RSNs in mice. More specifically, the goal was to 1) establish a protocol using typical parameters from the literature in the lab and 2) perform similar experiments at higher resolution to allow the future study of smaller structures. A different anesthetic (urethane) was also tested, as an alternative for medetomidine, which affects the LC noradrenergic system.

It was possible to establish and optimize a robust preprocessing pipeline, with three variants, and an analysis pipeline for murine RSN mapping. Bilateral networks were found in both datasets and features consistent with previous literature, especially in the CPU, Hip, M1, S1, S2, and VC. These findings are consistent with previous literature that suggested that RSNs are preserved across rodents [60][20]. A thalamic network could be observed in the higher resolution datasets, but the functionally connected clusters contralateral to seed region was small. Connectivity along the midline was also reported in both datasets, as well as an overlap in the M1, S1 and S2 networks, consistent with previous reports of a somatomotor network. Preprocessing was performed with a baseline pipeline, a GSR variant and ventricular regression variant, no significant differences were found across pipelines. The baseline pipeline is therefore recommended, as it avoids the additional manual drawing of ventricular masks and the controversy surrounding GSR, respectively. Additionally, urethane was found to deliver a stable and lasting effect on bench tests, but further measurements should be performed before rsfMRI experiments should be carried out with this anesthetic.

These are encouraging results and are indicative that even higher resolution could be attempted in the future. Different anesthetics, as well as other FC metrics can also be investigated, such as dynamic FC [86], graph theory [85] or ALFF [84].

In conclusion, considering the high variability on data acquisition parameters, anesthetic regimes, preprocessing and analysis pipelines used in FC studies, these consistent network mappings are a promising result for rsfMRI in mice as a translational tool for the study of large-scale neural dynamics, as well as the fundamental mechanisms of small structures in the brain.



## 6. References

- [1] D. Drubach, *The Brain Explained*. Pearson, 1999.
- [2] R. M. Birn, "The role of physiological noise in resting-state functional connectivity," *Neuroimage*, vol. 62, no. 2, pp. 864–870, 2012.
- [3] J. Smucny, K. P. Wylie, and J. R. Tregellas, "Functional magnetic resonance imaging of intrinsic brain networks for translational drug discovery," *Trends Pharmacol. Sci.*, vol. 35, no. 8, pp. 397–403, 2014.
- [4] H. Lu and E. A. Stein, "Resting state functional connectivity : Its physiological basis and application in neuropharmacology," *Neuropharmacology*, vol. 84, pp. 79–89, 2014.
- [5] M. D. Fox and M. E. Raichle, "Spontaneous fluctuations in brain activity observed with functional magnetic resonance imaging," *Nat. Rev. Neurosci.*, vol. 8, p. 700, Sep. 2007.
- [6] N. Nallasamy and D. Y. Tsao, "Functional Connectivity in the Brain: Effects of Anesthesia," *Neurosci.*, vol. 17, no. 1, pp. 94–106, Feb. 2011.
- [7] K. H. Chuang and F. A. Nasrallah, "Functional networks and network perturbations in rodents," *Neuroimage*, vol. 163, no. August, pp. 419–436, 2017.
- [8] A. M. Belcher *et al.*, "Large-Scale Brain Networks in the Awake , Truly Resting Marmoset Monkey," vol. 33, no. 42, pp. 16796–16804, 2013.
- [9] H. Lu, Q. Zou, H. Gu, M. E. Raichle, E. A. Stein, and Y. Yang, "Rat brains also have a default mode network," *Proc. Natl. Acad. Sci.*, vol. 109, no. 10, pp. 3979 LP – 3984, Mar. 2012.
- [10] C. Guedj, E. Monfardini, A. J. Reynaud, A. Farnè, M. Meunier, and F. Hadj-Bouziane, "Boosting Norepinephrine Transmission Triggers Flexible Reconfiguration of Brain Networks at Rest," *Cereb. Cortex*, vol. 27, no. 10, pp. 4691–4700, Sep. 2016.
- [11] X. Huang, Z. Long, and X. Lei, "Electrophysiological signatures of the resting-state fMRI global signal : A simultaneous EEG-fMRI study," *J. Neurosci. Methods*, vol. 311, no. September 2018, pp. 351–359, 2019.
- [12] T.-L. Wu *et al.*, "Intrinsic functional architecture of the non-human primate spinal cord derived from fMRI and electrophysiology," *Nat. Commun.*, vol. 10, no. 1, p. 1416, 2019.
- [13] A. M. Packer, L. E. Russell, H. W. P. Dalglish, and M. Häusser, "Simultaneous all-optical manipulation and recording of neural circuit activity with cellular resolution in vivo," *Nat. Methods*, vol. 12, p. 140, Dec. 2014.
- [14] R. W. Chan, A. T. L. Leong, L. C. Ho, P. P. Gao, E. C. Wong, and C. M. Dong, "Low-frequency hippocampal – cortical activity drives brain-wide resting-state functional MRI connectivity," 2017.
- [15] L. Luo, E. M. Callaway, and K. Svoboda, "Genetic Dissection of Neural Circuits," *Neuron*, vol. 57, no. 5, pp. 634–660, Mar. 2008.
- [16] M. A. Bedell, N. A. Jenkins, and N. G. Copeland, "Mouse models of human disease. Part I: techniques and resources for genetic analysis in mice.," *Genes Dev.*, vol. 11, no. 1, pp. 1–10, Jan. 1997.
- [17] C. Martin, "Contributions and complexities from the use of in vivo animal models to improve understanding of human neuroimaging signals," *Front. Neurosci.*, vol. 8, p. 211, Aug. 2014.
- [18] E. Jonckers, D. Shah, J. Hamaide, M. Verhoye, and A. Van der Linden, "The power of using functional fMRI on small rodents to study brain pharmacology and disease," *Front. Pharmacol.*, vol. 6, p. 231, Oct. 2015.
- [19] K. Murphy, R. M. Birn, and P. A. Bandettini, "Resting-state fMRI confounds and cleanup," *Neuroimage*, vol. 80, pp. 349–359, 2013.
- [20] D. N. Guilfoyle *et al.*, "Functional connectivity fMRI in mouse brain at 7T using isoflurane," *J. Neurosci. Methods*, vol. 214, no. 2, pp. 144–148, Apr. 2013.
- [21] W.-J. Pan, J. C. W. Billings, J. K. Grooms, S. Shakil, and S. D. Keilholz, "Considerations for resting state functional MRI and functional connectivity studies in rodents," *Front. Neurosci.*, vol. 9, p. 269, Aug. 2015.
- [22] S. Bouret and S. J. Sara, "Network reset : a simplified overarching theory of locus coeruleus noradrenaline function," vol. 28, no. 11, 2005.
- [23] S. J. Sara and S. Bouret, "Review Orienting and Reorienting : The Locus Coeruleus Mediates Cognition through Arousal," *Neuron*, vol. 76, no. 1, pp. 130–141, 2012.
- [24] L. A. Schwarz and L. Luo, "Minireview Organization of the Locus Coeruleus-Norepinephrine

- System,” *Curr. Biol.*, vol. 25, no. 21, pp. R1051–R1056, 2015.
- [25] A. S. Scott Huettel and G. McCarthy, *Functional Magnetic Resonance Imaging*. Sinauer, 2014.
- [26] A. G. Webb, “Introduction to Biomedical Imaging.” Wiley-IEEE-Press, p. 264, 2003.
- [27] R. A. Pooley, “AAPM/RSNA physics tutorial for residents: fundamental physics of MR imaging.,” *Radiographics*, vol. 25, no. 4, pp. 1087–1099, 2005.
- [28] J. T. Bushberg, J. A. Seibert, E. M. Leidholdt, and J. M. Boone, *The Essential Physics of Medical Imaging*, 3rd ed. Lippincott Williams & Wilkins, 2002.
- [29] R. M. Botnar and M. R. Makowski, “Cardiovascular magnetic resonance imaging in small animals,” *Prog. Mol. Biol. Transl. Sci.*, vol. 105, pp. 227–261, Jan. 2012.
- [30] D. Gilmore and K. Waterstram-Rich, *Nuclear Medicine and PET/CT*, 8th ed. Mosby, 2016.
- [31] P. Lauterbur, “Image Formation by Induced Local Interactions: Examples Employing Nuclear Magnetic Resonance,” *Nature*, vol. 242, no. 5394, pp. 190–191, 1973.
- [32] D. Kokorin, “Magnetic resonance imaging with spatially-selective pulses using multiple transmission channels,” 2015.
- [33] S. Ljunggren, “A simple graphical representation of fourier-based imaging methods,” *J. Magn. Reson. (1969)*, Vol. 54, Issue 2, p. 338-343., vol. 54, pp. 338–343, Jan. 1983.
- [34] R. Mezhich, “A perspective on K-space,” *Radiology*, 1996.
- [35] D. Moratal, A. Vallés-Luch, L. Martí-Bonmatí, and M. Brummer, “k-Space tutorial: an MRI educational tool for a better understanding of k-space,” *Biomed. Imaging Interv. J.*, vol. 4, no. 1, pp. e15–e15, Jan. 2008.
- [36] D. C. Preston, “MRI Basics,” 2006. [Online]. Available: [https://case.edu/med/neurology/NR/MRI Basics.htm](https://case.edu/med/neurology/NR/MRI_Basics.htm). [Accessed: 15-Oct-2019].
- [37] R. W. Brown, Y. C. N. Cheng, E. M. Haacke, M. R. Thompson, and R. Venkatesan, *Magnetic Resonance Imaging: Physical Principles and Sequence Design: Second Edition*, vol. 9780471720. Wiley-Blackwell, 2014.
- [38] L. Pauling and C. D. Coryell, “The Magnetic Properties and Structure of Hemoglobin, Oxyhemoglobin and Carbonmonoxyhemoglobin,” *Proc. Natl. Acad. Sci.*, vol. 22, no. 4, pp. 210–216, Apr. 1936.
- [39] K. R. Thulborn, J. C. Waterton, P. M. Matthews, and G. K. Radda, “Oxygenation dependence of the transverse relaxation time of water protons in whole blood at high field,” *Biochim. Biophys. Acta - Gen. Subj.*, vol. 714, no. 2, pp. 265–270, Feb. 1982.
- [40] S. Ogawa, T. M. Lee, A. R. Kay, and D. W. Tank, “Brain magnetic resonance imaging with contrast dependent on blood oxygenation,” *Proc. Natl. Acad. Sci. U. S. A.*, vol. 87, no. 24, pp. 9868–9872, Dec. 1990.
- [41] S. Ogawa and T.-M. Lee, “Magnetic resonance imaging of blood vessels at high fields: In vivo and in vitro measurements and image simulation,” *Magn. Reson. Med.*, vol. 16, no. 1, pp. 9–18, Oct. 1990.
- [42] N. K. Logothetis, J. Pauls, M. Augath, T. Trinath, and A. Oeltermann, “Neurophysiological investigation of the basis of the fMRI signal,” *Nature*, vol. 412, no. 6843, pp. 150–157, 2001.
- [43] M. E. Raichle and D. A. Gusnard, “Appraising the brain’s energy budget.,” *Proc. Natl. Acad. Sci. U. S. A.*, vol. 99, no. 16, pp. 10237–9, Aug. 2002.
- [44] L. Gagnon, A. Smith, D. Boas, A. Devor, T. Secomb, and S. Sakadzic, “Modeling of Cerebral Oxygen Transport Based on In vivo Microscopic Imaging of Microvascular Network Structure, Blood Flow, and Oxygenation,” *Front. Comput. Neurosci.*, vol. 1, Sep. 2016.
- [45] J. Proudman, “IV. Notes on the motion of viscous liquids in channels,” *London, Edinburgh, Dublin Philos. Mag. J. Sci.*, vol. 28, no. 163, pp. 30–36, Jul. 1914.
- [46] N. K. Logothetis, “The Underpinnings of the BOLD Functional Magnetic Resonance Imaging Signal,” *J. Neurosci.*, vol. 23, no. 10, pp. 3963 LP – 3971, May 2003.
- [47] D. J. Heeger and D. Ress, “What does fMRI tell us about neuronal activity?,” *Nat. Rev. Neurosci.*, vol. 3, no. 2, pp. 142–151, 2002.
- [48] X. Hu and E. Yacoub, “The story of the initial dip in fMRI,” *Neuroimage*, vol. 62, no. 2, pp. 1103–1108, Aug. 2012.
- [49] F. Schlegel, A. Schroeter, and M. Rudin, “The hemodynamic response to somatosensory stimulation in mice depends on the anesthetic used: Implications on analysis of mouse fMRI data,” *Neuroimage*, vol. 116, pp. 40–49, Aug. 2015.
- [50] M. T. Colonnese, M. A. Phillips, M. Constantine-Paton, K. Kaila, and A. Jasanoff, “Development of

- hemodynamic responses and functional connectivity in rat somatosensory cortex," *Nat. Neurosci.*, vol. 11, no. 1, pp. 72–79, 2008.
- [51] N. K. Logothetis, "What we can do and what we cannot do with fMRI," *Nature*, vol. 453, no. 7197, pp. 869–878, 2008.
- [52] J. M. Adamczak, T. D. Farr, J. U. Seehafer, D. Kalthoff, and M. Hoehn, "High field BOLD response to forepaw stimulation in the mouse," *Neuroimage*, vol. 51, no. 2, pp. 704–712, Jun. 2010.
- [53] P. Mansfield, "Multiplanar Image Formation using NMR Spin Echos," *J. Phys. C Solid State Phys.*, vol. 10, p. L55, 1977.
- [54] H. Lu, Y. Mazaheri, R. Zhang, A. Jesmanowicz, and J. S. Hyde, "Multishot partial-k-space EPI for high-resolution fMRI demonstrated in a rat whisker barrel stimulation model at 3t," *Magn. Reson. Med.*, vol. 50, no. 6, pp. 1215–1222, Dec. 2003.
- [55] N. Ben-Eliezer, U. Goerke, K. Ugurbil, and L. Frydman, "Functional MRI using super-resolved spatiotemporal encoding," *Magn. Reson. Imaging*, vol. 30, no. 10, pp. 1401–1408, 2012.
- [56] Y. Ye, Y. Zhuo, R. Xue, and X. J. Zhou, "BOLD fMRI using a modified HASTE sequence," *Neuroimage*, vol. 49, no. 1, pp. 457–466, Jan. 2010.
- [57] T. J. Vincent *et al.*, "Longitudinal Brain Size Measurements in App/Ps1 Transgenic Mice," *Magn. Reson. Insights*, vol. 4, p. MRI.S5885, Jan. 2010.
- [58] C. Baltes, N. Radzwill, S. Bosshard, D. Marek, and M. Rudin, "Micro MRI of the mouse brain using a novel 400 MHz cryogenic quadrature RF probe," *NMR Biomed.*, vol. 22, no. 8, pp. 834–842, Oct. 2009.
- [59] B. B. Biswal, F. Z. Yetkin, V. M. Haughton, and J. S. Hyde, "Functional connectivity in the motor cortex of resting human brain using echo-planar MRI," *Magn. Reson. Med.*, 1995.
- [60] C. P. Pawela *et al.*, "Resting-state functional connectivity of the rat brain," *Magn. Reson. Med.*, vol. 59, no. 5, pp. 1021–1029, 2008.
- [61] E. Jonckers, J. van Audekerke, G. de Visscher, A. van der Linden, and M. Verhoye, "Functional connectivity fMRI of the rodent brain: Comparison of functional connectivity networks in rat and mouse," *PLoS One*, vol. 6, no. 4, 2011.
- [62] J. Bijsterbosch, S. M. Smith, and C. F. Beckmann, *Introduction to Resting State fMRI Functional Connectivity*. 2017.
- [63] F. Barkhof, S. Haller, and S. A. R. B. Rombouts, "Resting-State Functional MR Imaging: A New Window to the Brain," *Radiology*, vol. 272, no. 1, pp. 29–49, Jul. 2014.
- [64] J. S. Damoiseaux *et al.*, "Consistent resting-state networks across healthy subjects," *Proc. Natl. Acad. Sci.*, vol. 103, no. 37, pp. 13848 LP – 13853, Sep. 2006.
- [65] S. M. Smith *et al.*, "Correspondence of the brain's functional architecture during activation and rest," *Proc. Natl. Acad. Sci.*, vol. 106, no. 31, pp. 13040–13045, Aug. 2009.
- [66] S. Gaudio *et al.*, "Altered resting state functional connectivity of anterior cingulate cortex in drug naïve adolescents at the earliest stages of anorexia nervosa," *Sci. Reports (Nature Res.)*, vol. 5, p. 10818, Jun. 2015.
- [67] M. J. Brookes *et al.*, "Investigating the electrophysiological basis of resting state networks using magnetoencephalography," *Proc. Natl. Acad. Sci.*, vol. 108, no. 40, pp. 16783 LP – 16788, Oct. 2011.
- [68] W.-J. Pan, G. Thompson, M. Magnuson, W. Majeed, D. Jaeger, and S. Keilholz, "Broadband local field potentials correlate with spontaneous fluctuations in functional magnetic resonance imaging signals in the rat somatosensory cortex under isoflurane anesthesia," *Brain Connect.*, vol. 1, no. 2, pp. 119–131, 2011.
- [69] M. Bruyns-Haylett, S. Harris, L. Boorman, Y. Zheng, J. Berwick, and M. Jones, "The resting-state neurovascular coupling relationship: rapid changes in spontaneous neural activity in the somatosensory cortex are associated with haemodynamic fluctuations that resemble stimulus-evoked haemodynamics," *Eur. J. Neurosci.*, vol. 38, no. 6, pp. 2902–2916, Sep. 2013.
- [70] Y. Ma *et al.*, "Resting-state hemodynamics are spatiotemporally coupled to synchronized and symmetric neural activity in excitatory neurons," *Proc. Natl. Acad. Sci.*, vol. 113, no. 52, p. E8463 LP-E8471, Dec. 2016.
- [71] D. Bajic, M. M. Craig, C. R. L. Mongerson, D. Borsook, and L. Becerra, "Identifying rodent resting-state brain networks with independent component analysis," *Front. Neurosci.*, vol. 11, no. DEC, 2017.
- [72] M. Magnuson, W. Majeed, and S. D. Keilholz, "Functional connectivity in blood oxygenation level-

- dependent and cerebral blood volume-weighted resting state functional magnetic resonance imaging in the rat brain,” *J. Magn. Reson. Imaging*, vol. 32, no. 3, pp. 584–592, Sep. 2010.
- [73] K. A. Williams *et al.*, “Comparison of alpha-chloralose, medetomidine and isoflurane anesthesia for functional connectivity mapping in the rat,” *Magn. Reson. Imaging*, vol. 28, no. 7, pp. 995–1003, Sep. 2010.
- [74] A. Gozzi and A. J. Schwarz, “Large-scale functional connectivity networks in the rodent brain,” *Neuroimage*, vol. 127, pp. 496–509, 2016.
- [75] T. T. Liu, A. Nalci, and M. Falahpour, “The global signal in fMRI: Nuisance or Information?,” *Neuroimage*, vol. 150, pp. 213–229, 2017.
- [76] M. D. Fox, A. Z. Snyder, J. L. Vincent, M. Corbetta, D. C. Van Essen, and M. E. Raichle, “The human brain is intrinsically organized into dynamic, anticorrelated functional networks,” *Proc. Natl. Acad. Sci. U. S. A.*, vol. 102, no. 27, pp. 9673 LP – 9678, Jul. 2005.
- [77] K. Murphy, R. M. Birn, D. A. Handwerker, T. B. Jones, and P. A. Bandettini, “The impact of global signal regression on resting state correlations: are anti-correlated networks introduced?,” *Neuroimage*, vol. 44, no. 3, pp. 893–905, Feb. 2009.
- [78] A. Shmuel and D. A. Leopold, “Neuronal correlates of spontaneous fluctuations in fMRI signals in monkey visual cortex: Implications for functional connectivity at rest,” *Hum. Brain Mapp.*, vol. 29, no. 7, pp. 751–761, Jul. 2008.
- [79] K. H. Chuang *et al.*, “Evaluation of nuisance removal for functional MRI of rodent brain,” *Neuroimage*, vol. 188, no. October 2018, pp. 694–709, 2019.
- [80] D. V Smith *et al.*, “Characterizing individual differences in functional connectivity using dual-regression and seed-based approaches,” *Neuroimage*, vol. 95, pp. 1–12, Jul. 2014.
- [81] D. M. Cole, S. M. Smith, and C. F. Beckmann, “Advances and pitfalls in the analysis and interpretation of resting-state FMRI data,” *Front. Syst. Neurosci.*, vol. 4, p. 8, Apr. 2010.
- [82] K. R. A. Van Dijk, T. Hedden, A. Venkataraman, K. C. Evans, S. W. Lazar, and R. L. Buckner, “Intrinsic functional connectivity as a tool for human connectomics: theory, properties, and optimization,” *J. Neurophysiol.*, vol. 103, no. 1, pp. 297–321, Jan. 2010.
- [83] J. Lin, X. Cui, X. Dai, and L. Mo, “Regional Homogeneity Predicts Creative Insight: A Resting-State fMRI Study,” *Front. Hum. Neurosci.*, vol. 12, p. 210, May 2018.
- [84] T. Tsurugizawa, B. Djemai, and A. Zalesky, “The impact of fasting on resting state brain networks in mice,” *Sci. Rep.*, vol. 9, no. 1, pp. 1–12, 2019.
- [85] M. Siyah Mansoor, M. A. Oghabian, A. H. Jafari, and A. Shahbabaie, “Analysis of Resting-State fMRI Topological Graph Theory Properties in Methamphetamine Drug Users Applying Box-Counting Fractal Dimension,” *Basic Clin. Neurosci.*, vol. 8, no. 5, pp. 371–385, 2017.
- [86] M. G. Preti, T. A. Bolton, and D. Van De Ville, “The dynamic functional connectome: State-of-the-art and perspectives,” *Neuroimage*, vol. 160, no. December 2016, pp. 41–54, 2017.
- [87] Z. Liang, J. King, and N. Zhang, “Uncovering intrinsic connective architecture of functional networks in awake rat brain,” *J. Neurosci.*, vol. 31, no. 10, pp. 3776–3783, Mar. 2011.
- [88] E. Jonckers, R. Delgado y Palacios, D. Shah, C. Guglielmetti, M. Verhoye, and A. Van der Linden, “Different anesthesia regimes modulate the functional connectivity outcome in mice,” *Magn. Reson. Med.*, vol. 72, no. 4, pp. 1103–1112, Oct. 2014.
- [89] J. Grandjean, A. Schroeter, I. Batata, and M. Rudin, “Optimization of anesthesia protocol for resting-state fMRI in mice based on differential effects of anesthetics on functional connectivity patterns,” *Neuroimage*, vol. 102, no. P2, pp. 838–847, 2014.
- [90] J. L. Tremoleda, S. Macholl, and J. K. Sosabowski, “Anesthesia and Monitoring of Animals During MRI Studies BT - Preclinical MRI: Methods and Protocols,” M. L. García Martín and P. López Larrubia, Eds. New York, NY: Springer New York, 2018, pp. 423–439.
- [91] J. Paasonen, P. Stenroos, R. A. Salo, V. Kiviniemi, and O. Gröhn, “Functional connectivity under six anesthesia protocols and the awake condition in rat brain,” *Neuroimage*, vol. 172, no. October 2017, pp. 9–20, 2018.
- [92] A. Sumiyoshi, R. J. Keeley, and H. Lu, “Physiological Considerations of Functional Magnetic Resonance Imaging in Animal Models,” *Biol. Psychiatry Cogn. Neuroimaging*, vol. 4, no. 6, pp. 522–532, Jun. 2019.
- [93] F. A. Nasrallah, H. C. Tay, and K. H. Chuang, “Detection of functional connectivity in the resting mouse brain,” *Neuroimage*, vol. 86, pp. 417–424, 2014.
- [94] X. Liu *et al.*, “Multiphasic modification of intrinsic functional connectivity of the rat brain during

- increasing levels of propofol," *Neuroimage*, vol. 83, pp. 581–592, Dec. 2013.
- [95] P. Flecknell, "Chapter 2 - Managing and Monitoring Anaesthesia," in *Laboratory Animal Anaesthesia*, P. B. T.-L. A. A. (Fourth E. Flecknell, Ed. Boston: Academic Press, 2016, pp. 77–108.
- [96] Q. Bukhari, A. Schroeter, D. M. Cole, and M. Rudin, "Resting state fMRI in mice reveals anesthesia specific signatures of brain functional networks and their interactions," *Front. Neural Circuits*, vol. 11, no. February, pp. 1–11, 2017.
- [97] P. Flecknell, "Chapter 5 - Anaesthesia of Common Laboratory Species: Special Considerations," in *Laboratory Animal Anaesthesia*, P. B. T.-L. A. A. (Fourth E. Flecknell, Ed. Boston: Academic Press, 2016, pp. 193–256.
- [98] S. I. Ganzberg and D. A. Haas, "15 - General Anesthesia," in *Pharmacology and Therapeutics for Dentistry*, F. J. Dowd, B. S. Johnson, and A. J. B. T.-P. and T. for D. (Seventh E. Mariotti, Eds. Mosby, 2017, pp. 221–240.
- [99] J. P. Nolan, "Chapter 19 - Anaesthesia and neuromuscular block," in *Clinical Pharmacology*, P. N. Bennett, M. J. Brown, and P. B. T.-C. P. (Eleventh E. Sharma, Eds. Oxford: Churchill Livingstone, 2012, pp. 295–310.
- [100] M. D. Sinclair, "A review of the physiological effects of alpha2-agonists related to the clinical use of medetomidine in small animal practice," *Can. Vet. J. = La Rev. Vet. Can.*, vol. 44, no. 11, pp. 885–897, Nov. 2003.
- [101] M. Fukuda, A. L. Vazquez, X. Zong, and S.-G. Kim, "Effects of the  $\alpha_2$ -adrenergic receptor agonist dexmedetomidine on neural, vascular and BOLD fMRI responses in the somatosensory cortex," *Eur. J. Neurosci.*, vol. 37, no. 1, pp. 80–95, Jan. 2013.
- [102] T. D. Ambrisko and Y. Hikasa, "Neurohormonal and metabolic effects of medetomidine compared with xylazine in beagle dogs," *Can. J. Vet. Res.*, vol. 66, no. 1, pp. 42–49, Jan. 2002.
- [103] C. M. Jorm and J. A. Stamford, "Actions of the hypnotic anaesthetic, dexmedetomidine, on noradrenaline release and cell firing in rat locus coeruleus slices," *Br. J. Anaesth.*, vol. 71, no. 3, pp. 447–449, 1993.
- [104] M. E. Magnuson, G. J. Thompson, W.-J. Pan, and S. D. Keilholz, "Time-dependent effects of isoflurane and dexmedetomidine on functional connectivity, spectral characteristics, and spatial distribution of spontaneous BOLD fluctuations," *NMR Biomed.*, vol. 27, no. 3, pp. 291–303, Mar. 2014.
- [105] C. Gelegen *et al.*, "Staying awake--a genetic region that hinders  $\alpha_2$  adrenergic receptor agonist-induced sleep," *Eur. J. Neurosci.*, vol. 40, no. 1, pp. 2311–2319, Jul. 2014.
- [106] P. Flecknell, "Chapter 1 - Basic Principles of Anaesthesia," in *Laboratory Animal Anaesthesia*, P. B. T.-L. A. A. (Fourth E. Flecknell, Ed. Boston: Academic Press, 2016, pp. 1–75.
- [107] K. J. Field and C. M. Lang, "Hazards of urethane (ethyl carbamate): a review of the literature," *Lab. Anim.*, vol. 22, no. 3, pp. 255–262, Jul. 1988.
- [108] P. Flecknell, "Chapter 3 - Special Techniques," in *Laboratory Animal Anaesthesia*, P. B. T.-L. A. A. (Fourth E. Flecknell, Ed. Boston: Academic Press, 2016, pp. 109–140.
- [109] T. Wu, J. Grandjean, S. C. Bosshard, M. Rudin, D. Reutens, and T. Jiang, "Altered regional connectivity reflecting effects of different anaesthesia protocols in the mouse brain," *Neuroimage*, vol. 149, pp. 190–199, 2017.
- [110] V. Zerbi, J. Grandjean, M. Rudin, and N. Wenderoth, "Mapping the mouse brain with rs-fMRI: An optimized pipeline for functional network identification," *Neuroimage*, vol. 123, pp. 11–21, 2015.
- [111] F. Sforazzini *et al.*, "Altered functional connectivity networks in acallosal and socially impaired BTBR mice," *Brain Struct. Funct.*, vol. 221, no. 2, pp. 941–954, 2016.
- [112] J. Grandjean *et al.*, "Common functional networks in the mouse brain revealed by multi-centre resting-state fMRI analysis (Supplementary material)," *bioRxiv*, p. 541060, Jan. 2019.
- [113] Y.-Q. Zhou, F. S. Foster, B. J. Nieman, L. Davidson, X. J. Chen, and R. M. Henkelman, "Comprehensive transthoracic cardiac imaging in mice using ultrasound biomicroscopy with anatomical confirmation by magnetic resonance imaging," *Physiol. Genomics*, vol. 18, no. 2, pp. 232–244, Jul. 2004.
- [114] G. Vanhoutte, M. Verhoye, and A. Van der Linden, "Changing body temperature affects the T signal in the rat brain and reveals hypothalamic activity," *Magn. Reson. Med.*, vol. 55, no. 5, pp. 1006–1012, May 2006.
- [115] J.-M. Heydel, E. Holsztyńska, A. Legendre, N. Thiebaud, Y. Artur, and A.-M. Le Bon, "UDP-glucuronosyltransferases (UGTs) in neuro-olfactory tissues: Expression, regulation, and function,"

- Drug Metab. Rev.*, vol. 42, pp. 74–97, Feb. 2010.
- [116] K. J. Friston, *Statistical parametric mapping: the analysis of functional brain images*. Amsterdam; Boston: Elsevier / Academic Press, 2007.
- [117] C. Chavarrías, V. García-Vázquez, Y. Alemán-Gómez, P. Montesinos, J. Pascau, and M. Desco, “fMRat: an extension of SPM for a fully automatic analysis of rodent brain functional magnetic resonance series,” *Med. Biol. Eng. Comput.*, vol. 54, no. 5, pp. 743–752, 2016.
- [118] B. B. Avants, N. J. Tustison, G. Song, P. A. Cook, A. Klein, and J. C. Gee, “A reproducible evaluation of ANTs similarity metric performance in brain image registration,” *Neuroimage*, vol. 54, no. 3, pp. 2033–2044, Feb. 2011.
- [119] K. Gorgolewski *et al.*, “Nipype: a flexible, lightweight and extensible neuroimaging data processing framework in python,” *Front. Neuroinform.*, vol. 5, p. 13, Aug. 2011.
- [120] E. Jones, T. Oliphant, and P. Peterson, “SciPy: Open Source Scientific Tools for Python,” Jan. 2001.
- [121] A. Roche, “A Four-Dimensional Registration Algorithm With Application to Joint Correction of Motion and Slice Timing in fMRI,” *IEEE Trans. Med. Imaging*, vol. 30, no. 8, pp. 1546–1554, 2011.
- [122] A. Klein *et al.*, “Evaluation of 14 nonlinear deformation algorithms applied to human brain MRI registration,” *Neuroimage*, vol. 46, no. 3, pp. 786–802, 2009.
- [123] A. L. Janke and J. F. P. Ullmann, “Robust methods to create ex vivo minimum deformation atlases for brain mapping,” *Methods*, vol. 73, pp. 18–26, 2015.
- [124] D. Janke, A.L., Ullmann, J.F.P., Kurniawan, N., Paxinos, G., Keller, M., Yang, Z., Richards, K., Egan, G., Petrou, S., Galloway, G., Reutens, “15µm average mouse models in Waxholm space from 16.4T 30µm images.,” in *20th Annual ISMRM Scientific Meeting and Exhibition. Melbourne, Australia.*, 2012.
- [125] A. M. Winkler, G. R. Ridgway, M. A. Webster, S. M. Smith, and T. E. Nichols, “Permutation inference for the general linear model,” *Neuroimage*, vol. 92, pp. 381–397, May 2014.
- [126] T. A. Seabrook, T. J. Burbridge, M. C. Crair, and A. D. Huberman, “Architecture, Function, and Assembly of the Mouse Visual System,” *Annu. Rev. Neurosci.*, vol. 40, no. 1, pp. 499–538, Jul. 2017.
- [127] A. Niranjan, I. N. Christie, S. G. Solomon, J. A. Wells, and M. F. Lythgoe, “fMRI mapping of the visual system in the mouse brain with interleaved snapshot GE-EPI,” *Neuroimage*, vol. 139, pp. 337–345, 2016.
- [128] M. H. Buonocore and L. Gao, “Ghost artifact reduction for echo planar imaging using image phase correction,” *Magn. Reson. Med.*, vol. 38, no. 1, pp. 89–100, 1997.
- [129] L. Griffanti *et al.*, “Hand classification of fMRI ICA noise components,” *Neuroimage*, vol. 154, pp. 188–205, 2017.
- [130] M. F. Glasser *et al.*, “Classification of temporal ICA components for separating global noise from fMRI data: Reply to Power,” *Neuroimage*, vol. 197, pp. 435–438, 2019.
- [131] Y.-T. Kuo, A. H. Herlihy, P.-W. So, K. K. Bhakoo, and J. D. Bell, “In vivo measurements of T1 relaxation times in mouse brain associated with different modes of systemic administration of manganese chloride,” *J. Magn. Reson. Imaging*, vol. 21, no. 4, pp. 334–339, Apr. 2005.
- [132] R. M. Hutchison, S. M. Mirsattari, C. K. Jones, J. S. Gati, and L. S. Leung, “Functional Networks in the Anesthetized Rat Brain Revealed by Independent Component Analysis of Resting-State fMRI,” *J. Neurophysiol.*, vol. 103, no. 6, pp. 3398–3406, Apr. 2010.
- [133] B. R. White, A. Q. Bauer, A. Z. Snyder, B. L. Schlaggar, J. M. Lee, and J. P. Culver, “Imaging of functional connectivity in the mouse brain,” *PLoS One*, vol. 6, no. 1, 2011.
- [134] F. Zhao, T. Zhao, L. Zhou, Q. Wu, and X. Hu, “BOLD study of stimulation-induced neural activity and resting-state connectivity in medetomidine-sedated rat,” *Neuroimage*, vol. 39, no. 1, pp. 248–260, Jan. 2008.
- [135] T. Watanabe, Z. Tan, X. Wang, A. Martinez-Hernandez, and J. Frahm, “Magnetic resonance imaging of noradrenergic neurons,” *Brain Struct. Funct.*, vol. 0, no. 0, p. 0, 2019.
- [136] J. Grandjean *et al.*, “Common functional networks in the mouse brain revealed by multi-centre resting-state fMRI analysis (Supplementary information),” *bioRxiv*, p. 541060, Jan. 2019.

# Annex A

**Table A.1:** Summary of 10 rsfMRI studies performed in mice, highlighting the objective, parameters used in the acquisition and details on animal preparation. It should be noted that only the aspects relating to the mapping of functional networks are discriminated, as several studies had a wider range of analysis not considered relevant for the scope this thesis. FOV = Field of view, MS = Matrix size, resol = pixel resolution.

|    | Study                        | Goal  | MRI parameters  | Animal preparation   |
|----|------------------------------|---|---|--|
| 1  | Jonckers et al, 2011 [61]    | Implement rsfMRI in mice and compare obtained functional networks with rats.            | 9.4T, GE-EPI. TR/TE = 2000/15 ms, 12 slices (0.4 mm thick) e 0.1 mm gap, FOV 20x20 mm <sup>2</sup> , MS = 128x64, resol = 0.16x0.31 mm <sup>2</sup> , 150 repetitions | 9 male mice, 0.6mg/kg/h medetomidine, free breathing.  |
| 2  | Guilfoyle et al, 2013 [20]   | Perform rsfMRI in mice using only isoflurane as anesthetic.                             | 7T, 3-shot EPI. TR/TE=2000/20ms, 14 slices (1mm thick), 0.1mm gap, FOV=30x30 mm <sup>2</sup> , MS=64x64, resol=0.469x0.469 mm <sup>2</sup> , 360 repetitions          | 12 male mice, 1.5% iso, free breathing.  |
| 3  | Grandjean et al, 2014 [89]   | Compare 4 anesthesia protocols: medetomidine, isoflurane, propofol, and urethane        | 9.4T cryoprobe, GE-EPI, TR/TE=1000/10ms, 12 slices (0.5mm thick), FOV=23.7x14 mm <sup>2</sup> , MS=90x60, resol=0.263x0.233 mm <sup>2</sup> , 360 repetitions         | 63 female mice, 1% and 1.5% iso, 0.1 and 0.2mg/kg/h medetomidine, 120-150mg/kg/h propofol, 1.2 and 1.5g/kg urethane, endotracheal intubation |
| 4  | Nasrallah et al, 2014 [93]   | Compare 3 different dosages of medetomidine.  | 9.4T, GE-EPI, TR/TE=2000/15ms, 15 slices (0.5 mm thick), FOV=20x20 mm <sup>2</sup> , MS=64x64, resol=0.3125x0.3125 mm <sup>2</sup> , 300 repetitions                  | 0.1/0.6/1 mg/kg/h i.p. medetomidine, 25 mice, free breathing   |
| 5  | Zerbi et al, 2015 [110]      | Test the use of a noise removal algorithm (FIX).  | 9.4T cryoprobe, GE-EPI, TR/TE=1000/10ms, FOV=23.7x14 mm <sup>2</sup> , MS=90x60, resol=0.263x0.233 mm <sup>2</sup> , 360 repetitions                                  | 15 mice, medetomidine (0.01mg/kg/h I.V.) + 0.5% isoflurane, endotracheal intubation  |
| 6  | Sforazzini et al, 2016 [111] | Identify FC differences in healthy vs BTBR (autism model) mice.                         | 7T, GE-EPI TR/TE=1000/15ms, 16 slices (0.5mm thick), FOV=23x20 mm <sup>2</sup> , MS=100x87, resol=0.23x0.23 mm <sup>2</sup> , 360 repetitions                         | 10 C57BL/6J (normal) mice + 10 BTBR mice, intubated, halothane 0.7%  |
| 7  | Bukhari et al, 2017 [96]     | Uses data from (3) to apply ICA, dual regression and network modelling (same objective) |   |  |
| 8  | Wu et al, 2017 [109]         | Uses data from (3) to apply ReHo analysis (same objective)                              |   |  |
| 9  | Tsurugizawa et al, 2019 [84] | Study fasting impact on FC networks.  | 11.7T cryoprobe, GE-EPI, TR/TE=2000/12ms, 15 slices (0.5 mm thick), FOV=15x9.2 mm <sup>2</sup> , MS=150x92, resol=0.1x0.1 mm <sup>2</sup> , 180 repetitions           | 11 non-fasted, 8 fasted mice, isoflurane (0.8-1%)  |
| 10 | Grandjean et al, 2019 [112]  | Use a general optimized pipeline to identify common networks across centers.            | Numerous datasets were used: Details on supplementary information [136] (variation of field strength, coil type, TR/TE, slices, FOV/MS/resol, repetitions)            |  |

**Table A.2:** Summary of 10 rsfMRI studies performed in mice, highlighting the preprocessing and analysis pipelines, results and main conclusions. It should be noted that only the aspects relating to the mapping of functional networks are discriminated, as several studies had a wider range of analysis not considered relevant for the scope of this thesis.

|    | Preprocessing + Analysis  | Results/Conclusions   |
|----|---|---|
| 1  | Motion correction, normalization, spatial smoothing 0.3x0.4mm <sup>2</sup> FWHM, bandpass filter 0.01Hz-0.1 Hz. ICA with GIFT with 15, 30 and 40 components   | Different FC patterns for rats and mice. Depend strongly on number of components of ICA. Appearance of unilateral cortical components for the mouse data compared to bilateral rat cortical networks. More components needed for the ICA to separate cortical regions in mice.  |
| 2  | Motion correction, 2mm FWHM Gaussian kernel spatial smoothing, bandpass (0.005-0.1Hz), detrend, normalization. SBA with seeds based on previous works   | Evidence of a DMN for lateral cortical and medial cortical seeds (but with low spatial specificity). Functional connectivity for these seeds included cortical regions. Right lateral and medial seed also showed FC with hippocampus (often included in the DMN). Not so clear for insular and prefrontal seeds - more circumscribed regional FC.                  |
| 3  | Motion correction, slice-timing correction, normalization. GSR and motion parameters regression. Bandpass filter (0.01 - 0.3 Hz). SBA analysis + interhemispheric correlation analysis.   | Isoflurane, propofol and urethane resulted in bilateral correlation with respect to cortical seeds, but no significant inter-hemispheric striatal connectivity. Medetomidine showed bilateral striatal but compromised interhemispheric cortical connectivity. Medetomidine + isoflurane - best inter-hemispheric connectivity and striatal bilateral connectivity. |
| 4  | 0.01-0.1Hz bandpass, FWHM=0.3125, ventricular signal regression. SBA analysis (threshold=0.2) and interhemispheric correlation analysis.  | Found bilateral FC for 0.1 and 0.6 mg/kg/h (1mg/kg/h shows poor FC patterns)  |
| 5  | Skull stripping, MELODIC ICA, high-pass filtering (>0.01 Hz), motion correction and spatial smoothing (0.3x0.3 mm <sup>2</sup> kernel). FIX training and testing. SBA with 3 seeds to compare pipelines + ICA to identify 23 networks + Network analysis.   | FIX showed a very good performance, and using that algorithm, 23 resting state circuits in mice were identified, including two networks that displayed default mode network-like topography   |
| 6  | Normalization, motion correction, motion parameters and ventricular signal regression, bandpass (0.01-0.08Hz), spatial smoothing FWHM gaussian kernel 0.6 mm. SBA and interhemispheric correlation analysis.  | Impaired intra-hemispheric connectivity in fronto-cortical but not posterior sensory cortical areas. Altered subcortical and intra-hemispheric connectivity networks, with evidence of marked frontothalamic and striatal dysconnectivity, along with aberrant spatial extension and strength of ipsilateral and local connectivity                                 |
| 7  | Uses data from (3) to apply ICA, dual regression and network modelling (same objective and similar conclusions)   |   |
| 8  | Uses data from (3) to apply ReHo analysis (same objective and similar conclusions)  |   |
| 9  | Slice timing, realignment, normalization, motion parameters regression, ventricular and white matter signal regression. Bandpass (0.01–0.1 Hz), spatial smoothing Gaussian (0.2 × 0.2 × 0.5 mm <sup>3</sup> ). Parcellation of cortex and subcortex into 52 ROIs (80–2000 voxels) to build a connectivity matrix. ALFF analysis | FC was globally increased in fasted vs non-fasted group (particularly between the hippocampus (bilateral), retrosplenial cortex (left), visual cortex (left) and auditory cortex (left)).   |
| 10 | Brain extraction, normalization, spatial smoothing, temporal filtering, motion correction and motion parameter regression. GSR, ventricular regression, vasculature regression, white matter regression. SBA to compare pipelines and ICA to identify networks.   | Preprocessing qualitatively affected the maps, SBA delivers reproducible large-scale networks in most datasets, sedation and other protocol differences alter FC strength.  |